Determination of Sheath Heat Transmission Coefficient in NSTX Discharges with Applied Lithium Coatings

Joshua Benjamin Kallman

A Dissertation Presented To The Faculty
Of Princeton University
In Candidacy For The Degree
Of Doctor Of Philosophy

Recommended For Acceptance
By The Program In Plasma Physics
Of The Department Of
Astrophysical Sciences

Advisor: Robert Kaita

September 2011

In memory of my grandmother,
Elka Zibman,
who valued knowledge in all its forms.

Abstract

Recycled particle flux can be a significant contributor to tokamak edge plasma density, and lead to reductions in edge temperature. Previous measurements have shown that solid evaporated lithium coatings can lead to lowered edge recycling, corresponding decreases in edge plasma density, and a radial broadening of the electron temperature profile. During the 2010 run campaign, The National Spherical Torus Experiment operated with both solid and liquid lithium coatings on its plasma-facing components. A section of graphite outer divertor tiles was replaced with a substrate designed to hold liquid lithium coatings. While the lithium coatings on the graphite remain solid, the plates can be heated to render the lithium into a liquid state.

In preparation for this campaign, a 99-tip dense Langmuir probe array was installed in the outboard divertor to measure scrape-off layer density and temperature. The probe array was located so as to radially span these two different divertor surfaces and measure their respective effects on the temperature and density. A dual-band fast IR camera was also installed to provide surface temperature and heat flux measurements. The use of two-color IR thermography allows for an assessment of effects due to the uncertain, phase- and purity-dependent emissivity of the lithium coatings.

The present study compares the derived heat fluxes from these diagnostics to determine an effective classical sheath heat transmission coefficient γ, a measure of the heat flow reaching the device surfaces as a function of plasma parameters, namely the edge temperature and density - quantities which should be modified by lithium coatings. The sheath heat transmission is of great interest to future devices, which can expect to see large steady-state and transient heat fluxes to material surfaces. The value of γ was measured to be 2.49 +/- 0.04, a factor of ~3 smaller than the expected classical result of ~7. The implications of this measurement and the changes to edge plasma profiles that are possible causes of the lower observed value are discussed.

Supported by US-DOE Contract DE-AC02-09CH11466.

Contents

List of Figures

List of Tables

Acknowledgements

Though I have signed sworn statements that this work represents the fruit of my own labors, it would surely not have been possible without the support and assistance of those around me. Though it may take an entire village to raise a child, the number of people that have aided me during the production of this document in some capacity, academic or otherwise, is not so far short of that number.

First and foremost, I would like to thank my parents, Rena and David Kallman. They supported me when I first embarked on my foray into the world of physics, and gave me encouragement when others doubted my resolve. It was with their counsel that I was able to navigate the transition from classics to physics and collect degrees in both. My other relatives, including my younger brothers Danny and Seth, my grandparents Sheila and Harold Kallman, my late grandmother Elka Zibman, and other aunts, uncles, and cousins also provided the encouragement that only family can.

I would also like to thank my advisor, Robert Kaita, who was my unfailing advocate throughout my tenure as his student. He is a man of many hats and responsibilities, but always found the time to acquire a power supply for a test of mine or offer me insightful suggestions on the latest results. He was also a liaison with the senior members of the NSTX research staff, making sure I had the technician support I needed or helping me craft a proposal for machine run time. In addition, he was a tireless editor and refiner of my presentations, abstracts, and papers over the years, even adding a few Latin phrases to my scientific writing vocabulary.

I'd also like to thank the advisors that worked with me on my first and second year projects (and beyond with the lithium work on NSTX) , Jon Menard and Leonid Zakharov, both of whom encouraged me in their own ways and helped me understand the finer points of magnetohydrodynamics and its associated experimental and theoretical methods. Jill Foley also deserves recognition for helping me along early in my career as an intern, and encouraging me to pursue plasma physics at the graduate level.

I also had the privilege to work with Henry Kugel, one of the pioneers in lithium research in fusion devices, on much of the lithium technology in this thesis. There are few (if any) in the field with his expertise in such matters, and without his vision for NSTX lithium work, very little of what is contained in these pages would be possible. His experience proved invaluable in the design of many of the experiments conducted over the course of my research.

Additionally, I would be remiss were I not to thank our department secretary and surrogate mother, Barbara Sarfaty. She is the force that holds the graduate program together, and was always there to offer assistance with the labyrinthine Princeton paperwork, second monitors or laptops for extra productivity, or just someone to have a pleasant chat with after lunch.

The construction and operation of the Langmuir probe array would not have been possible without the help of Mike Jaworski, who designed the electronics system and software that ensured its operation. He always provided valuable advice on the operation or interpretation of probe data, especially where the effects of lithium were concerned. In addition, he and I conducted many experiments together on the physical and chemical properties of lithium, and I learned much of proper experimental procedure under his guidance. Were such a title in existence, I would surely refer to him as my 'junior advisor'.

I am also grateful for the help of many technicians and engineers who assisted me with various lithium experiments or with the design and assembly of the Langmuir probe array. Particular among these was John Timberlake, who had an uncanny knack for assembling the perfect device for the job with the imperfect and limited materials at hand. With his recent passing, the field has lost one of the greatest stores of experiential knowledge it has probably ever known. I was also greatly assisted by Larry Guttadora, who brought his many years of diagnostic design experience to bear in the creation of the Langmuir probe array. It was through many iterations with him of materials and design concepts that the final product emerged, and I was thankful for his knowledge at every step of the way.

Eugene 'Buddy' Kearns also was also a large help in many of the small-scale experimental tests, and was quick with a wrench and a whiz at the bench. The others that helped me are too numerous to mention, but I would like to give special thanks to Doug Westover and Westley Reese for help with the assembly and wiring of the probe array, and Scott Gifford and Mike Anderson for help during installation - and to all of them for never cursing me (openly) for deciding to place 99 probes in such a small space.

Lastly, I would like to thank all of my friends and fellow grad students, my brothers and sisters in arms. Whether present at Princeton or otherwise, their willingness to discuss the nagging nuances of thesis tedium was always a comfort. Whether as part of our championship Pub Quiz team or the valiant Tokabats softball team, they provided me with distraction when I needed it (or didn't), and were always a valuable sounding board for the ideas that were probably too crazy to bring before the experts mentioned above. I'd particularly like to mention Luc and Meg Peterson and Jess Baumgaertel, members of the FTC and some of the best friends I've made at Princeton or otherwise. My office-mate Craig Jacobson and I frequently filled our whiteboard with discussions of lithium technology... or sometimes the finer points of construction for dwarf fortresses. Dan Lundberg was a source of dry wit and many a hallway conversation. Laura Berzak and Tim Gray were wealths of lithium knowledge and wise beyond their years. Adam Hopkins (now married to Laura) is a chemist/physicist who always provided lively scientific or political discourse. Dave Smith and Ethan Schartman were lunch companions and proof that there was light at the end of the tunnel. I also worked closely with Tyler Abrams on the development of lithium film measurement techniques and the proper way to tag out a runner at second base. Other friends who supported me include my Stanford undergrad crew, Greg, Sarita, Pam, and Sierra, those I met at Princeton, Abe, Erik, Anton, Martin, Katy, Brendan, Kelsey, Matt, Nik, Jeff, Dennis, and all the others I may have forgotten to add here. Thanks again to you all!

Chapter 1

Introduction

1.1 Energy in the 21st century

As the world population continues to grow, so does the demand for energy. This demand is also affected by the rise in westernized lifestyle in developing nations as SUVs, HD televisions, and the other comforts of modern living become more commonplace. The International Energy Agency provides putative numbers for energy demand by fuel source in its World Energy Outlook [16], which is shown in Figure 1.1. As world energy demand

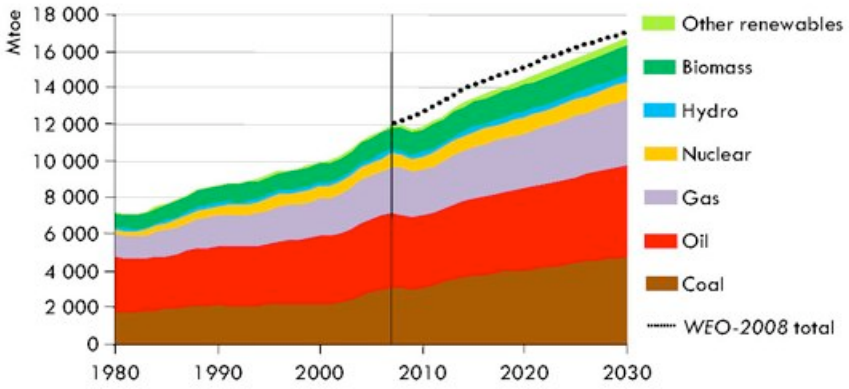

Figure 1.1: World Energy Demand by Fuel Source

increases, fossil fuels will continue to dominate the energy landscape, leading to the release of greenhouse gases. Much has already been discussed on this subject in other literature

[17], but a representative graph of greenhouse gas concentrations is shown for reference in Figure 1.2.

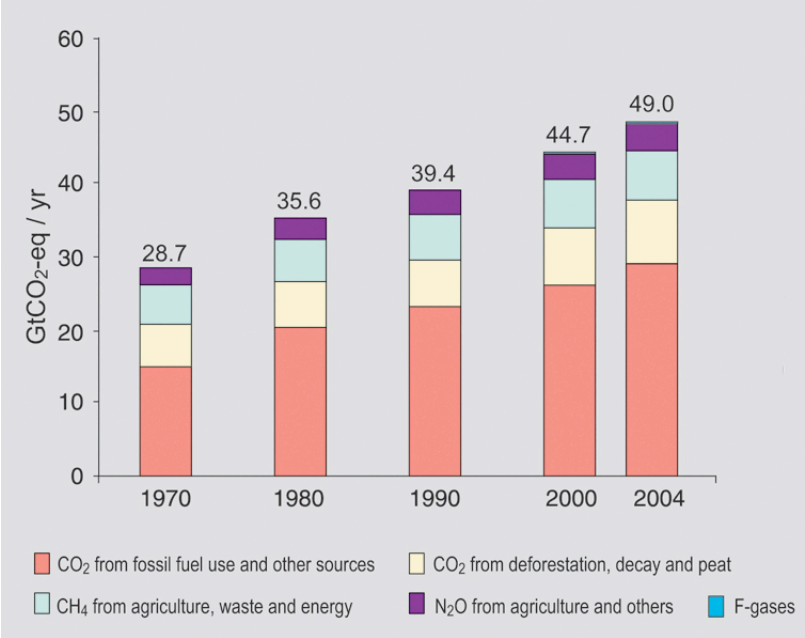

Figure 1.2: Worldwide Greenhouse Gas Emissions

Regardless of the environmental ramifications of population and energy growth, the simple fact remains that the majority of energy sources in use today are non-renewable and have limited global resources remaining. Table 1.1 shows the estimated reserves of several

Energy Source	Years Remaining
Coal	122
Oil	42
Natural Gas	60
Uranium	83*

*Does not include unreported reserves or take into account advanced fuel cycles

Table 1.1: World energy reserves [13], [14]

key fuels and the years remaining at current energy usage. Nuclear fission is included here also, and although promising from many standpoints, raises the twin specters of proliferation and waste disposal. Renewable sources will contribute to this mix, but Figure 1.1

shows that they will not make significant ingress in the next 20 years. Also, many renewable sources are only available in specific geographic locations or at certain times of day, limiting their ability to serve as cores for base-load power stations. The need exists then to develop an energy source that can provide continuous power, not constrained by location or fuel availability, and producing a minimum of greenhouse gas emissions. Nuclear fusion energy holds just such a promise.

1.2 Fusion energy

1.2.1 Nuclear Fission

The use of nuclear fission reactions to generate energy has a long-established tradition in the United States and elsewhere. The reaction of a heavy nucleus, usually ^{235}U or ^{239}Pu, with a neutron generates a daughter nucleus and one or more neutrons, which serve to perpetuate the reaction. Through Einstein's mass-energy equivalence reaction, $E = mc^2$, the differences in rest mass between the reactants and the products results in a net energy gain. The common uranium fission reaction, when fast decays are accounted for, is:

$$n + {}^{235}U \rightarrow {}^{140}Ce + {}^{94}Zr + 2n + 6e^{-} + 206MeV \tag{1.1}$$

Some of the generated neutrons are used to perpetuate the reaction, while others are absorbed by a surrounding blanket and used in a heat-exchanger/turbine combination to generate electricity much in the manner of conventional power plants.

The advantages of fission power generation are that the science is well-established and that it provides a reliable baseline method of power generation without generating the greenhouse gases associated with burning fossil fuels. Also, given an adequate supply of nuclear fuel, the conditions to initiate and sustain the reaction are relatively lax, requiring only room temperature neutrons. The disadvantages are rather significant, including safety

concerns such as meltdown, proliferation risks, and production of radioactive byproducts that can take millennia to decay.

1.2.2 Nuclear Fusion Energy

Nuclear fusion takes advantage of the same basic physics as fission, in which the rest mass of the reaction products is lower than the mass of the reactants and net energy is generated. Rather than splitting heavy nuclei, fusion takes advantage of the fact that light nuclei will produce energy when joined into a heavier nucleus. The key reactions that are exploited in current fusion research are as follows:

$$D + D \xrightarrow[50\%]{} {}^3He + n + 3.27MeV \tag{1.2}$$

$$D + D \xrightarrow[50\%]{} T + p + 4.03MeV \tag{1.3}$$

$$D + {}^3He \rightarrow \alpha + p + 18.3MeV \tag{1.4}$$

$$D + T \rightarrow \alpha + n + 17.6MeV \tag{1.5}$$

Where D is deuterium, H^2, T is tritium, H^3, and α is He^4. Deuterium is extremely abundant in nature, and is found in a 1:7000 ratio to normal hydrogen, making the oceans an almost limitless fuel source. Tritium, due to its short half-life (12 years), is not found in nature and must be produced; the traditional method for doing so is the nuclear reaction of lithium with a neutron:

$${}^6Li + n(slow) \rightarrow \alpha + T + 4.8MeV \tag{1.6}$$

$${}^7Li + n(fast) \rightarrow T + \alpha + n - 2.5MeV \tag{1.7}$$

Lithium is therefore the limiting factor in available fusion fuel, but as shown in Table 1.2 is abundant enough to provide for the Earth's energy demands into the far future, especially compared to uranium or fossil fuels. The D-T reaction, Eq. 1.5, is generally favored, due

Location	Years Remaining
Land	500
Oceans	150,000

Table 1.2: Lithium reserves [15]

to the availability of fuels and favorable cross-sections, shown below in Figure 1.3. Fusion power also avoids the meltdown hazards of fission since the amount of fuel present at any time would burn itself out after several seconds, while to achieve critical mass for a fission reactor up to a year or more of fuel must be stored. Another advantage over fission is that the reaction products are non-radioactive, although the neutrons produced can activate the surrounding materials. Nevertheless, the half-lives for activated advanced materials are on the order of years or decades, rather than millennia.

One disadvantage of fusion is that as compared to fission, much more energy is required to initiate the fusion reaction, although a silver lining of this is that the proliferation risk is greatly reduced. The cross-sections for the fusion reactions are energy dependent: the reactant nuclei must have high enough energies to overcome their mutual electrical repulsion, but the collision frequency is inversely dependent on the velocity. Thus there is a peak cross-section for the reactions at specific energies, as shown in Figure 1.3. In heating the deuterium and tritium to the required energies, the electrons are stripped from the atoms, which then become ionized and form a plasma. The energetic ions must then be confined by some method so that they react with each other rather than escape. If a sufficient particle density can be maintained at a sufficient temperature for a sufficient time, then the plasma will be self-heating and ignition is obtained. The salient measure of ignition is called the Lawson criterion [18], defined as:

$$nT\tau \geq 3 \times 10^{21} [m^{-3} Ks] \tag{1.8}$$

In the sun, the large gravitational forces present provide the necessary density, temperature,

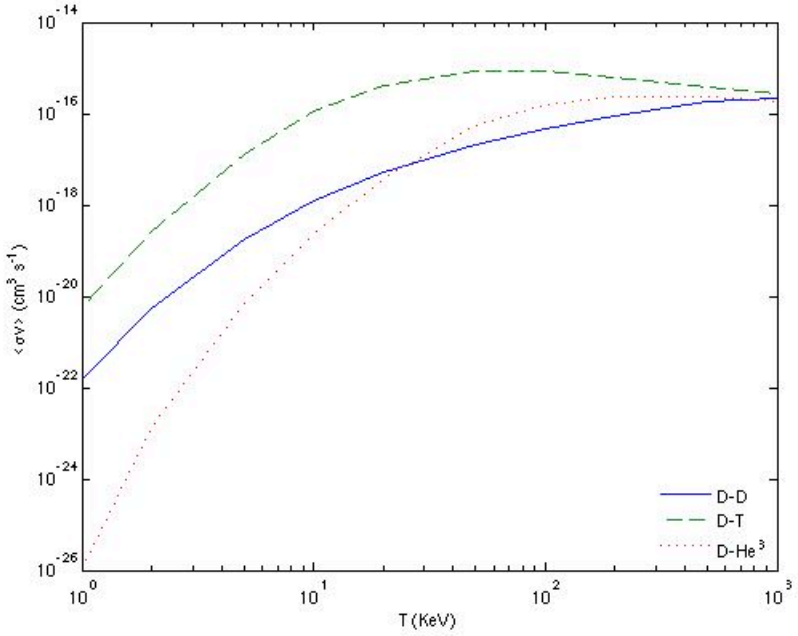

Figure 1.3: Fusion cross sections

and confinement times, while on Earth we must resort to more novel methods to achieve the required parameters.

1.3 Confinement Schemes

1.3.1 Inertial Confinement Fusion (ICF)

In the inertial confinement method, density and temperature are maximized, at the expense of confinement time. This is achieved by forming a small solid pellet of deuterium and tritium, and placing it at the center of an intense symmetric laser barrage. The lasers superheat the outer layers of the pellet, often a secondary material such as beryllium, which then ablates. This ablation generates a reaction force which compresses the interior D-T pellet to achieve a sufficient density and temperature to achieve ignition. This process can also be achieved using a hohlraum, a hollow cylindrical chamber which re-radiates the laser energy in the x-ray range to achieve target heating (Figure 1.4). The entire process happens

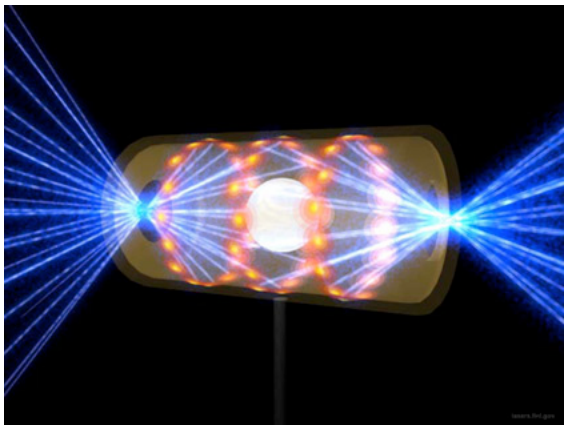

Figure 1.4: NIF Target

on very short timescales, thus immense laser energies are required to reach the density and temperature to meet the Lawson criterion.

The largest such existing experiment is the National Ignition Facility (NIF), located at Lawrence Livermore National Laboratory. This complex uses as system of 192 lasers, operating at 1.8 MJ and 500 TW in the UV range to achieve the required heating power to ignite the D-T pellet . The target, hohlraum, and laser paths are shown in Figure 1.4.

1.3.2 Magnetic Confinement Fusion (MCF)

Another method for confining a plasma, and the one relevant to the remainder of this thesis, involves the use of magnetic fields to confine the plasma and achieve the Lawson criterion. By nature, the diffuse plasma must be much less dense than its solid inertial fusion counterpart, and therefore temperature and confinement time are maximized to obtain the necessary triple product.

Deuterium and tritium gases are injected into a confining vacuum vessel, and breakdown (ionization) is initiated. These particles are then heated through use of ohmic systems, neutral beam injection, or various forms of RF power. The plasma may then be confined by magnetic fields since charged particles will follow magnetic field lines. If fields are arranged in a linear configuration, then particles will be lost when they reach

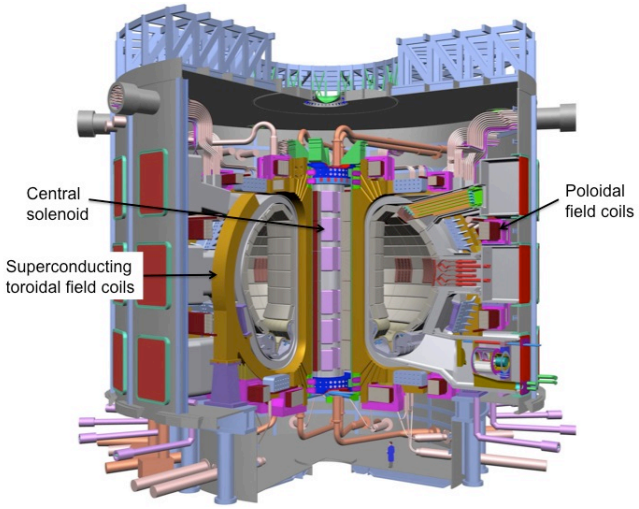

Figure 1.5: ITER Tokamak

the physical walls at the end of the confinement vessel. In order to maintain confinement for the necessary duration, the most widely used magnetic configurations involve scenarios where the fields are bent back upon themselves into a toroidal geometry, thus allowing the particles to circulate indefinitely (unless they are lost by some other mechanism) and achieve the necessary confinement time to satisfy the Lawson criterion.

1.4 The Tokamak and the ST configuration

1.4.1 Traditional Tokamaks

One of the earliest toroidal magnetic field geometries is the tokamak, pioneered in Russia in the 1950s. It consists of a toroidal vacuum chamber, with a central solenoid, toroidal magnetic field coils encircling the chamber, and poloidal field coils for vertical position control. The ITER tokamak, an international reactor currently in construction in Cadarache, France, and representative of the latest concepts in reactor design, is pictured in Figure 1.5.

The basic guide field in a tokamak is oriented in the toroidal direction, although this alone is insufficient to contain the plasma. Various drifts that inhibit confinement act on the

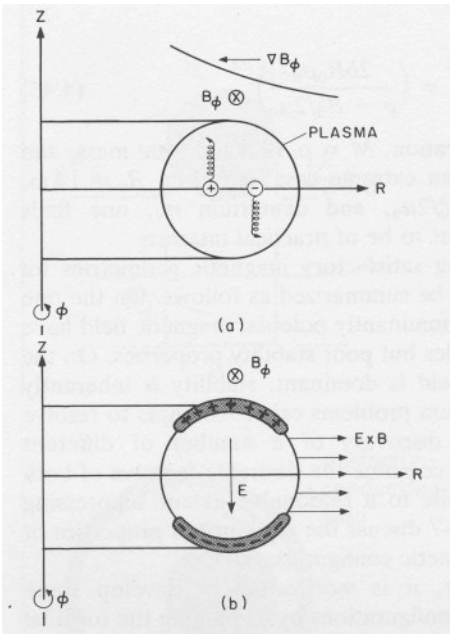

Figure 1.6: Example of how (a) vertical $\nabla \overrightarrow{B}$ drift gives rise to (b) radial $\overrightarrow{E} \times \overrightarrow{B}$ drift [1]

particles as they execute circular motion around the field lines. Two such drifts are caused by the curvature of the field lines and by the gradient in the strength of the magnetic field. Both of these drifts operate in the vertical direction, and act in opposite directions on ions and electrons. These oppositely directed drifts lead to a charge separation in the vertical direction, which then gives rise to a vertically directed electric field. This field gives rise to a further $\overrightarrow{E} \times \overrightarrow{B}$ drift, which occurs in the radial direction and serves to expel particles of both charges from the tokamak. These effects are shown schematically in Figure 1.6. The method for countering this effect is to apply a poloidal magnetic field, which twists the overall configuration into a helical geometry. This geometry serves to counter the vertical drifts by causing the particles to undergo poloidal as well as toroidal transits, and thus after a certain number of orbits end up in their original vertical positions. This is often referred to as the 'twirling honey effect' due to its similarity to method by which a honey stick is swirled to prevent the honey from dripping off of it. This is shown schematically in Figure 1.7.

This field is not supplied by the poloidal field coils, which primarily serve to contain the

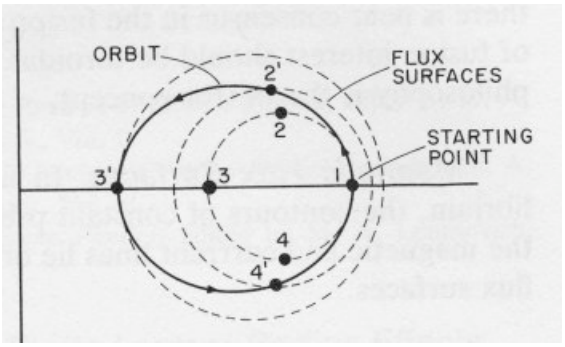

Figure 1.7: Single particle orbit showing drift stabilization by helical field. Unprimed numbers represent motion without drift forces; primed values show particle undergoing poloidal transit with drift motion taken into account. [1]

vertical position of the bulk plasma, but by a toroidal current driven directly in the plasma itself. Ohmic current drive provides an inherently pulsed current drive mechanism, as it generates the main plasma current by employing a central solenoid to create a large change in magnetic flux. This time-changing flux induces a current in the conductive plasma due to Faraday's Law of induction. The power supplies used to generate this flux have limited voltage thresholds, and therefore can only swing within a certain voltage range. Once these voltage limits are reached, there is no further change in flux, and therefore no more current driven in the plasma.

In a traditional tokamak, where the major radius, R, of the device is large compared to the minor radius, a, of the plasma itself, this inductive flux coupling is the primary method of sustaining the plasma current, and thus the discharge can only be sustained as long as this flux can be provided. Fortunately, the plasma is capable of generating its own current, called the bootstrap current. This current is generated by the interaction of magnetically trapped particles with untrapped particles in the presence of a density gradient [19], which naturally exists in toroidal devices. This bootstrap current can be a higher fraction of the necessary current in other magnetic geometries than the large aspect ratio tokamak, chief among them the spherical torus, or ST.

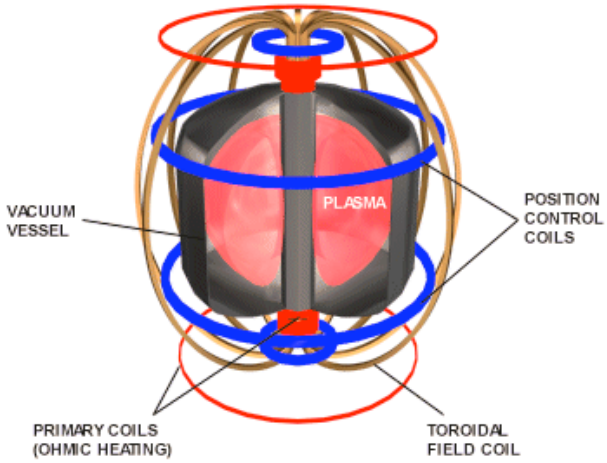

Figure 1.8: Schematic of ETE spherical torus in Brazil

1.4.2 The ST Magnetic Geometry

The spherical torus resembles a traditional tokamak in most respects (toroidal guide field, inductively driven plasma current, vertical shaping coils), but differs mainly in its aspect ratio, A, defined as $\frac{R}{a}$. Whereas tokamaks usually have aspect ratios of 3 or greater, the ST has an aspect ratio of somewhere between 1.25-2. Rather than resembling the donut shape of a tokamak, the ST resembles a cored apple, and is depicted in Figure 1.8. This small aspect ratio provides several advantages over the traditional tokamak, including the ability to maintain a higher β, defined as the ratio of plasma pressure to magnetic pressure. Therefore a larger plasma density and temperature can be sustained with a smaller magnetic field. STs have also demonstrated a higher bootstrap fraction of total current [19], showing the potential to achieve fully non-inductive operation when also utilizing small amounts of supplemental current drive, which can be provided by neutral beams or other radio-frequency heating methods. There are several disadvantages of the ST: the difficulty in operating with superconducting coils due to the small amount of space available in the center of the machine, as well as higher levels of power delivered to the plasma facing components (PFCs) due to the smaller surface area of the power exhaust channel relative to a traditional tokamak. Current research in ST physics is focusing heavily on this issue, as

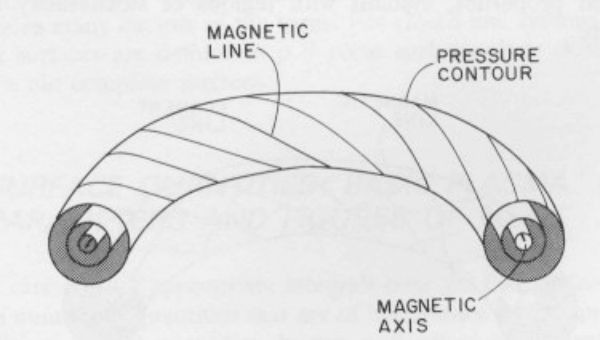

Figure 1.9: Flux surfaces in a toroidal confinement device [1]

its resolution is a key step in the use of STs as viable fusion reactor geometries. This thesis represents an attempt to understand the method by which heat is transferred to the PFCs in the presence of lithium coatings.

1.5 The Plasma Boundary and Lithium

1.5.1 Confinement and recycling

Although the plasma is macroscopically contained in equilibrium by the toroidal and poloidal magnetic fields, there is still transport to the walls. The magnetic field lines form a set of closed magnetic surfaces, also known as flux surfaces, as shown in Figure 1.9. Particles travel along these surfaces as they complete their toroidal and poloidal transits, and are confined in this region. The last closed flux surface, LCFS, represents the outer radial boundary of field lines which close on themselves rather than terminating on a material surface, and any which escape it will ultimately come into contact with the device walls. The plasma that exists outside of the LCFS is referred to as the scrape-off layer (SOL). As particles strike the walls, they can either be adsorbed onto the material surfaces or reflected. Eventually, the surfaces (graphite in the case of NSTX) will become saturated with incident particles, and any new particles that hit the walls will knock out some of these now cold neutral particles, a process known as recycling. The escaped ions can also sputter neutral

atoms from the tiles or surfaces that comprise the walls themselves, providing a source of impurities into the plasma.

These cold neutrals of any species can then penetrate some depth into the plasma, where they are ionized and either expelled again or transported deeper into the core. If the recycled atoms are of the same plasma species, they provide an often unwanted additional fueling source, complicating density control. Carbon walls, as discussed in more detail in Chapter 3, are utilized as the first wall in NSTX and many fusion devices and are a high recycling surface for hydrogenic species. In addition, since carbon is a higher Z element, any that is sputtered into the plasma will not be fully stripped of its electrons and will contribute to energy loss in the form of line radiation (this is also true for other PFC materials such as stainless steel). It is thus desirable to have a first wall that is of a material with low ionization energy, limiting its penetration depth into the core, and which is able to strongly bind with expelled D or T ions to reduce the rate of recycling into the plasma. Lithium has been identified as just such a candidate material. Recycling and associated phenomena are discussed more thoroughly in Chapter 3.

1.5.2 Lithium for use in fusion devices

The absorbing boundary conditions provided by lithium-conditioned walls have been investigated by various devices world-wide. This lithium research has generally focused on solid lithium coatings applied either through evaporation or direct plasma deposition. The relevant bond formed with a hydrogenic species is:

$$2Li + H_2^x \longrightarrow 2LiH^x \tag{1.9}$$

Other bonding mechanisms involving different compounds or weaker bonds are currently the subject of active research [20]. The issue with solid lithium coatings, however, is that the static surface can saturate with incident particles much in the same way that conven-

tional PFCs will. This is not entirely deleterious: although the surface cannot absorb any more deuterium, the high bonding energy keeps the already trapped particles entrained.

This saturation of the solid surface necessitates frequent reapplication of the lithium surfaces, a concept that is inherently inimical to steady state operation. One idea for mitigation of surface saturation is the move liquid lithium PFCs. Such a liquid surface is desirable as the incident deuterium will be trapped in solution throughout the liquid rather than solely as a surface layer. NSTX is currently investigating just such a surface with the installation of the Liquid Lithium Divertor (LLD) described later in Chapter 3.

Lithium is an attractive first wall for a fusion device not only for the reasons mentioned above, but also because of its ability to breed tritium when bombarded with fast neutrons, as described in Section 1.2.2. The ability to make such a surface comprised of a flowing liquid would greatly enhance the benefits of lithium. Not only would this allow for sustained operation, since a fresh lithium surface would always be presented to the plasma, but it would also provide a means of tritium breeding and extraction. A flowing surface also has the advantage of avoiding the materials defects that arise when the first wall is subjected to intense neutron flux, since it will constantly be replenished, contributing further to potential steady-state operation.

Liquid (as opposed to solid) lithium walls, however, been studied in large-scale machines. The modifications to the edge plasma density and temperature caused by these walls could be a key motivating factor in their continued usage. In addition, the way that they alter the heat flux to the material surfaces is of great interest in large-scale machines with large amounts of exhaust power. The diagnostics installed in NSTX for the 2010 run campaign allowed high temporal and spatial resolution measurements of edge plasma parameters to be made for the first time. These measurements were used in concert with IR camera measurements to asses the mechanisms involved in SOL and divertor heat transport, particularly the value of the sheath heat transmission coefficient (discussed in Chapter 2), a measurement of how particles carry energy out of the plasma to the material surfaces.

1.6 Thesis Objective

The role of this thesis is to asses the magnitude and method of the transport of heat flux to the material divertor surface of NSTX during the application of lithium to PFCs, utilizing a dense Langmuir probe array and an IR camera. Chapter 2 provides the physics background for edge plasma studies, recycling, and Langmuir probe theory. Chapter 3 discusses the NSTX device, previous work with lithium in the machine, and the design of the LLD. Chapter 4 discusses the probe array itself, including considerations in the design process and the methodology of its construction and installation. Chapter 5 presents the data analysis methods employed in interpreting and utilizing the probe and camera data. Chapter 6 presents the data and the derived measurement of the sheath heat transmission coefficient, which provides a measure of the amount of energy transported to the PFCs by electrons and ions. Lithium has the potential to alter this coefficient by changing the edge plasma parameters or the method by which heat is transported in the edge plasma. Chapter 7 presents the synthesis of the results and a discussion the observed value of the sheath heat transmission coefficient.

Chapter 2

The Plasma-Material Interface

Although fusion plasmas generally exist in a vacuum in the ideal sense, the confinement scheme necessary to contain them is generated and surrounded by a physical device with which the plasma is forced to interact. As described in the previous chapter, in magnetic confinement fusion energy (MFE), toroidal and poloidal magnetic fields are employed to provide plasma stability and confinement. Despite the general efficacy of these confinement methods, cross-field diffusion and turbulence drive particles outside of the region where closed field lines can be maintained, placing them on trajectories to intersect with the surrounding material surfaces. Since it would greatly reduce the lifetime of the vacuum vessel components and the coils that generate the fields for these to be the first components that ejected particles encounter, various wall materials and and geometric schemes are utilized to provide surfaces with which the plasma can first contact. These surfaces collectively make up the plasma-material interface (PMI), and play a vital role in the successful operation of MFE machines.

2.1 The Scrape-off Layer (SOL)

As discussed in Chapter 1, in the core of a tokamak plasma, all field lines eventually close upon themselves, forcing particles to maintain trajectories that infinitely loop around the

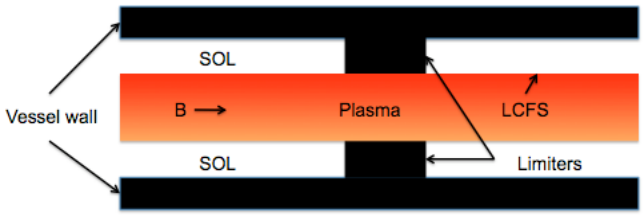

Figure 2.1: Schematic of a limited plasma

torus. This region is spatially finite, however, and has an outermost flux surface referred to as the last closed flux surface (LCFS). The plasma scrape-off layer, henceforth referred to as the SOL, represents the region of the plasma outside the LCFS where magnetic field lines terminate on material surfaces rather than themselves. Thus, any particle travelling on such a field line (if not transported radially inward back to the bulk plasma) will eventually contact whatever material surface that field line happens to close upon. The SOL extends from the LCFS all the way up to the material wall. Therefore, all power and particles leaving the plasma must eventually pass through this region, and it is the processes which govern the SOL characteristics that affect the power and particle flux to the material surfaces, as well as the confinement parameters of the plasma as a whole.

2.1.1 The limiter and divertor geometries

Two basic approaches are used to set the LCFS in modern tokamaks: limiters and divertors. In the limited case, the LCFS of the plasma is defined by the material surface with which it comes into contact - thus, the magnetic extent of confinement is literally limited by the position of the limiting surface. Figure 2.1 depicts a limited plasma configuration. The plasma flows along the magnetic field lines, but any particles transported radially outward of the limiter radius are no longer confined. Plasma still exists in this unconfined SOL region, but the particles are generally on a trajectory to intersect with either the limiter itself or the material walls.

In the case where the magnetic field angle is normal to the limiter surface, as is shown

in the diagram, the total wetted area will be equal to the area of the limiter surface, which is in turn equal to the cross-sectional area of the SOL. This can be modified if the field is oblique to the surface by a factor of B_θ/B, where B_θ is the poloidal field angle. Thus, the plasma wetted area, $A_{\perp,wet}$, is defined as:

$$A_{\perp,wet} = A_{SOL} B_\theta / B \tag{2.1}$$

If we define the total power leaving the plasma as P_{SOL}, then the heat flux caused by parallel transport (the dominant mechanism) to the limiter surface, $q_\parallel$, is defined as:

$$q_\parallel = P_{SOL}/A_{\perp,wet} \tag{2.2}$$

This is true for any general geometry case, although in the diverted and other more complex geometries the SOL area may be a more complicated function of field angle and flux expansion (see Section 2.1.2) than simply the area of the limiter. The limiter case presented above represents one of the simplest possible geometries. In practice even limiters with flat surfaces do not present an area entirely perpendicular to the field. This serves to increase the plasma wetted area and thus dilute the magnitude of the local heat flux. The limiter has the advantage of being a relatively simple-to-install device that is chosen to maximize both the wetted area and plasma volume within the vacuum chamber and internal to the field coils, since magnetic volume is often one of the most expensive considerations in tokamak design. The materials chosen for the limiter surface are often those that posses high thermal conductivity and are low-Z, such as carbon. Carbon, however, is a high-recycling material which acts as a source of cold neutrals when saturated, and which can also be a source of impurities due to sputtering. A major disadvantage of the limiter geometry in this case is that this source is then in direct contact with the main plasma volume, introducing these recycled neutrals and impurities into the bulk plasma.

The divertor geometry, by contrast, can take advantage of the magnetic geometry to

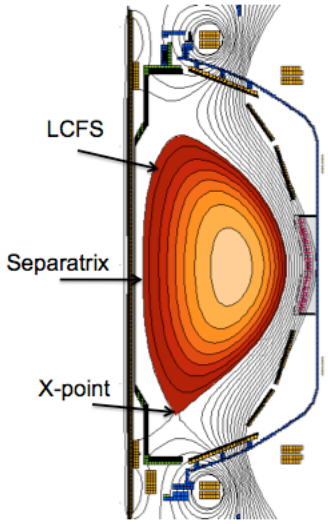

Figure 2.2: Cross-section of NSTX plasma

create a rather large connection length, defined as the distance a particle travels after leaving the LCFS until it strikes a material target. The connection length is:

$$L = \pi R q \tag{2.3}$$

$$q = \frac{r B_t}{R B_\theta} \tag{2.4}$$

where R is the device major radius, and r is the radius of the particular flux surface within the plasma. The safety factor, q, describes the number of toroidal transits a particle makes for every poloidal transit around the device. Since the poloidal field can be made quite weak by design in the divertor region, the connection lengths can be on the order of 100 m or more. A typical plasma cross section in NSTX is shown in Figure 2.2. The innermost flux surface that intersects the device walls is known as the separatrix, and the region where the separatrix field lines intersect is called the X-point, and represents a point where the poloidal field goes to zero and the connection length is essentially infinite. The advantage of having such a large connection length is that the heat removed from the plasma has ample opportunity to be lost through volumetric processes such as radiation and charge

exchange. It also places the recycling (and thus particle) sources far from the main plasma volume, allowing for removal of impurities and cold neutrals through pumping. Its primary disadvantage, when compared to limiter geometry, is that it can consume a large portion of expensive magnetic volume, although this fact is often outweighed by the performance enhancements described above. As the divertor geometry is the one employed in the device used for these studies, it is the one that will be henceforth discussed exclusively.

2.1.2 The SOL in diverted tokamaks

The divertor SOL is marked by several important features that distinguish it from the SOL in limited machines. One such property is the expansion of magnetic flux surfaces, defined as $\frac{(B_\theta/B)_{mid}}{(B_\theta/B)_{target}}$. The flux expansion represents the relative width of a flux tube at the midplane compared to its width at the target, reflecting the change in cross-sectional area due to magnetic geometry effects. Assuming that all power deposited in a flux tube at the midplane (ignoring volumetric losses for the moment) eventually ends up at the divertor target, flux expansion is often useful for reducing the heat flux per unit area at the divertor target, easing the power handling requirements of the PFCs. This can be visualized in Figure 2.3, which shows several of the salient features of diverted SOL geometry, and is a reproduction of Figure 5.23 from P. Stangeby's comprehensive reference, "The Plasma Boundary in Magnetic Fusion Devices" [2]. In addition, the plasma wetted area can be further increased by angling the divertor targets in an orientation that is not normal to the incoming poloidal field, to add to the effect generated by toroidal field angle as described in the previous section. This introduces another factor equal to the scalar product of the poloidal field tangent unit vector with the vector normal to the target. In practice this effect is not nearly as large as that introduced by the toroidal field, but can still increase the plasma wetted area by a factor of 2.

As target (divertor surface) electron temperatures can typically be $\geq 20eV$, ionization of recycled hydrogen neutrals typically occurs at a very short distance from the target. Thus

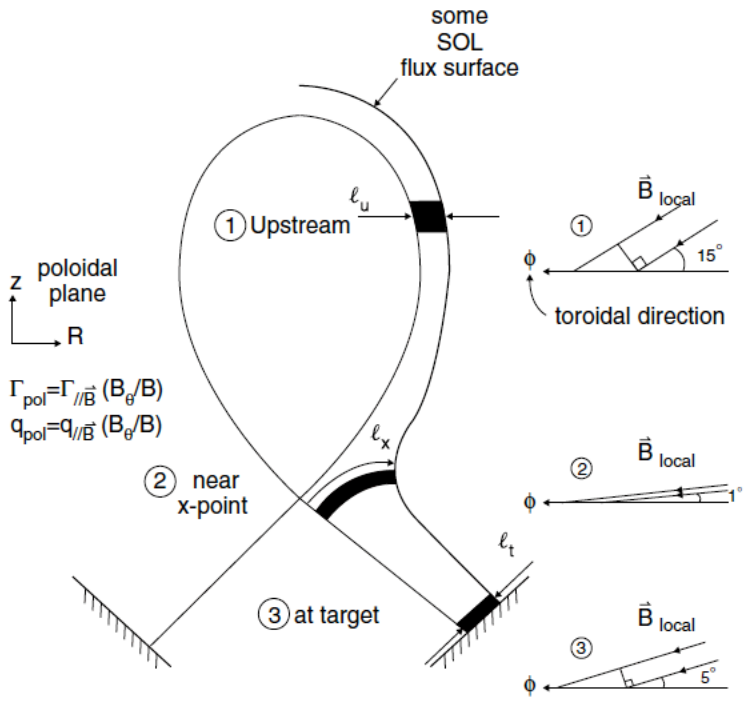

Figure 2.3: Representation of flux expansion in divertor geometry [2]

the particle source due to ionization is typically close to the surface, and much of the density variation occurs in this region. A simple model for this relates the neutral velocity to the neutral collision time, giving the mean free path. The ionization length, λ_{iz} is dependent on both the local temperature and density and is given by:

$$\lambda_{iz} = \frac{v_n}{\left(n_e \overline{\sigma v_{iz}}(T_e)\right)} \tag{2.5}$$

where v_n is the velocity of the recycled neutrals, and $\overline{\sigma v_{iz}}(T_e)$ represents the ionization rate coefficient. This coefficient is a function of the cross-sectional area of the neutrals, as well as the velocity of the ionizing particles, generally assumed to be the electron species (hence the dependence on electron temperature. Other particle sources and sinks due to charge exchange and recombination can also contribute to this picture.

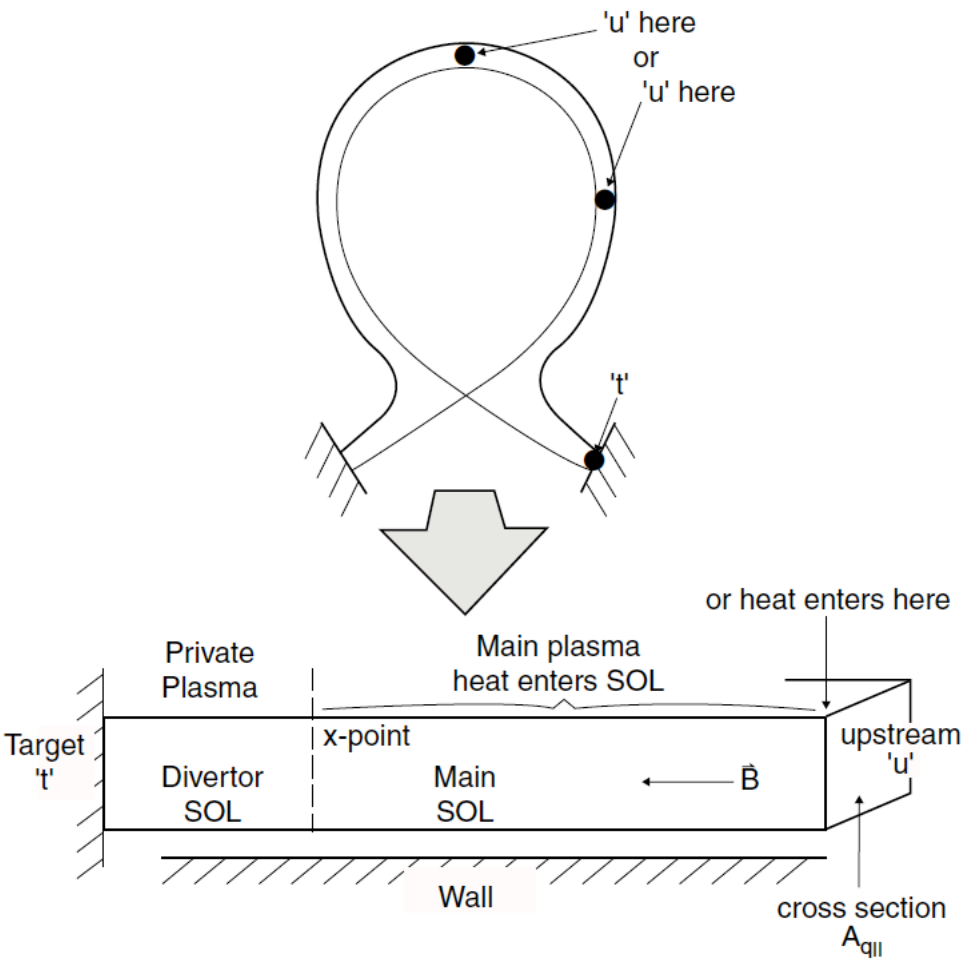

Figure 2.4: Two-point model of a diverted tokamak boundary, showing a cross-section and a straightened out poloidal flux tube

2.2 The Two-Point Model

A classical method known as the 'two-point model', referred to henceforth as 2PM, is often used to evaluate heat and particle transport in the SOL. This model represents a method of subdividing the plasma into two main regions: the upstream region (far from the divertor target) and the target region. It has the advantage of providing profiles for the entire SOL utilizing measurements at only two points, rather than necessitating a suite of diagnostics spanning the whole SOL region. The 2PM is described in greater depth in [2], and shown graphically in Figure 2.4, a reproduction of Figure 5.7 from that reference. The upstream point is also defined as a region of zero fluid velocity, or stagnation point. It is assumed that

heat either all enters at the upstream point or uniformly throughout the flux tube, although the overall effect of the later case only results in about a 20% difference in calculated values. The heat is then transported along field lines past the x-point and into the divertor region, where it eventually comes into contact with the divertor target. The midplane is often chosen as the upstream point rather than the point halfway between the targets. This has a small effect on the results, but leads to a large advantage due to generally greater availability of midplane data.

There are several key assumptions made by the two-point model that need to be briefly discussed. First, it is inherently a steady-state solution and is applicable when a flux tube has come to particle and power equilibrium. In addition, all particles are ionized very close to the target, and this is the only region of net parallel plasma flow. Total pressure is also constant along a flux tube, and generalizing to $T_i = T_e$:

$$p_{tot} = p_{static} + p_{dyn} = 2nkT + nmv^2 \tag{2.6}$$

Equating up- and downstream pressures (and using velocity stagnation upstream and sound speed as the downstream velocity [see Section 2.5]) yields:

$$n_t \left(2kT_t + mc_s^2\right) = 2n_u kT_u \tag{2.7}$$

$$2n_t T_t = n_u T_u. \tag{2.8}$$

If the fluid velocity is small or negligible for most of the SOL length, then heat must be primarily conducted rather than convected, and the heat flux to the (normal-facing) material walls is equal to the parallel heat conduction:

$$q_{\parallel} = \gamma n_t k T_t c_{st} \tag{2.9}$$

where γ is the sheath heat transmission coefficient.

2.2.1 Two-point Model Corrections

The model in this form excludes several loss and source mechanisms of interest, which must also be included if one is interested in a complete treatment. These can generally be thought of as 'fractional' effects, for instance:

$$q_{rad}^{SOL} + q_{cx}^{SOL} = f_{power} q_{\parallel} \tag{2.10}$$

The fractional term describes these processes as some constant relation to the overall heat transport or momentum. Terms treated in this way are the volumetric power losses just described, the fraction of heat that is conducted rather than convected (generally ~1 in the conduction-limited regime), and a fraction of momentum loss due to neutral friction, viscous forces, and volume recombination. These terms can be incorporated with little difficulty into the 2PM equations, as described in [2]. The energy lost through recycling can also be included to refine the assumption that all particles recycled re-enter the plasma with the same energy they had initially. This can make additional contributions to the momentum factor described above, and can cause errors of 33% or more [2].

2.3 SOL Regimes of Interest

In general, regardless of the edge geometry, all power and particles leaving the plasma are introduced into the SOL by perpendicular transport from the bulk plasma. The particles carry this heat either by means of convection or conduction primarily in the direction parallel to the magnetic field. As all field lines in this region terminate on material surfaces, the plasma power is eventually deposited on the PFCs in the form of heat flux, the magnitude of which can be modified by causing the field lines to intersect the PFCs at oblique angles. It is very important to distinguish, however, the means by which the heat is transferred from the upstream (midplane) region of the plasma to the divertor target. The first regime of inter-

est for our present analysis is the sheath-limited regime, in which temperature is constant along field lines until very close to the target and heat transport is primarily convective. In contrast, the conduction-limited regime is characterized by collisional interactions that cause a temperature gradient to appear. These collisions then cause heat transfer primarily through conduction. In both cases, if viscosity and ionization effects are ignored, the sum of static and dynamic pressures are assumed to be constant (Equation 2.6 along a flux tube (essentially a piece of a flux surface given some radial depth). There exists a third case, known as the detached divertor. This is marked by high recycling, neutral pressures, and radiated power, and is where pressure gradients along flux tubes often arise. This can often occur on the inboard divertor leg in NSTX, but as our measurements are primarily located on the outboard side, this case will not be discussed in detail.

2.3.1 Sheath-limited SOL

As previously discussed, sheath heat transport is often governed by collisionality, which determines whether particles can free-stream to the targets or transfer their energy through collisions. If self-collisions are assumed to dominate over cross-species collisions, then an effective collisionality can be defined as:

$$\nu^*_{SOL,e} = L/\lambda_{ee} = 10^{-16} n_u L/T^2_{eu}, \quad \nu^*_{SOL,i} = L/\lambda_{ei} = 10^{-16} n_u L/T^2_{iu} \tag{2.11}$$

where $\nu*_{SOL,e}$ and $\nu*_{SOL,i}$ represent the electron and ion self-collisionalities, respectively. If the ion and electron temperatures are assumed to be equal, then these two values will naturally be equal as well. Since low collisionality equates to small temperature gradients, $T_u \leq 1.5T_t$, and high collisionality to large gradients, $T_u \leq 3T_t$, we can define the transition collisionality from sheath to conduction-limited as $\nu^*_{SOL} \sim 10-15$ [2].

The term 'sheath-limited' arises from the fact that all of the plasma heat is transmitted through the sheath. The Bohm criterion [21] states that particles must enter the sheath at a

velocity equal or greater to the sound speed (see Section 2.5). Since the two-point model assumes stagnation (v = 0) at the upstream point, one can take the simple model of linearly increasing velocity throughout the SOL approaching the target, giving an average velocity of $\frac{1}{2}c_s$. If the particle lifetime is defined as the particle content divided by the particle outflux (a generic form for this quantity), then:

$$\tau_{SOL} = \frac{n_{\bar{SOL}}L}{\frac{1}{2}n_0 c_s} \approx L/c_s$$

The simplicity of this model allows for ease of computation of many scale lengths and other quantities analytically, but often fails to include many realistic effects that complicate the SOL transport properties. These assumptions include: T_i and T_e decoupled from one another due to weak collisionality, no volumetric loss processes, no ionization, recombination, or neutral friction within the SOL - generally constant profiles everywhere but the sheath. Estimating the SOL by such a regime may be more appropriate for limiter machines, but the divertor geometry (and parameters in many such machines) demands a more rigorous treatment. The densities and connection lengths in these machines can be quite high, causing ν^* to exceed the value at which the conduction-limited regime dominates.

Lithium, however, represents a means of decreasing edge collisionality by lowering edge densities and raising edge temperatures (see Section 2.7 and Chapter 3). Although the version of the sheath-limited model discussed here ignores many of the complexities of the SOL, the observations discussed in the concluding chapters of this thesis point towards a less collisional SOL which may require a more thorough kinetic treatment to fully analyze. Therefore, in the present analysis the conduction-limited regime will be examined, since it includes many contributing factors present in real-world devices.

2.3.2 Conduction-limited SOL

When $\nu^*_{SOL} \gtrsim 15$, significant temperature gradients can arise in the SOL due to heat transfer being limited to conduction through particle collisions. This regime is therefore called the conduction-limited regime. Following the derivation from [2], the generic equation for parallel heat conductivity is given by:

$$q_{\parallel cond} = P_{SOL}/A_{q\parallel} = -\kappa_0 T^{5/2} \frac{dT}{ds_\parallel} \tag{2.12}$$

where $s_\parallel$ is the coordinate along the magnetic field and in our straightened geometry. Since the electron thermal conductivity constant, κ_{0e}, has a value of ~2000 (compared to $\kappa_{0i} \sim$ 60), electron heat conduction is assumed to be dominant and this equation can be solved for both the upstream and downstream boundary cases. Given the exponent of 7/2 that will arise in the solutions, even a small change in T_u vs. T_t will make the latter term much smaller, and the two solutions can be equated to give:

$$T_u = \left(\frac{7}{2} \frac{q_\parallel L}{\kappa_{0e}} \right)^{2/7} \tag{2.13}$$

This assumes that all heat enters at the upstream point, but a more complex treatment in which the heat enters uniformly throughout the flux tube merely serves to change the multiplicative factor of $7/2 \rightarrow 7/4$, leaving the much stronger exponential effect unchanged. The most complex case of heat entering asymmetrically throughout the flux tube generally requires a computational approach that precludes simple analytic solutions. This result shows that the upstream temperature should change very little even for large changes in heat flux, and is independent of the density as well. The strong dependence of heat conduction on temperature ensures that the upstream region must maintain a high temperature to efficiently remove the plasma heat.

Combining Eq. 2.7, 2.9, and 2.13, one can find a result for the target temperature:

$$T_t = \frac{m_i}{2e} \frac{4q_\parallel^2 \left(\frac{7}{2}\frac{q_\parallel L}{\kappa_{0e}}\right)^{-4/7}}{\gamma^2 e^2 n_u^2} \tag{2.14}$$

This indicates a quasi-linear relationship between heat flux and target temperature, but a strong inverse relationship with upstream density. This equation can also provide a direct solution method for upstream density if the target temperature (from Langmuir probes) and parallel heat flux (from IR camera data) are known. Lastly, if we define the flux to the target as $\Gamma_t = c_{st} n_t$, we can combine Eq. 2.9 and 2.14 to give:

$$\Gamma_t = \frac{n_u^2}{q_\parallel} \left(\frac{7}{2}\frac{q_\parallel L}{\kappa_{0e}}\right)^{4/7} \frac{\gamma e^2}{2m_i} \tag{2.15}$$

This indicates that the target flux is a strong function of upstream density in the conduction-limited regime. A relationship between $\bar{n}_e$ and n_u (often empirical) would allow this relationship to be entirely given in terms of known quantities and could provide scaling-law guidelines for plasma performance.

Since it is often a given that all incident ions are recycled as neutrals (more on this in Section 2.7), the conduction-limited regime is often also referred to as the 'high-recycling' regime, as the target flux scales as n_u^2, or perhaps as αn_u^2, where α is an empirically derived constant. If we use this relation, then using our definition of particle lifetime as (total plasma content/outward flux), we come to the equation:

$$\tau_p = \frac{\alpha q_\parallel}{n_u (\frac{7}{2} q_\parallel L/\kappa_{0e})^{4/7}} \frac{2m_i}{\gamma e^2} \frac{volume}{A_{wet}(B_\theta/B)_t} \tag{2.16}$$

This shows that with the assumptions we have made, cross-field transport is decoupled from particle transport (i.e., no heat or particle diffusivity coefficients involved in the particle lifetime) - thus energy and particle confinement are not necessarily related [2].

2.4 SOL Profiles and Dependencies on P_{SOL} in the Conduction-Limited SOL

A simple geometric and first-principles consideration relating the power into the SOL is given by [2]:

$$P_{SOL} \approx A_{\perp} n_u \chi_{\perp} k T_u / \lambda_{T_u} \tag{2.17}$$

where $\chi_{\perp}$ is the plasma thermal diffusivity, and λ_{T_u} is the scale length of the temperature gradient at the upstream point, given by:

$$\lambda_{T_u} = -\left(\frac{1}{T_u}\frac{\partial T_u}{\partial r}\right)^{-1} \tag{2.18}$$

This is the generic expression for scale lengths that will be used for the remainder of this thesis, essentially representing the logarithmic derivative of a given quantity. If one applies this method to the relationship between T and $q_{\parallel}$, then it emerges that $\lambda_{q_{\parallel}} = \frac{2}{7}\lambda_T$. In the assumption that all other quantities in (2.17) are held fixed, then the heat flux scale length will decrease as power into the SOL increases, meaning that the heat flux to the material targets will grow at least as fast as the input power. This is already a concern for present-generation devices, not to mention ITER and reactor-scale machines, where heat fluxes can reach $> 10 MW/m^2$ under steady-state operation [22]. Transient heat fluxes can exceed this by at least a factor of 2, or by even higher amounts during thermal quenches. Though carbon and refractory metal PFCs can withstand high transient fluxes, the steady-state operation of fusion reactors will require materials that can withstand these fluxes on a time scale long enough to ensure a high duty cycle and cost-effective energy.

One can utilize several methods to relate the power into the SOL to the temperature and density profiles and various scale lengths. The methods will be briefly presented here, as well as the general results, but the full derivations can be found in Section 5.7.3 in [2]. The

first method invokes a simple model of diffusive heat transport:

$$\lambda_{q_\parallel} = (\chi_\perp \tau_E^{SOL})^{1/2} \tag{2.19}$$

where the energy confinement time in the SOL is derived from the standard form of (total energy content of SOL/SOL power). One can also utilize power conservation:

$$\frac{dq_\perp}{ds_\perp} = -\frac{dq_\parallel}{ds_\parallel}. \tag{2.20}$$

In this case, all heat transported into the SOL from the main plasma must be conducted along field lines to the target surfaces. The final method combines the equations for upstream temperature, heat and temperature scale lengths, SOL power, and parallel SOL heat flux area. Despite these different assumptions, the methods result in fairly similar final scaling laws, which will be summarized here.

$$\lambda_{q_\parallel} \propto P_{SOL}^{-5/9} (n_u \chi_\perp^{SOL})^{7/9} \tag{2.21}$$

This indicates, as above, that more SOL power results in a narrower power deposition channel, and thus greater heat flux. This can be countered, however, by increases in upstream density and perpendicular heat diffusivity, which will generally serve to increase the spatial extent of the power deposition.

$$n_t \propto n_u^4 / P_{SOL}^{3/2}. \tag{2.22}$$

Further applying these relations yields to the flux to the target -$\Gamma_t \propto n_u^2$, which is in keeping with our earlier assessments.

These quantities represent testable relations that can be verified using Langmuir probe, IR, and Thomson scattering measurements. Ultimately, however, these relations are the result of simple modeling with many assumptions and are steady-state solutions of the fluid equations with only two points of reference.

2.5 Sheath physics

The plasma sheath is a region, typically a few Debye lengths thick, which forms around all plasma-material interfaces. The sheath forms as a result of the much greater electron mobility as compared to that of ions. As plasma electrons impact the surface, they begin to charge it to a negative voltage, which serves to repel further electrons and attract ions as an electric field develops. This electric field ensures that there is zero net flux of charge, therefore forcing (assuming that the ion charge, Z, is 1) $\Gamma_e = \Gamma_i$.

2.5.1 Velocity and density distributions for electrons and ions

In Section 1.8.2.2 of [2], it is shown that by taking the electron fluid momentum equation and neglecting all terms except the dominant pressure and electric field terms, one can demonstrate that the electrons follow a Boltzmann factor distribution:

$$n_e = n_0 e^{(eV/kT_e)} \tag{2.23}$$

The derivation of the sheath electric field begins with the condition that the electrons, suffering sufficient collisions, will develop a Maxwellian velocity distribution of the form (in 1D):

$$f_e(v_x) = n_o(m/2\pi kT_e)^{1/2} e^{-\frac{m}{2kT}v_x^2} \tag{2.24}$$

Taking the first moment of this equation by finding the average velocity in the x direction, one finds:

$$\bar{c_e} = \left(\frac{8kT}{\pi m_e}\right)^{1/2} \tag{2.25}$$

Solving the ion fluid equations yields a more complex distribution for the ion velocity in the SOL (the ion density follows the more simple relation of $Zn_i = n_e$, since quasi-neutrality is preserved), but a simple relation in the sheath can be found. Utilizing particle and energy

conservation, one can derive a form for the ion density:

$$n_i = n_{se}(v_{se}/v)^{1/2} \tag{2.26}$$

where the *se* subscript denotes the value of a quantity at the sheath edge, with the ion density at the sheath edge equalling the electron as quasi-neutrality still holds in this region. Utilizing Poisson's equation, one then finds that in order for a stable, non-oscillatory, solution to the electric field to exist, all ions must enter the sheath with at least the sound speed, c_s, given by:

$$v_{i,se} \geq c_s = \sqrt{\frac{k(T_e + T_i)}{m_i}} \tag{2.27}$$

This relationship is known as the Bohm criterion [21]. Comparing the sound speed to the electron velocity and assuming the densities are initially equal, it is clear that the surface will quickly become inundated with electrons and acquire a negative charge, as the electron mass is the much smaller. This will generate the sheath electric field in order to ensure a zero net current to the surface, which will charge up to the floating potential, V_f, in order to create the field. In the case of hydrogenic ions and $T_e = T_i$, $V_f \approx V_{sp} - 3kT_e/e$. That is, the surface floats at a potential approximately $-3kT_e/e$ lower than V_{sp}, the space potential of the plasma. Debye shielding attempts to prevent this potential from penetrating into the plasma, and sets the scale length for the sheath, which is typically on the order of several λ_D. A small electric field still penetrates into the plasma, yielding a further pre-sheath potential drop of $\sim -0.7kT_e/e$.

2.5.2 Power and particle transmission through the sheath

If one can estimate the total energy carried by electrons and ions, then the heat flux through the sheath can be calculated. Taking the second moment of a Maxwellian distribution

function to find the one dimensional random heat flux yields:

$$q = 2kT\Gamma \tag{2.28}$$

In the case of a thin, simple sheath with no electron reflection or secondary emission, the flow of electrons into the sheath edge is the same as that to the surface:

$$q^e_{ss} = 2kT_e\Gamma_{se} = 2kT_e\Gamma_{ss} \tag{2.29}$$

This, however, differs from the flow of heat into the sheath edge, which is given by:

$$q^e_{se} = (2kT_e + e|V_f + V_{pre}|)\Gamma_{se} \tag{2.30}$$

Equation 2.30 indicates that electrons with sufficient energy to overcome the repelling potential of the floating surface will be lost at the surface, and thus need to have an energy that is higher by a factor of $|eV_f|$. There is also a contribution to the energy from the pre-sheath potential drop, reflected in the second potential term. All of these factors are folded into a more generic term for the electron heat flux to the sheath:

$$q^e_{se} = \gamma_e kT_e\Gamma_e \tag{2.31}$$

$$\gamma_e = 2 + \left|\frac{eV_f}{kT_e} + \frac{eV_{pre}}{kT_e}\right| \approx 5 - 6 \tag{2.32}$$

This is in contrast to $\gamma_{ss} \sim 2$, which means the electron heat flow into the sheath is significantly higher than the flow to the surface. This excess heat is transferred to the ions through the electric field, which serves to accelerate the ions, but must be maintained by power extracted from the electrons. The corresponding analysis for ions gives:

$$q^i_{se} = \left(2kT_i + \frac{1}{2}m_i c_s^2\right)\Gamma_{se} \tag{2.33}$$

This corresponds to $\gamma_i \sim 2-3$, and reinforces the notion that most of the power flow into the sheath is due to electrons, but that the sheath serves to transfer this energy to the ions, which are dominantly responsible for the power flow to the solid surface.

If the sheath is thin (no volumetric heat losses), this heat flow into the sheath edge is not lost, but rather all heat entering the sheath flows to the material wall. Thus if the flow into the sheath edge is known, this can be converted in a sheath heat transmission coefficient, γ, which combines the effects of electron and ion power removal from the plasma to determine the amount that will eventually impact the solid surface. Taking the definition of V_f as the condition when the electron and ion currents are equal and including a secondary electron emission coefficient, δ_e, this value can be quantified as:

$$\gamma = 2.5\frac{T_i}{T_e} + \frac{2}{1-\delta_e} - 0.5\ln\left[\left(\frac{2\pi m_e}{m_i}\right)\left(1+\frac{T_i}{T_e}\right)\left(\frac{2}{(1-\delta_e)^2}\right)\right]. \tag{2.34}$$

The net heat flux to a surface is therefore:

$$q = \gamma k T_e \Gamma \tag{2.35}$$

With the assumptions of $T_i = T_e$ and $\delta_e = 0$, the predicted value of γ is approximately 7. It is this value that this thesis will attempt to measure empirically to help quantify the mechanism of heat flux to PFCs. To do so requires the use of multiple diagnostics, namely an IR camera to measure the heat flux to the surface and Langmuir probes to measure the electron temperature and particle flux at the target.

2.6 Langmuir probe theory

2.6.1 Single probes

Proposed by Mott-Smith and Langmuir in a 1926 paper [23], a Langmuir probe represents one of the simplest and most widely utilized plasma diagnostics. A single Langmuir probe consists of an electrode inserted into a plasma, usually in a region where the heat flux from the plasma will not cause it material harm. A swept bias voltage is applied to this electrode, which attracts either electrons or ions. In the simplest case, we can deal with an unmagnetized plasma, or one where the flux is perpendicular to the probe surface.

The region of the current vs. voltage curve chosen for temperature measurement is generally that where the electron current is growing exponentially. In this case, the electron current to the probe surface will be given by that of Maxwellian flow where the density depends on the voltage:

$$I_e = \frac{e n_{se} \bar{c}_e}{4} e^{\frac{-e(V_{sp}-V_B)}{kT_e}} A_p \tag{2.36}$$

where V_{sp} is the space potential of the plasma, which is essentially higher than the floating potential by a constant factor, and includes the potential drop of the pre-sheath and sheath as described above in Section 2.5. V_B is the bias voltage applied to the probe, and it is this potential drop between the plasma and the surface that sets the electron density in the Maxwellian distribution, and determines the electron current to the probe tip. A_p is the area of the probe itself, which in the perpendicular case is simply a multiplier of the current density.

The ion current to the tip is dependent on the electron density (and hence the space potential relative to the floating potential as well) and the sound speed. It is generally assumed that the probe voltage is not strong enough to repel ions, and that all ions entering the sheath impact the probe surface. The sound speed is essentially what sets the sheath bias, as the electric field exists to accelerate ions to this speed and maintain $v_i n_i = v_e n_e$ at

the probe tip, we can define:

$$c_s = \sqrt{\frac{k\left(T_e + T_i\right)}{m_i}}. \tag{2.37}$$

At floating potential, to ensure the ion and electron currents are equal, this also ensures that:

$$n_i c_s = \frac{1}{4} n_s \overline{c_e} e^{\frac{eV_f}{kT_e}} \tag{2.38}$$

The ion current can then be obtained by considering only the potential drop from the plasma to the surface:

$$I_i = \frac{1}{4} n_s \overline{c_e} e^{\frac{eV_f}{kT_e}} A_p. \tag{2.39}$$

Combining the ion current with the electron current, condensing the space and floating potential terms, and using the fact that $n_s \sim \frac{n_0}{2}$ yields:

$$I_p = I_i - I_e = \frac{1}{2} e n_0 c_s \left(1 - e^{\left[\frac{e(V_B - V_f)}{kT_e}\right]}\right) A_p \tag{2.40}$$

Equation 2.40 is referred to as the Langmuir probe characteristic, which is the total current to the probe tip. The current is zero when the probe bias equals the floating potential, and reduces to the ion saturation current

$$I_{is} = \frac{1}{2} n_0 c_s A_p \tag{2.41}$$

at sufficiently negative voltages. The temperature can be simply derived from the characteristic equation by measuring the current produced at a certain voltage. The entire I-V trace is often obtained by sweeping the probe voltage, and this curve can then be fit with the temperature as a free parameter in order to determine its value. The ion saturation current (I_{sat}) is generally taken at the lowest voltage point on the curve. It is used in combination with the sound speed as determined from the electron temperature to deduce the density. Note that much of this analysis depends on $T_i = T_e$, although corrections are possible, to

determine the plasma density as well.

An additional correction can come in the form of a secondary electron coefficient, δ_e, which represents the fractional number of electrons emitted from the surface for every electron impact. This serves to reduce the net electron current by a factor of $1-\delta_e$ and thus push the floating potential closer to the space potential by a factor of $(1-\delta_e)^2$. As the ion flow to the surface in ion saturation is not affected by electron flow, the secondary electron emission does not tend to change the measured density. It can have an impact on the measured temperature due to the altered potential, but unless $\delta_e \rightarrow 1$, the effect is not large and generally ignored.

2.6.2 Double probes

A double Langmuir probe consists of two single probe tips biased with respect to each other and floating with respect to ground. They each draw an individual current as described in Equation 2.40, but now since the whole system draws no net current with respect to ground (as it is floating), $I_{p,1} = -I_{p,2}$ and $V_{B,1} - V_{B,2} = V_B$ (i.e., $V_{B,1} = -V_{B,2} = |V_B/2|$). This bias voltage actually represents the bias about the floating potential, thus $V_{tot} = V_f + V_B$. Taking the probe characteristics for each of the two probes, substituting in these voltages, and setting them equal to the negative of each other yields:

$$I_p = I_{sat} \tanh\left(\frac{eV_B}{2kT_e}\right) \tag{2.42}$$

where $I_p = (I_{p,1} - I_{p,2})/2$. Thus a plot of the sweep of I_p *vs.* V_B yields a hyperbolic tangent curve that can then be fit to yield the electron temperature. One could also simply take the derivative of the current with $V_B = 0$. This method has the advantage that it draws the much smaller ion saturation current, and does not perturb the plasma nearly as much as a single probe drawing the greater electron currents. It also limits the current to each electrode to the magnitude of I_{sat}, and therefore reduces the risk of an over-current or damage to

the probes. A disadvantage of the double probe is that one must assume that there are no variations in the plasma parameters at the different locations, and that one has the available space and resources to construct two separate probe tips.

2.6.3 Triple probes

The triple probe represents a further refinement of the double probe by adding an additional tip whose sole purpose is to measure the floating potential of the plasma. Since the floating potential is now known, the exact voltage of the two individual tips is also known and it is no longer necessary to obtain multiple voltage points during a sweep in order to deduce the electron temperature. Using the relation from above, which states that the currents into the two biased tips are equal and opposite, and that $V_1 - V_2 = V_B$ (where V_B is set by the circuitry), one can derive the relation:

$$e^{\frac{e(V_1-V_f)}{kT_e}}\left[1+e^{\frac{-eV_B}{kT_e}}\right]=2 \tag{2.43}$$

One then assumes that $eV_B \gg kT_e$, allowing the approximation of the exponential and reducing Equation 2.43 to:

$$T_e \simeq \frac{e}{k}\frac{V_1-V_f}{\ln 2} \tag{2.44}$$

With the appropriate circuitry, these quantities can be measured simultaneously and thus produce an instantaneous electron temperature for real-time measurement. Triple probes are commonly operated in 'quadruple-probe' mode, where an additional probe tip is run continuously in ion saturation current to give a plasma density with the known temperature. With the assumption that one of the triple probe tips will always be measuring ion saturation current, due to the relatively low temperatures of the edge plasmas being measured, the density can be determined through the standard method once the temperature is known.

Thus a system of three tips can be used to produce plasma temperature and density measurements at a frequency that is essentially limited only by that of the digitization

system used. Disadvantages are similar to the double probe system, in that one assumes that the plasma parameters are Maxwellian and do not vary greatly in the region that the different probe tips are sampling. This topic will be addressed in great detail in Chapter 4, as a major theme in constructing the triple probe array that is the subject of this thesis was the difficulty of placing many probes in a small area. In addition, the circuitry required for triple probes can become rather complicated, although one does not have to worry about applying a swept voltage, as the two active tips always sit at a constant bias relative to one another. Triple probes are additionally more vulnerable to secondary electron emission, as the emitted electrons will be repelled by one tip while being attracted to another.

2.6.4 Magnetized probe theory

The descriptions so far have dealt with the case of no magnetic field, or a magnetic field exactly perpendicular to the probe surface. In a tokamak, however, this is generally not the case. As was discussed at length above, the magnetic field angle is generally altered with respect to the material surfaces not only by the ratio of the poloidal and toroidal confining fields, but also by the fields which serve to direct particles to the divertor. This oblique magnetic field angle has the beneficial effect of reducing the perpendicular flux to the PFCs, but also complicates the interpretation of probe data as this altered flux magnitude must now be taken into account.

This problem was addressed in a 1981 paper by Chodura [3], and will be described here as it affects Langmuir probe interpretation. In order for the Bohm criterion to be satisfied, ions must enter the electrostatic sheath (simply referred to as the sheath in earlier sections) with a velocity perpendicular to the surface equal to or greater than the sound speed. In the case of a magnetic field, this is not guaranteed by the presence of the electrostatic sheath alone, as the particles now are travelling at an oblique angle and an electric field perpendicular to the wall will no longer suffice. A magnetic pre-sheath (MPS) thus forms in order to deflect the ions into a perpendicular trajectory and maintain the Bohm criterion.

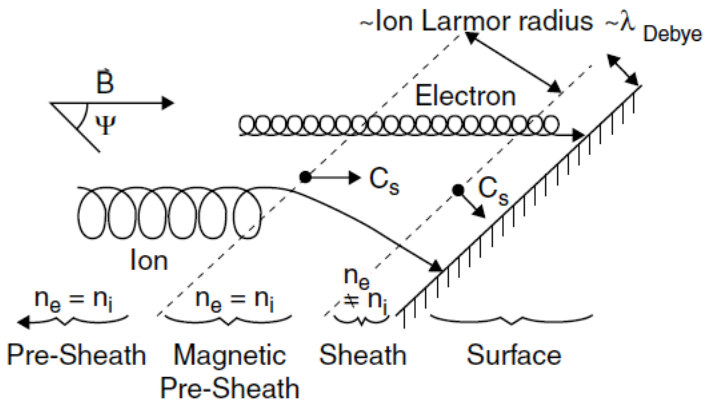

Figure 2.5: The magnetized plasma edge; reproduction of Figure 2.22 [3]

The electrons, being much more strongly tied to the magnetic field lines due to their much smaller mass, are unaffected by the MPS and simply stream along field lines to the surface. These combined effects are shown schematically in Figure 2.5. The scale length of the MPS is set by the ion gyroradius, as compared to the electrostatic sheath, which depends on λ_D. The formula derived using kinetic theory [3] gives:

$$L_{MPS} \simeq \sqrt{6}\frac{c_s m_i}{eB}\sin\psi \tag{2.45}$$

where ψ is the angle between the magnetic field and the surface normal, which reduces L_{MPS} to 0 in the case of a perfectly normal field angle.

The electrons still follow a Maxwellian distribution, and one can calculate their density within the MPS as a function of the voltage drop across it. For the ions, conservation of flux introduces a factor of $\cos\psi$. By combining these two equations, the voltage drop due to the MPS can be calculated, yielding:

$$\frac{eV_{MPS}}{kT_e} = \ln(\cos\psi)\,. \tag{2.46}$$

In NSTX, where the field angles are typically $\sim 5^\circ$, the potential drop in the MPS is approximately $-2.5kT_e/e$, meaning that a significant fraction of the overall potential drop

can occur in this region. Note that the potential drop across the sheath as a whole (and thus the floating potential) remains relatively unchanged, as there is a factor of $\cos\psi$ introduced into both the ion and electron fluxes. This effect therefore cancels out when calculating the potential at which zero net current is drawn. This shifting of the potential drop to the MPS simply indicates that the electric field is now devoting its energy to overcoming the $\mathbf{v} \times \mathbf{B}$ motion of the ions, rather than simply accelerating them to the sound speed. By identifying several instability modes that could grow in the MPS, Chodura proves [3] that in order for a stable solution to exist, a new criterion (the Chodura criterion) must be met to ensure a stable MPS. This is in fact identical to the Bohm criterion - namely that the parallel (to the field) velocity of ions entering the MPS must meet or exceed the sound speed.

The main caveat for probe interpretation is that while the floating potential is unaffected by the presence of the magnetic field, the ion flux to the surface of a flush-mounted Langmuir probe (assumed to be independent of the probe bias) is now reduced by the $\cos\psi$ factor. If this ion saturation current is used to calculate the plasma density, one must then include this angular factor in the effective probe area, as would be required with the effective area reduction of any limiting surface. The incorporation of this effect into probe interpretation will be discussed in detail Chapter 5.

2.7 The effect of lithium on SOL conditions

Nearly all of the analysis discussed above has focused on perfectly recycling wall conditions - all the ion flux reaching the plasma wall is re-emitted as neutrals which re-ionize and return to the plasma (thus creating a steady-state density). This leads to Equation 2.16, which describes the SOL particle lifetime. This equation can be simply modified to reflect a recycling coefficient of less than 1, as it divides the total particle content by the recycled flux. We can define the recycling coefficient R as the fraction of outward flux that returns

to the plasma, such that:

$$\tau_p = \frac{nV}{R\Gamma_{out}}, \tag{2.47}$$

where τ_p is the total particle content divided by the recycled neutral flux back into the plasma. We can also define a particle decay time as:

$$\frac{nV}{\tau_p^*} = -\frac{d(nV)}{dt} \tag{2.48}$$

The time derivative of the particle content is the recycled flux back into the plasma minus the outward ion flux:

$$\frac{d(nV)}{dt} = R\Gamma_{out} - \Gamma_{out} = (1-R)\Gamma_{out}. \tag{2.49}$$

This leads to a definition of the particle decay time of:

$$\tau_p^* = \frac{\tau_p}{1-R} \tag{2.50}$$

This, of course, assumes the simplest possible particle balance where the only source or sink action occurs at the material wall. Appendix A shows a more rigorous derivation of τ_p^* that includes physical pumping of gas as well as core and neutral beam fueling.

The primary effect of lithium, however, is to provide a surface that entrains incident deuterium particles with a much higher efficiency than its graphite counterpart, leading to a reduction in the surface recycling coefficient. Equation 2.49, when solved for the plasma density, predicts an exponential pump-out of deuterium, which must be sustained with external fueling to maintain a constant density. A similar effect can be achieved with extensive helium wall conditioning (albeit lasting for a small number of discharges), and was observed on the Tokamak Fusion Test Reactor (TFTR) [24]. The GDC method of wall cleaning is utilized in NSTX as well, but was eventually supplanted by the application of evaporated lithium coatings.

This reduced recycling can have other far-reaching implications for the overall plasma

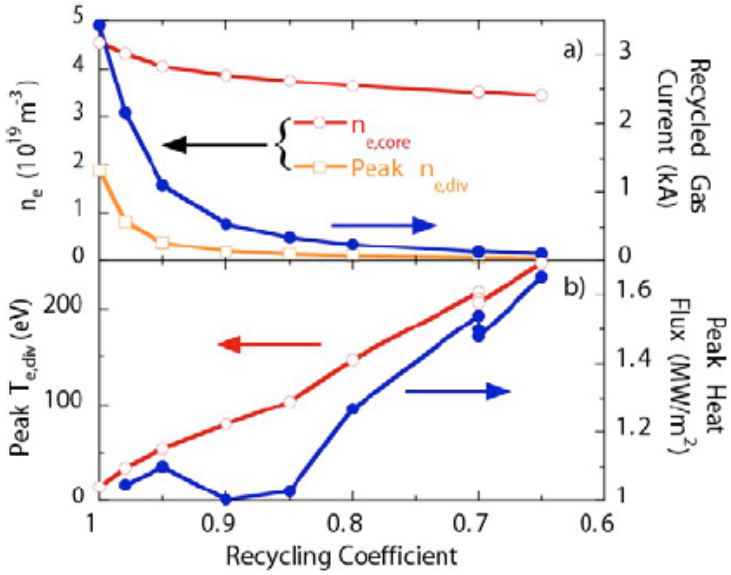

Figure 2.6: The variation in edge parameters with a changing recycling coefficient. Reproduction of Figure 4 in [4]

conditions, namely in the changes to edge plasma density and temperature. Fluid modeling efforts in NSTX have sought to quantify the changing effect on divertor conditions, and early results are shown in Figure 2.6. As R decreases, the divertor plasma density decreases, while the temperature increases. These effects can decrease the value of ν^*_{SOL}, changing the edge collisionality regime and fundamentally altering the way that heat is transported through the SOL to the divertor surfaces. A lower edge collisionality can imply that the high-energy electron population extracted through the sheath can not be replenished in the SOL, decreasing the overall heat flux to the wall and changing the value of γ.

The next chapter focuses on the history of lithium wall conditioning in theory and experiment, and describes the evolution of lithium experiments on NSTX and efforts to improve the utility of evaporated lithium coatings as a component of the PMI.

Chapter 3

NSTX and the Liquid Lithium Divertor (LLD)

3.1 NSTX parameters

The National Spherical Torus eXperiment (NSTX) is one of three large magnetic confinement research devices in the US fusion program, and is the largest spherical torus (ST) in the country. It resides at the Princeton Plasma Physics Laboratory and achieved first plasma in 1999. A summary of its operating parameters for a typical discharge can be found in Table 3.1. A cartoon of the device, with a human shown for scale, is found in Figure 3.1.

3.2 H-mode physics in NSTX

NSTX typically operates in the regime known as H (or high-confinement) mode. This mode of operation was first discovered in the ASDEX tokamak in 1982 [25] and is characterized by a steep temperature and density gradient at the plasma edge, allowing the formation of a hot, dense core region. These steep gradients indicate a region of reduced transport that separates the hot plasma core from the cold edge, and allows for profiles that resem-

Parameter	Value
Major radius (R)	85 cm
Minor radius (a)	67 cm
Plasma current (I_p)	600 - 1200 kA
Pulse length	1 s
Toroidal field	0. 4 - 0. 65 T
Neutral beam (NB) power	6 MW
RF power	6 MW
Divertor heat flux	1 - 10 MW/m^2
Peak electron temperature	1.5 (NB) / 5 (RF) keV
Peak ion temperature	1 - 1.5 keV
Core electron density	$1 - 10 \times 10^{19}/m^3$
Toroidal beta (β_T)	10 - 40 %

Table 3.1: NSTX parameters

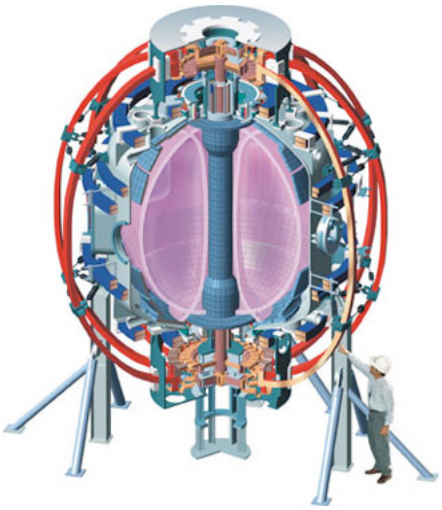

Figure 3.1: Cartoon of NSTX with human

ble step-functions rather than parabolae. The transition region between the relatively flat temperatures and densities of the core and the plasma edge is referred to as the pedestal, which is marked by a sharp decrease in both temperature and density as one moves radially outward. H-mode discharges are obtained in NSTX through neutral beam heating and can typically result in up to a 100% enhancement of the energy confinement time compared to ordinary, or L (low-confinement) mode discharges. The transition from L to H-mode typically occurs early in NSTX discharges, and is the subject of active theoretical and experimental research [26].

3.2.1 Edge Localized Modes

Although H-mode operation offers the promise of better energy confinement and enhanced performance, there are several unfavorable conditions that can result from operating with a large pressure gradient at the plasma edge. The energy principle of ideal MHD states that there are two terms can lead to instability growth: pressure gradients and currents parallel to the magnetic field. The current theoretical understanding attributes edge-localized modes (ELMs) to peeling-ballooning modes associated with these two conditions [27]. In an H-mode, both factors can be present - the pressure gradient results from the steep drop in temperature and density in the pedestal region, while the parallel bootstrap current can result from the pedestal density gradient as mentioned in Section 1.4.2. The ELM-crash that results can expel a portion of the plasma stored energy, from as little as 1% for small ELMs, but up to 15% or more for large ELMs [28]. The energy released in this manner makes its way to the PFCs, depositing very high instantaneous power loads. Recent fast IR camera measurements show that this parallel heat flux can be as high as 70 MW/m^2 at the ELM peak, significantly higher than during quiescent periods [29]. ELMs therefore represent a significant hurdle for reliable H-mode operation, and it is only recently that successful efforts have begun to mitigate and/or suppress them.

3.2.2 Secular density rise

The traditional NSTX divertor consists of ATJ graphite tiles that are an excellent heat sink, but which quickly saturate with incoming deuterium particles and act as a recycling source with R~1. He glow discharge cleaning (GDC) is performed between deuterium discharges by inserting probes that provide a repelling positive voltage to drive the an ionized He background gas into the grounded vessel walls, collisionally de-trapping entrained deuterium neutrals. GDC, however, can only remove a certain fraction of the absorbed particles, and surfaces quickly re-saturate, returning to their high-recycling state.

It has been previously documented on NSTX [30] that the plasma electron density increases with time in small-ELM or ELM-free discharges. This phenomenon is referred to as the secular density rise, and is primarily attributed to a particle source from a recycling divertor, as well as through impurity accumulation (see Section 3.4.1). This density rise is incompatible with future NSTX research goals, which include the desire to operate at the lower edge densities and higher temperature (and therefore reduced collisionalities) necessary for non-inductive current drive [31]. Non-inductive current drive would be a substantial step forward in continuous operation, as it would obviate the need for an ohmic coil.

3.3 NSTX experiments with lithium wall coatings

The concerns for H-mode operation listed above motivated the study of methods to control ELMs, and to reduce the wall and divertor recycling sources responsible for the secular density rise. Previous lithium conditioning results on both TFTR [32] and CDX-U [33] had demonstrated decreases in both edge density and recycling. Thus, a research program was undertaken in the NSTX machine to utilize lithium in an effort to discover a regime more suitable for stable, fully non-inductive operation.

3.3.1 Pellet injection

In 2005, NSTX performed a series of experiments utilizing a lithium pellet injector [34]. Pellets of approximately 2 mg were injected into several classes of discharges after several shots of He glow discharge cleaning (GDC). In a series of center-stack limited L-mode discharges, 30 mg of pellets were injected into helium plasmas in order to coat the center stack. Relative to the reference discharges after similar cleaning procedures, it was observed that there was a 33% decrease in plasma density, with the density rise attributable to the neutral beam fueling rate rather than wall recycling sources. A density reduction of approximately 50% was observed in lower single null (LSN) neutral beam heated discharges [34].

In both classes of discharge, this density reduction was evident on the first shot after the lithium conditioning, but was no longer present by the third discharge following deposition. Although this procedure was effective at producing reduced density, it required the use of several conditioning discharges with helium as the working gas. These conditioning shots would therefore detract from the duty cycle of a power plant. This issue motivated further research into lithium wall conditioning method. Due to the short-lived nature of the lithium coatings, it was evident that a lithium deposition system that could replenish these coatings on a shorter time-scale between discharges was necessary. A lithium evaporation system was thus developed.

3.3.2 Lithium evaporation

Starting in 2005 and continuing to the present day, a LIThium EvaporatoR system (LITER) has been used to deposit lithium coatings on the lower PFCs of NSTX [34]. The initial years of experiments utilized a LITER whose orientation was dictated by a port originally used for inserting a glow discharge cleaning (GDC) probe into the plasma chamber. This aimed the lithium vapor at the center stack of the vessel, preferentially coating it rather than the lower divertor. In the interest of producing thicker lithium coatings on the lower divertor for use in controlling the particle source in LSN discharges, the LITER was re-

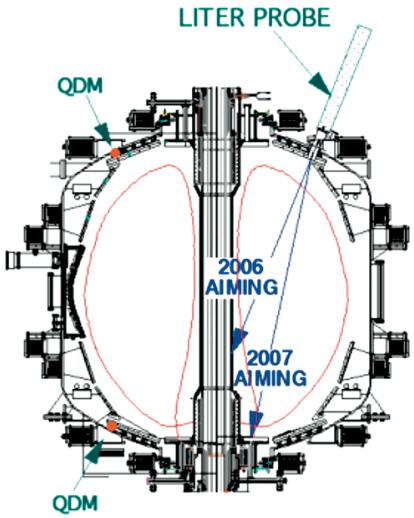

Figure 3.2: LITER aiming in 2006, and 2007 (continuing to present) [5]

designed with output nozzles that re-directed the lithium for the 2007 run campaign, as seen in Figure 3.2.

The results from 2006 on pre-conditioned graphite surfaces [5] in L-mode discharges successfully duplicated those of pellet injection from 2005, but in these cases also the density returned to the pre-conditioning level by the second discharge following application. In situations where helium GDC was not applied prior to a small evaporation, no effect was observed. If, however, sufficiently thick coatings of lithium were deposited (400 - 600 mg of deposition), H-mode discharges showed improvements in stored energy and discharge pumping consistent with previous lithium results utilizing pellet injection. Although these benefits only persisted for a single discharge, the elimination of the need for He GDC allowed for a shorter shot cycle with only lithium conditioning occurring between discharges. Experimental results from 2007 also demonstrated a decrease in ELM frequency relative to similar discharges without lithium deposition.

Despite these initial successes, the lower vessel coverage was only partial, as evidenced by a center-stack 'shadow' where lithium accumulation was greatly reduced. As a result, NSTX continued to expand its lithium operations in 2008 with the installation of a second LITER, offering more complete toroidal coverage of the device. During the 2008

run campaign experiments were run to specifically study the effects of lithium on ELM suppression [35]. In this experiment, increasing lithium deposition was associated with decreasing ELM frequency. In several discharges, ELMs were completely suppressed, correlated with higher temperatures and lower densities as measured by a mid-plane Thomson scattering system [36], as well as higher stored energies. These effects are attributed to the reduction and inwards shift of edge gradients, primarily due to changes in the edge density gradient due to lithium pumping [37]. In those discharges with complete ELM suppression, however, secular rises in both the density and radiated power were observed.

Further LITER experiments during the 2009 run campaign, discussed below in Section 3.4.1, sought to understand and mitigate the effects observed in the ELM-suppressed lithium discharges. An effort was also made to determine divertor and mid-plane heat-flux scale lengths and values under lithiated PFC conditions [38].

3.3.3 Li powder

During the 2009 run campaign, a device for dropping lithium powder by means driven piezo-electric oscillator was used to introduce aerosol Li particles into NSTX discharges [39]. ELM suppression results similar to those achieved with lithium evaporation were achieved, and the characteristic rise in impurities and radiated power was mitigated compared to discharges with evaporated coatings.

3.4 ELM control and consequences

One of the major results of lithium experiments on NSTX has been the reduction and elimination of ELMs, but the consequences include secular rises in electron and impurity density, as well as in radiated power. The suppression of ELMs has also been achieved on the DIII-D device by utilizing a combination of cryopumping and neutral beam injection counter to the plasma current [40]. This regime, the quiescent H-mode (QH-mode), is able

to avoid the secular density rise observed in NSTX through both the use of cryopumping and by the emergence of an edge harmonic oscillation (EHO). The EHO is characterized by correlated magnetic and density fluctuations that promote particle but not energy transport, resulting in the high energy confinement times associated with lithium in NSTX, but without the corresponding deleterious effects. Unfortunately, such a regime has not been reproduced on NSTX to date, and several undesirable effects of lithium conditioning have been observed.

3.4.1 Impurity build-up and radiated power

In ELM-free H-modes obtained through lithium conditioning, energy confinement time can be greatly increased, but this generally corresponds to an increase in particle confinement time. If recycling is also lowered, however, the density source responsible for the secular rise is potentially related to the increased confinement of impurities One of the key questions recent NSTX research has sought to address is whether the increase in electron density is derived from an increase in main-species deuterium ions, or from an increase in carbon or other impurity species concentrations.

One method of assessing the relative purity of a fusion plasma is by measuring the Z_{eff}, or effective charge of the plasma ions. If the plasma were purely deuterium, the effective charge would be +1(e). Any larger measure would indicate the presence of impurity species, which would contribute more net positive charge if more than singly ionized. The core ion temperatures in the > 1 keV range are sufficient to fully ionize carbon, providing a +6 charge. Carbon is generally the dominant impurity due to its prolific use as an NSTX PFC, but other frequent impurities include Fe, O, N, B, Ar, and Cu, all of which are present in either the NSTX PFCs or as residual gases in the vacuum, and are capable of being more than singly ionized at core plasma temperatures. The Z_{eff} in NSTX is typically measured with a visible bremsstrahlung diagnostic [41], and carbon impurity concentration can be determined from the NSTX charge exchange recombination spectroscopy (CHERS) system

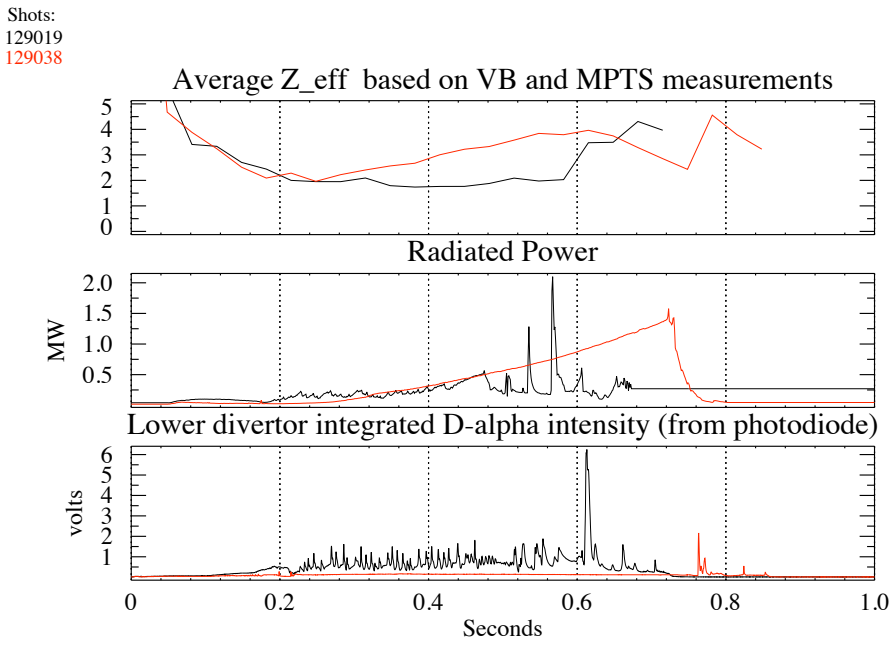

Figure 3.3: Radiated power, Z_{eff}, and $D_\alpha$data from ELMing, non-Li discharge 129019 compared with ELM-free Li discharge 12938

[42]. Deuterium density is often inferred by taking the total electron density from Thomson scattering and subtracting 6x the carbon density as measured by CHERS, treating all other impurities as trace. The core concentrations of these other impurities are often measured spectroscopically through the SPRED [43], XEUS [44], and LoWEUS [45] systems. These other systems do not provide absolute measurements, but only relative comparisons. Impurity concentrations (and spatial locations) can also be determined by using visible cameras employing different wavelength filters, discussed in more detail in Section 3.5.5. Lastly, radiated power can be determined by use of bolometry systems. NSTX employs both core [46] and divertor bolometry diagnostics for this purpose.

Radiated power, Z_{eff}, and D_α data from the canonical discharges compared for ELM suppression in NSTX, 129019 (no Li with ELMs) and 129038 (Li evaporation without ELMs), are presented in Figure 3.3. In the ELMing shot, the ELM events serve to limit

the buildup of impurities and reduce the overall radiated power, while no such relief mechanism exists in the ELM-free discharge. Power balance dictates that an ever increasing fraction of the input power is diverted to radiation as impurity content increases, which while inherently undesirable due to decreased heating efficiency, can also lead to radiative collapse if the plasma is no longer being adequately heated. Just as much of scientific advancement occurs as serendipitous accidents, so too did an alternate potential means of suppressing ELMs turn into a method for triggering them and a path to impurity control.

3.4.2 Resonant magnetic perturbation experiments

It has been previously demonstrated on the DIII-D tokamak that certain categories of ELMs could be suppressed through the use of resonant magnetic perturbations (RMPs) [47]. These perturbations are achieved by the use of auxiliary magnetic coils that provide an n = 3 toroidal mode number field which resonates with various magnetic islands in the plasma edge. This creates ergodized flux surfaces that change the position of the peak pressure gradient, similarly to what occurs when lithium is applied in NSTX. In an effort to duplicate this effect and pursue an alternate means of ELM suppression in NSTX, the existing coils used for resistive wall mode (RWM) stabilization [48, 49] were utilized to try to create a similarly resonant field structure.

Due to the fact that these coils were not initially designed for RMP usage, ELM-suppression did not occur - indeed the opposite phenomenon, ELM triggering, was observed [50]. The coils create both strong resonant and non-resonant fields, which serve to brake the plasma rotation through an increase in neoclassical toroidal viscosity, as well as to alter the plasma pressure (and potentially current) profiles in mechanisms which are not yet fully understood. The net effect, however, is to move into a region unstable to the peeling-ballooning modes traditionally associated with ELM triggering. Additionally, the ability to reliably trigger ELMs is shown [50] to decrease the stored energy lost per ELM event. This serves to mitigate the heat flux to the PFCs and has potential applications

for ITER, in which the power is high enough to cause considerable damage to the walls. Once this result was observed, it was tested to determine if it could be a viable means of controlling impurity accumulation in NSTX discharges.

As shown in [50], ELMs triggered in discharges where lithium coatings had been applied served to reduce the radiated power and Z_{eff} relative to discharges with no ELM triggering. The secular density rise is also somewhat arrested relative to the lithium-only case, but is not completely eliminated. The effects on the total stored energy during the quiescent period between ELMs are minimal. However, the author does note that ELMs triggered in this manner during lithium-conditioned discharges can release substantial fractions of the stored energy per ELM. This is an effect which can possibly be mitigated by the triggering of more frequent and smaller ELMs. Possible further applications of this technique in concert with lithium coatings remain an area of active research.

3.5 The liquid lithium divertor

As noted in the above sections, one of the primary disadvantages of LITER operation is the need to continually apply coatings between discharges. This requires the evaporator systems to be periodically refilled, an event that is disruptive to the operational cycle of the machine. When a LITER needs to be refilled, it must be retracted into its housing, which is then sealed from the main vacuum by means of a gate valve. The LITER is then re-loaded by means of a liquid-fill system using heated lithium under an argon atmosphere. Once the LITER is reinstalled, the housing must be put back under high-vacuum. Finally, the LITER is de-gassed at a temperature slightly above the melting point of lithium to remove trapped impurities that may have entered the device during filling. This process can take over 18 hours, and while often performed over-night or on a weekend, can cut into the operational schedule - especially if a mid-week refilling is necessary. The typical load in a LITER is 90 g of lithium, which under typical application conditions will last for roughly 1.5 weeks.

Frequent LITER use also leads to the deposition of large amounts of lithium into NSTX, which can lead to inadvertent coatings of vacuum windows and large buildups of passivated lithium on the tile surfaces themselves.

The results described in the following section led to the concept of building a liquid lithium divertor, i.e., a macroscopic layer of liquid lithium on a non-carbon substrate, and placing it in NSTX. The goal was to control the strongest recycling source in the machine, and avoid the pitfalls associated with traditional evaporated lithium and bare PFC H-mode regimes. A complementary reference to this section can be found in [6], which outlines many of the LLD design requirements and considerations.

3.5.1 A brief history of liquid lithium in deuterium plasma devices

Investigations into the ability of lithium to trap hydrogenic species have been undertaken since the 1960s, when experiments were conducted with energetic ion beams on both solid and liquid lithium substrates [51]. This concept, however, was not seriously explored in reactor relevant regimes until the development of a liquid lithium capillary porous system (CPS) in the 1990s [52]. The effects of this system were investigated in the T11-M [53] and FTU [54] tokamak devices, showing evidence of deuterium pumping by the liquid lithium surface. Experiments on the PISCES-B machine showed promising results for the hydrogenic retention properties of liquid lithium as opposed to the solid form [55]. This result demonstrated the ability of a thick liquid lithium film to absorb deuterium at a 1:1 atomic ratio, forming LiD molecules and sequestering rather than recycling incident lithium. Due to the mobility of these molecules in the thick liquid, the surface did not saturate at the lower ratio observed in the solid lithium case. Theoretical and simulation results characterizing a wide array of recycling regimes [56] highlighted the potentially dramatic changes in plasma temperature and density possible when recycling was sufficiently reduced.

Experimental results from the Current Drive eXperiment-Upgrade (CDX-U), also at PPPL [57], showed the favorable operating conditions possible in a tokamak environment

when using a liquid lithium tray (with a clean lithium surface). These results provide the most relevant empirical basis for the NSTX LLD concept, as they demonstrate the density reduction and increases in energy confinement time associated with a macroscopically thick liquid lithium PFC. As the liquid lithium tray was designed, constructed, and operated in CDX-U, it provided much of the technological knowledge necessary to construct the system for LLD implementation, mainly the interaction of lithium with material surfaces and residual gases in a plasma vacuum environment. In addition, the CDX-U result motivated the construction of the Lithium Tokamak eXperiment (LTX), a small ST with fully-liquid-lithium-coated walls and which is in the startup process at the time of this writing.

3.5.2 Desired operating regime and fill method

3.5.2.1 LLD Placement

Although the highest performing NSTX discharges (in terms of duration and stability) are generally run on the inboard divertor, many factors were taken into consideration during the LLD design process. Figure 3.4 summarizes some of the issues considered in LLD placement. A 0D particle balance model was developed by R. Maingi [58] to evaluate several pumping scenarios and to determine the relative plasma density response for two different discharge shapes based on LLD size and location.

The high-δ (triangularity) shape, shown in Figure 3.5a, represents the high-performance class of discharge typically run with the outer strike point on the inner section of the NSTX inner divertor. This represents a discharge that would be run on the inner section of the inboard divertor. The medium-δ shape, Figure 3.5b, represents a compromise discharge that would be run with the strike point on the outer section of the inner divertor. The final shape utilized in testing was the low-δ shape, a lower performing discharge run on the outboard divertor and shown in Figure 3.5c. Placing the LLD to take best advantage of this shape represents the lowest programmatic risk, as any failure of the LLD that prevented plasma flux from being placed on it (e.g., significant surface erosion or impurity flux into

RADIUS & WIDTH	GENERAL MERITS	GENERAL DEMERITS	PARTICLE BALANCE & RECYCLING	EROSION & DEPOSITION	DIAGNOSTIC ISSUES re Radius & Width
Inner-half, Lower Inner Divertor	+ Lowest R/a + Allows high performance NSTX plasmas + Graphite outboard for other XPs + Smallest circumference (7')	- Biggest impact if malfunction during run. - Difficult to reach Inner Vessel feedthrus. - Lower Inner Divertor gas ports. - ~137cm Li feed stroke from HorizDiv Port. - Possible CHI issues	Modeling in progress	-Shortest CS sputtering trajectory - highest Li_2C_2 formation?	- Loss of 1 or 2 Bz coils - Loss of 2 TC - Loss of 2 LP
Outer-half, Lower Inner Divertor	+ Graphite on inboard side for other XPs	- Difficult access to Inner Vessel feedthrus. - Lower Divertor gas ports. - ~117cm Li feed stroke. - Possible CHI issues	Modeling in progress		-Loss of 1 or 2 Bz coil - Loss of 2 TC - Loss of 2 LP spaces
Inner-half, Lower Outer Divertor	+ Minimal impact if malfunctions during run + Allows majority of XPs to use Inner Divertor + Nearby large ports + Minimal feedthru issues + No apparent CHI issues + Higher R/a, NHTX-like XPs + Allows characterization of heat flux footprint for higher-aspect-ratio NHTX plasmas	- Largest circumference (15.5') - Sloping installation on conical section more difficult. - Flat installation on conical section - Unusable for present smaller R/a high performance plasmas. ~~102 cm Li feed stroke from HorizDiv Port	Modeling in progress		-Loss of 2 Bz coils - Loss of 2 TC - Loss of 1 LP - FL response changes?

PPPL

Figure 3.4: LLD design considerations matrix

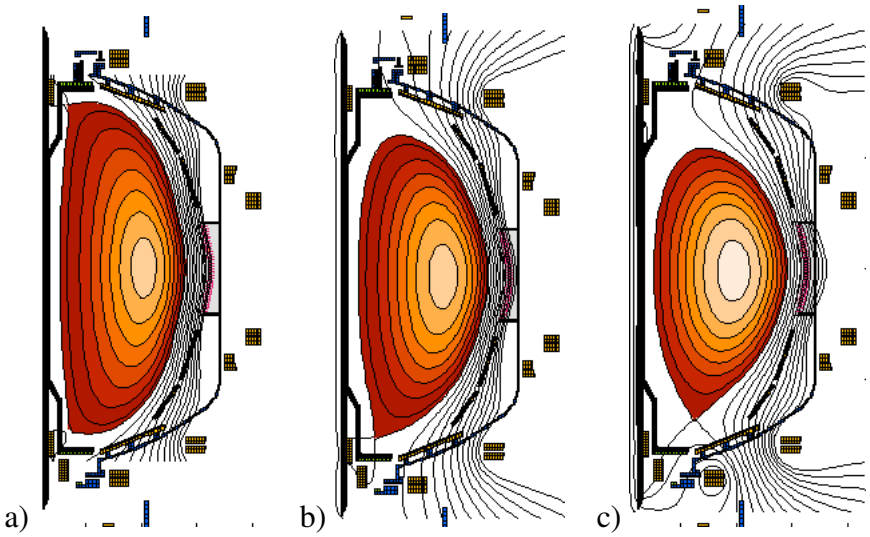

Figure 3.5: Cross sections of a) high triangularity, b) medium triangularity and c) low triangularity discharges used for LLD placement studies

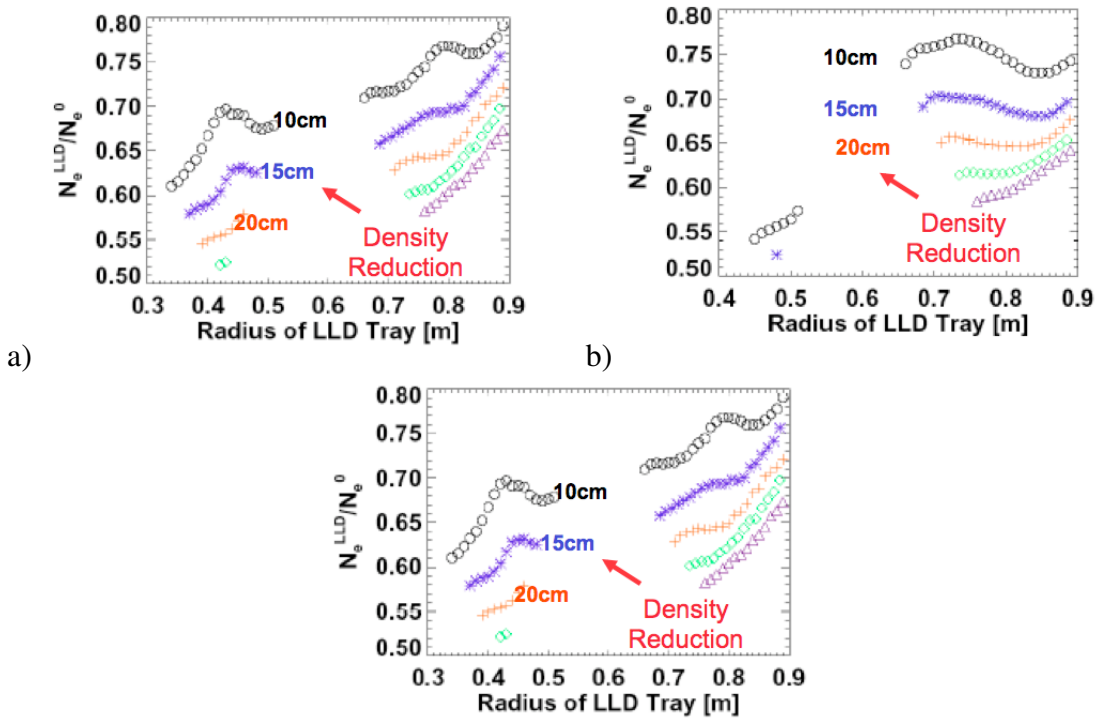

Figure 3.6: 0D pumping model for a) high-δ, b) medium-δ, and c) low-δ discharge shapes

the plasma when irradiated) would still allow high-performance discharges to be run on the inboard divertor.

The primary input to the 0-D particle balance model is the radial profile of the divertor D_α light as measured by a 1D-CCD camera [59]. This is then coupled with the assumed recycling coefficients for various surfaces: 0.98 for carbon tiles vs. 0.15 for the LLD. As there are many other assumptions about the relative magnitudes of plasma fluxes and fueling efficiencies that are required (inboard/outboard and top/down asymmetries, interpretation of recycled deuterium emission, neutral beam and gas fueling efficiency), the model was primarily utilized to give relative density scenarios for different LLD placement locations and widths rather than absolute density predictions. The results of applying this model to the high-δ, medium-δ, and low-δ cases can be seen in Figure 3.6. The y-axis shows the density relative to a discharge without the LLD present, which is plotted against the radial position of the LLD as well as the width of the lithium tray itself. As expected,

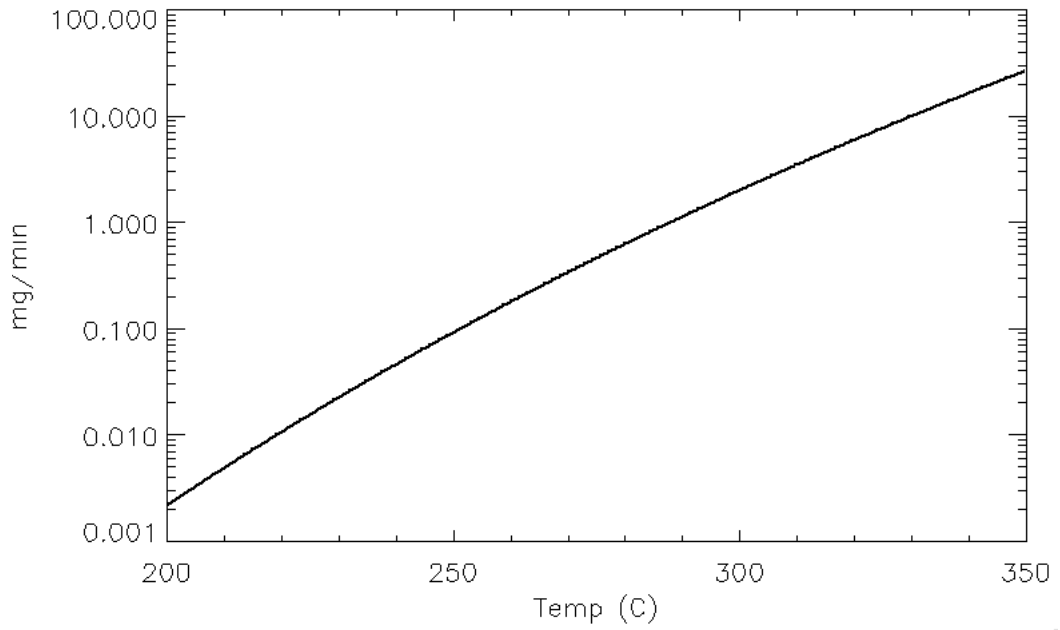

Figure 3.7: Lithium flux off LLD vs. temperature

wider trays produce greater density reductions, and since a significant fraction of the flux is always reaching the inner divertor, trays located farther inboard produce the greatest density reductions regardless of outer strike point location. It was ultimately decided that a 20 cm tray located just inboard of the CHI gap would provide the least programmatic risk, easiest feed-through access, and sufficient pumping capabilities.

3.5.2.2 Operating temperature

The minimum operating temperature for the LLD to qualify as liquid is approximately 180° C, the melting point of lithium. Beyond this, the operating point is primarily set by the capabilities of the heating system and the desire to keep evaporation to a minimum. Figure 3.7 shows the theoretical maximum for evaporative flux from the 4 LLD plates vs. their operating temperature. Since LITER typically deposits 20-40 mg/minute, the lithium flux off the LLD would approach this value between 300 and 350° C. This would not only make LLD fueling difficult at this temperature, but would begin to coat the entire vacuum

vessel with lithium. This would possibly be desirable for certain experiments, but could lead to many undesirable consequences for routine operation, such as the development of coatings on diagnostic windows or changing the global wall conditions and hindering attempts at comparison across discharges. There exists the possibility that at sufficiently high temperatures, the lithium density would overwhelm the plasma density, but given that one mole of lithium is 7 g, the threshold temperature for this occurrence exceeds the negative fueling balance temperature states above. Thus, the operating temperature for the LLD should be 180 to 350° C.

3.5.2.3 Fill system

CDX-U was able to fill its tray limiter by utilizing a liquid fill system developed jointly with the PISCES group at UCSD [60], but access was made easier by virtue of the relatively small size of the device and the ability to locate lithium reservoirs on top of straight feed tubes. The schedule of LLD development and installation did not permit the creation of an analogous system on NSTX. Several alternative systems were considered, including solid fill, but were ultimately deemed to be unfeasible for various reasons (see Section 3.5.3). This left the LITER probes as the only viable near-term LLD fill system. As described in Section 3.3.2, the LITER probes are now aimed at the lower inboard divertor, as this is where most of the high-performance lower single null discharges are run, and where the greatest benefit is often realized. The placement of the LLD rendered this filling technique inefficient, as only 4.5-7% of evaporated lithium actually ends up on the LLD surface. Figure 5 in [6], reproduced here as Figure 3.8 , shows a plot of the deposition from the LITER probes and the relative thicknesses deposited on various parts of NSTX. Calculations in this paper also show that if a 10% deuterium trapping efficiency is assumed, 7.9 g of lithium deposition in NSTX (taking into account the 7% fill efficiency) is necessary to place the requisite number of lithium atoms on the LLD to absorb the $4.8x10^{21}$ deuterium atoms input as fuel gas into a typical NSTX discharge. This results in much larger amounts

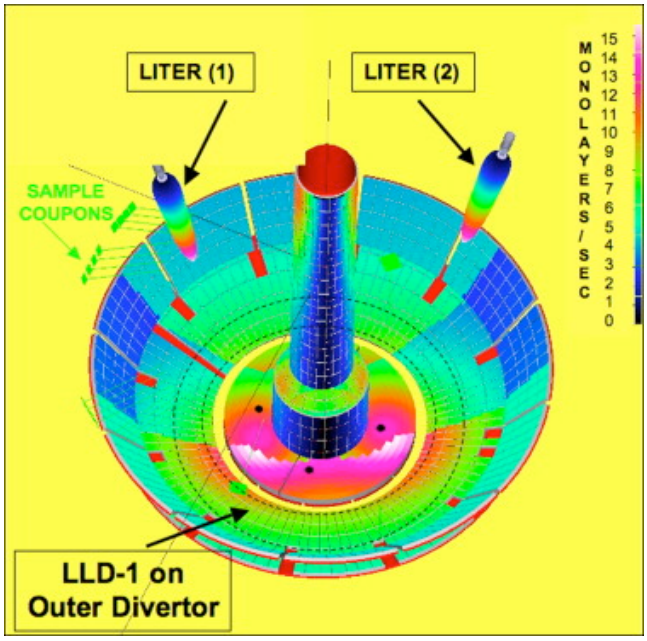

Figure 3.8: Deposition of LITER probes on LLD, taken from [6]

of lithium in the machine than normal, which typically operates with 100-200 mg of lithium evaporated on PFCs prior to a discharge.

3.5.3 Offline testing

This section deals with various tests and procedures that were developed largely at PPPL. Though they do not relate directly to many of the physics results that were obtained with the LLD, they were performed as part of its design thesis research and are therefore included.

3.5.3.1 Fill and cleaning

In order to determine the optimal substrate surface for the LLD, a series of experiments was conducted. Figure 3.9 shows a successful test of lithium wetting on a flame-sprayed (atop a stainless steel (SS) substrate) porous molybdenum surface. The details of this surface are described in the following section. The porous molybdenum (Mo) surface was also studied to determine lithium wetting effectiveness and potential cleaning methods.

After it was determined that the sample would wet, an experiment was performed to

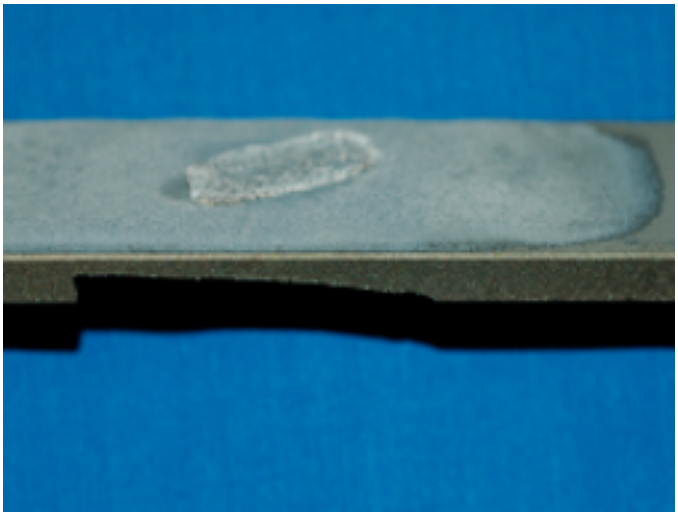

Figure 3.9: Lithium successfully wetting a porous molybdenum surface

glean whether the lithium would migrate up the 22° angle of the divertor. To accomplish this, a LITER probe was placed in an evacuated $(1x10^{-7}Torr)$ test chamber with a heated target consisting of Mo on SS substrate facing its 'snout', as seen in Figure 3.10. A shutter was used to block 50% of the incident Li flux, providing a line of sight to only the bottom half of the substrate. The depositions were performed with the sample heated to between 200 and 250° C (as measured by a thermocouple mounted beneath the sample), well above the ~180° C melting point of lithium. The next image, Figure 3.11, shows the area of greatest deposition and a gradient in lithium thickness as it diffuses throughout the sample. The sequence continues in Figure 3.12, which shows a top-down view of the sample, which is full of lithium. This is indicated by the pooling of the lithium on the surface, forming blobs due to its high surface tension. Note that the lithium is also restrained by this surface tension from flowing down the incline and over the side of the sample, a favorable indication for lithium retention in the final design. The sample was then cooled and allowed to passivate by reacting with the residual gas pressure in the chamber. The result is seen in Figure 3.13, and the surface color change is caused by the formation of LiOH as the lithium reacts with residual water. The last image in the series, shown in Figure 3.14, was obtained after the sample was re-heated to 400° C, causing a breakup and melting of the

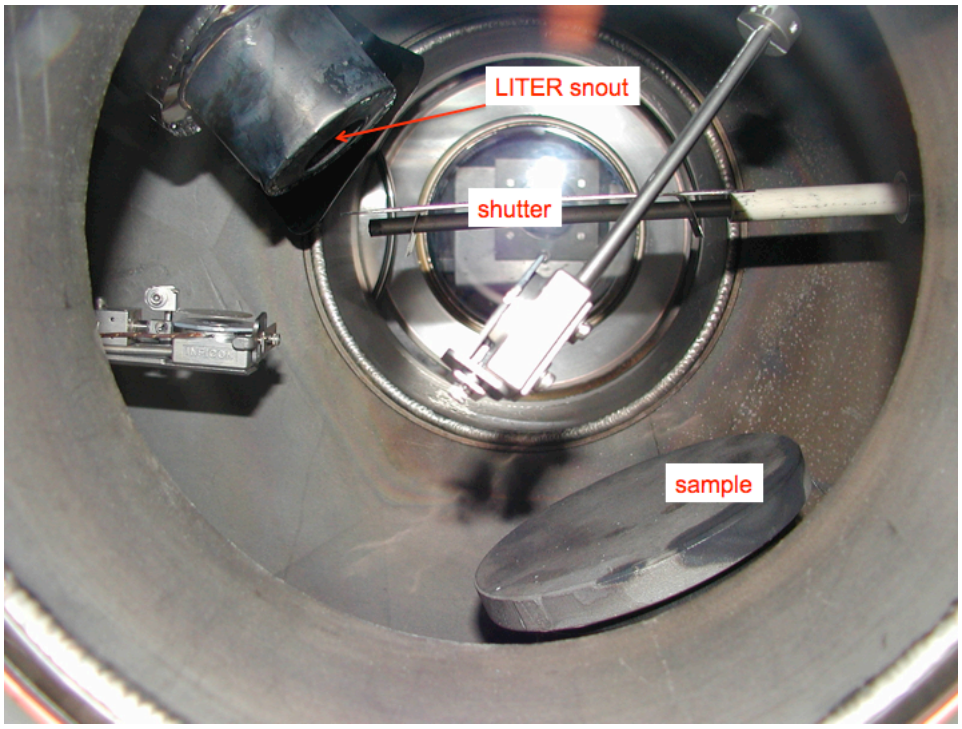

Figure 3.10: Chamber for Li wetting experiments

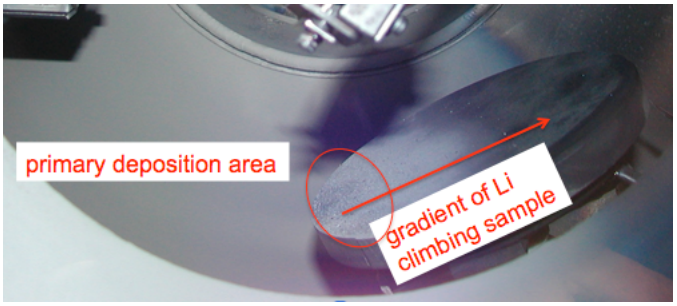

Figure 3.11: Primary deposition area and lithium spreading in test chamber

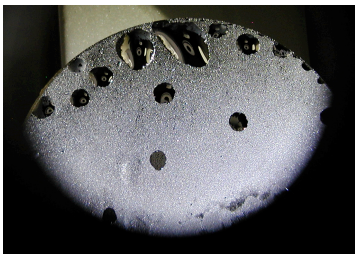

Figure 3.12: Overfull substrate with visible blobs

Figure 3.13: Passivated sample after LITER evaporation

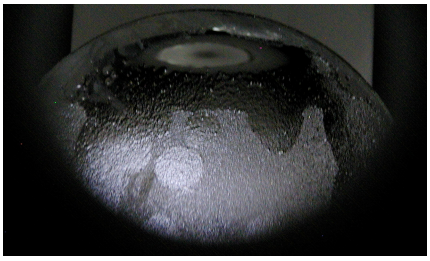

Figure 3.14: Sample after being reheated to 400° C

surface layer of lithium compounds (e.g., LiOH) and a return to a liquid state. Since the melting point of LiOH is 462° C, the lowest for all of the lithium compounds, this possibly indicates a discrepancy between the actual and measured temperatures. This heating also caused a reduction in surface tension that allowed the lithium to flow to the bottom of the sample and collect in the pool visible in the image. Despite this, the lithium still did not flow over the side of the sample, potentially due to the lower edge temperature.

Following these tests, another set of experiments was conducted to determine if a solid-fill system would be a viable alternative to evaporation, given the relative inefficiency of LITER delivery. Although heating the sample seemed to successfully break up surface impurities, it would be undesirable to heat the LLD to the $\geq 450°$ C temperatures necessary to achieve this, given the high evaporation rates discussed in the section above and the possible implications for fueling of the LLD and coating of the diagnostic windows. GDC was investigated as a potential cleaning method since the bluish hue observed in the later pictures above was potentially due to surface oxides that could be removed by this method, as well as the fact that GDC could potentially break up the hydroxides at lower temperatures. A similar setup to the experiment described above was utilized with a solid loading system

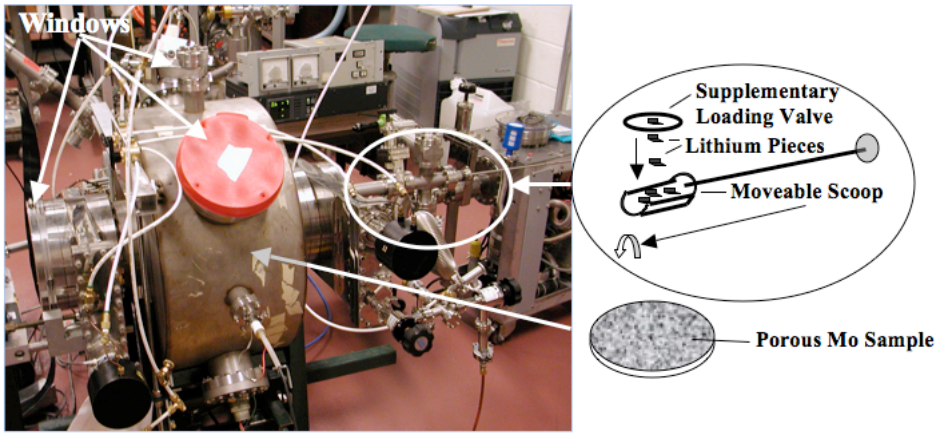

Figure 3.15: Exterior view of solid loading test chamber. Lithium pieces are loaded into the scoop, which is then rotated via a Wilson seal to deposit them on the sample.

was attached (seen in Figure 3.15), and the sample was outfitted with biasing capability to allow for GDC.

The first cleaning step performed was to run a hydrogen glow for approximately one hour on the sample (biased negatively at -1500 V for ion impact). The aim was to chemically sputter molybdenum oxides to form water with the incident hydrogen molecules. A trace of the RGA partial pressure of water before and after the glow is seen in Figure 3.16 . The trace indicates that after the glow was complete, the water partial pressure was higher than before the glow application. As the RGA was our only quantitative measure during this test, there is no direct evidence that the resultant water resulted from oxide sputtering. At the very least it helped to decrease the overall water pressure in the chamber, as seen at the far right of the graph. This procedure was repeated several times before lithium loading began.

The scoop shown in the sketch in Figure 3.15 was used to drop 10-15 grams of solid lithium chunks from a height of approximately 2 in (to simulate possible dropping in NSTX) onto the substrate, which was heated to 246° C to achieve melting. The sequence begins in Figure 3.17, which shows the freshly dropped lithium chunks on the substrate. Several bench tests were performed to determine the optimum chunk shape for retention on the sample surface. The greatest success was obtained by simply bending the lithium

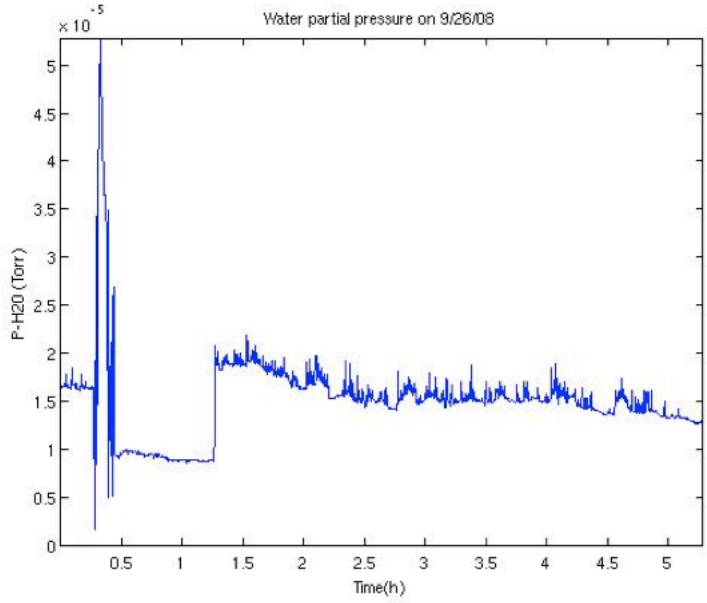

Figure 3.16: Water partial pressure before and after hydrogen glow on bare sample. The depressed pressure region is the time of glow

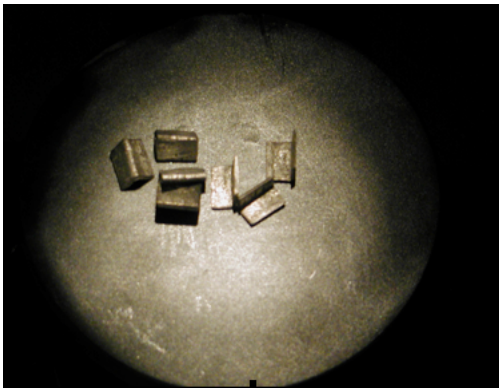

Figure 3.17: Solid lithium chunks deposited on heated substrate

Figure 3.18: Solid loading test, 30 minutes after deposition and at 280° C

Figure 3.19: Li substrate following reheating and cold glow tests

sheets in half into a tent shape, and this design was adopted. After 30 minutes, and after raising the temperature slightly to 280° C, the lithium has diffused throughout the sample, although some solid remnants of the chunks still remain, as seen in Figure3.18 . These solid husks are believed to be hydroxides formed on the outer surfaces on the chunks once they began to heat, and increase their reaction rate with the residual vacuum gases. Following the taking of the above picture, an additional chunk of lithium was added, a reheating test was performed (with similar results as above), and hydrogen GDC at room temperature was conducted on the sample for one hour. The resulting image (at room temperature) is shown in Figure 3.19. The striations occurred as a result of the reheating test, and the room temperature GDC did succeed in breaking up some of the hydroxide crust. The real suc-

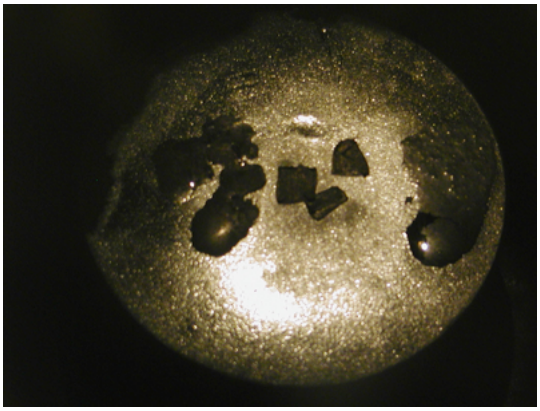

Figure 3.20: Sample at temperature after hot glow performed

cess of these tests, though, was when the sample was heated to 228° C and the glow was performed for an hour, the result of which is shown in Figure 3.20. The surface exhibits the shininess characteristic of clean liquid lithium, and the coating is uniformly covering the sample. The chunk husks are still present, but some have merged into liquid blobs rather than remaining solid on the surface. One explanation for why some samples are more liquid than others, consistent with the assessment of hydroxide crust formation, is that those that melted first absorbed a higher degree of residual gas and, thus had present much higher levels of impurities that would inhibit subsequent re-melting.

3.5.3.2 Active lithium signature

Aside from cleaning and fill techniques, experiments were undertaken at PPPL to determine if a signature for an active lithium surface could be found. An active surface was tentatively defined as one that could achieve some fraction of an anticipated 1:1 uptake of deuterium as demonstrated in the PISCES-B experiment [55]. Tests performed at PPPL were limited to measuring residual gas pressures during various heating and glow discharge experiments, but no concrete metric other than a decrease in water partial pressure was found. RGA deconvolution software developed by our experimental group was utilized to express a mass spectrum as component molecules during various stages of an experiment with evaporated lithium coatings on a porous molybdenum substrate. The results are shown in Figure 3.21.

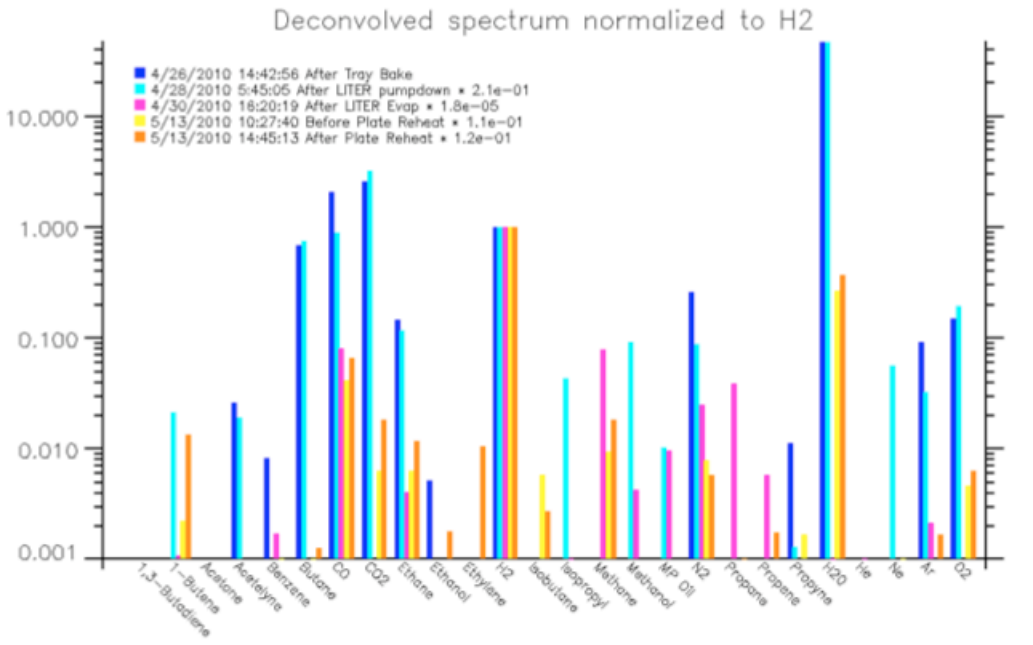

Figure 3.21: De-convolved RGA spectrum from laboratory experiments

The 4/26 and 4/28 data represent points before the evaporation of lithium, the 4/30 line is immediately following evaporation, and the last two 5/13 data points are after passivation and reheating, respectively. As stated above, the water peak disappears after fresh lithium evaporation, but no other concrete signature than the presence of methane and other hydrocarbons was found. The inability to resolve the mass 28 peak between nitrogen potentially introduced by LITER and newly formed hydrocarbons also increased the difficulty of interpretation. There is also no clear evidence on the RGA of re-activation after reheating, with little salient difference between the two final data points. In addition, the presence of deuterium in NSTX plasmas and variations in vacuum conditions during operation precludes the use of this technique as a reliable real-time measure of surface activity.

More advanced testing was conducted at Purdue with both porous molybdenum (unpublished) and graphite substrate [20] samples to determine the surface chemistry effects. The tests on graphite reveal a complex surface chemistry that is not solely dominated by LiD bonding, but is influenced by the carbon and oxygen present as well. Although molybdenum surfaces would exclude the presence of native carbon, oxygen is still always present

in NSTX, and carbon is available both as a residual gas and as dust sputtered from nearby graphite PFCs. Future in-situ testing is planned to allow for dynamic evaluation of lithium surface evolution, a goal that is necessary to characterize the surface activation in real-time. These tests will utilize the MAPP [61], an in-situ analysis suite that has been installed in NSTX for the 2011 run year. MAPP will employ XPS, ion scattering spectroscopy, and thermal desorption mass spectroscopy to analyze samples of various materials (C, Mo, etc) exposed to the plasma and lithium evaporation without the need to break vacuum.

3.5.3.3 Heater testing

A final series of tests was undertaken at PPPL to evaluate potential heaters for use in the LLD. Watlow cartridge (resistive) heaters were selected and several were purchased for testing purposes. Although resistive heaters specifically developed for vacuum applications do not exist, the Watlow heaters most closely matched the design needs. These heaters were equipped with internal thermocouples to assure that the heater components would not exceed their failure temperature. The heaters were installed in a copper block along with external thermocouples to measure the bulk temperature and mounted in an evacuated chamber. An RGA was used to monitor outgassing from the heaters. Initial testing revealed that large amounts of mass 44 were present as the heaters were first brought up to temperature, but disappeared after a sufficient duration in excess of 500° C, and present in much smaller amounts on subsequent reheats. This was attributed to the presence of organic binding materials involved in the heater manufacturing process. It was also discovered that the heaters would develop an internal short circuit between the power and thermocouple leads after repeated cycles; posthumous examination revealed that this was caused by the formation of internal conduction pathways. A third issue discovered was that the heater internal temperature would often exhibit a rapid rise time before exhibiting a temperature rise proportional to the copper bulk. This was related to the heaters not being in complete thermal contact with the copper due to small discrepancies in the mounting hole and heater

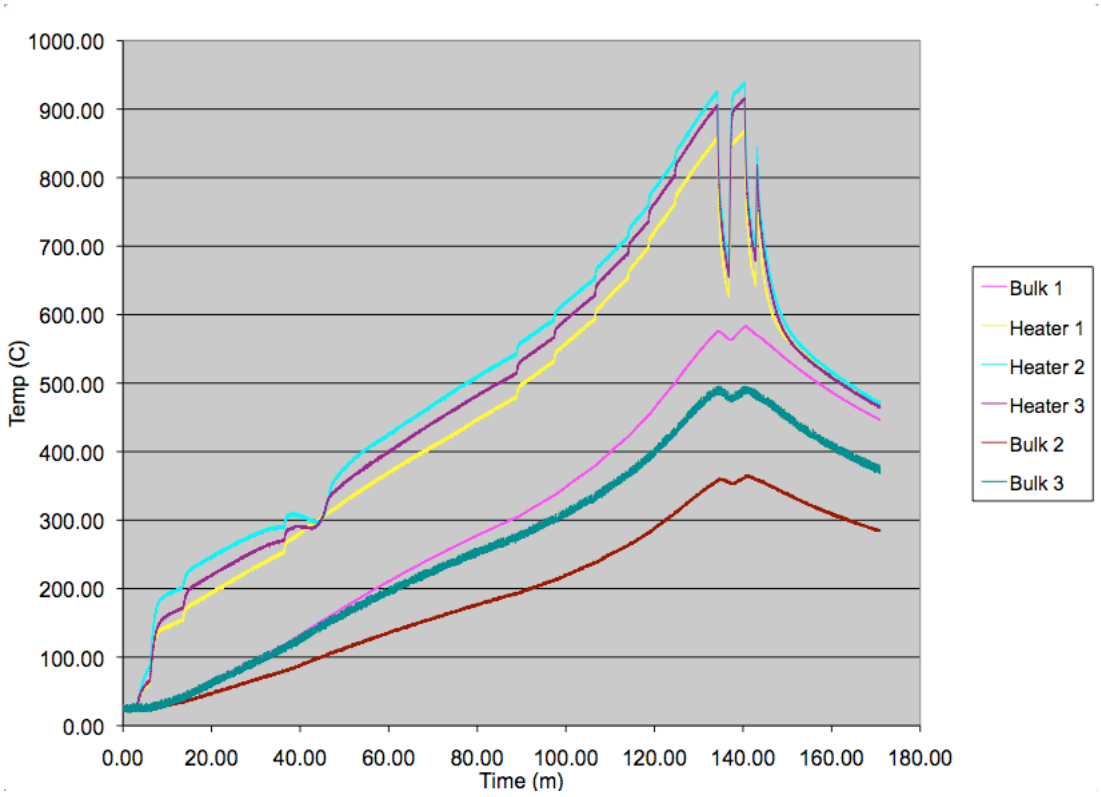

Figure 3.22: Test of candidate LLD heaters

diameter, unavoidable due to machining tolerances. The heaters would rapidly rise in temperature until they had expanded to the point that they were in sufficient thermal contact to begin heating the bulk. Figure 3.22 shows the results of one such heating test.

The results of these experiments led to important changes in the design of the heating system. A vacuum bake to 700° C was conducted on all heaters before installation to reduce organic impurities. As the thermocouples were deemed the root cause of internal short-circuiting, heaters without internal thermocouples were instead used. As seen in Figure 3.22 above, the ΔT between heaters and bulk was approximately 200° C, and with maximum operating temperatures in the 350° C range, the corresponding 550° C internal heater temperature would be well below the 760° C manufacturer-rated failure temperature. The final refinement in heater implementation that resulted from these tests was the use of a spray-able graphite coating to increase heater contact with the bulk material.

3.5.4 LLD plate design and fabrication

Engineering constraints set many of the design parameters for the LLD. As will be discussed in greater detail in Section 4.2.2, the compatibility of liquid lithium with various substrate materials was the initial criterion to consider in construction. In addition, the LLD plates must be capable of maintaining a uniform surface temperature above 180° C. The steady-state heat flux in the NSTX divertor region, which can approach $10 MW/m^2$, also presents a formidable power-handling challenge for any candidate substrate. Lastly, given the fill method of LITER evaporation, the plates should also be able to provide a uniform lithium thickness over their entire area rather than possessing regions locally rich or poor in liquid lithium. This surface must also be resistant to ejection by JxB forces that could arise if currents were induced in the lithium by disruptions, thermo-electric currents, SOL currents, or other transient plasma events, as occurred in the DIII-D DiMES probe [62]. The general details of the LLD design are described in [63], but are expounded upon below.

Copper provides the desired thermal response, but is reactive with liquid lithium. To mitigate this effect, a thin stainless-steel layer (0.01 in) was bonded to the underlying (0.875 in) copper plate. The layer is thick enough to prevent lithium penetration, but thin enough to compensate for the low thermal conductivity of stainless steel. To allow for retention of lithium against JxB force ejection and to provide a means for the liquid lithium to diffuse evenly across the plate surface, a 165 μm layer of 45% porosity flame-sprayed molybdenum was deposited as the final, plasma-facing layer. Molybdenum is a high-Z refractory metal with a high melting point (2623° C), reducing the likelihood that it will sputter or erode and contribute a significant source of plasma impurity. An electron micrograph representative of this porous layer is shown in Figure 3.23 . This substrate surface was originally developed for CDX-U/LTX in cooperation with Plasma Processes International, but was later adapted for used in the LLD.

Lithium itself is also a potential plasma impurity, but simulations show that due to its

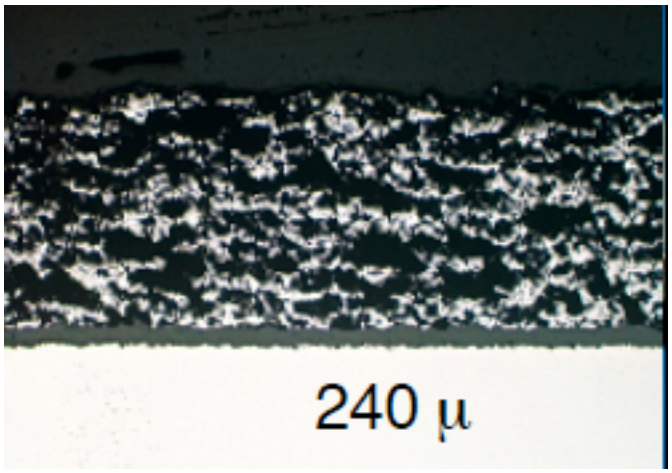

Figure 3.23: Electron micrograph of porous Mo layer

low ionization energy it is readily ionized in the SOL and was not expected to penetrate far into the core plasma [64]. This result is borne out by yet unpublished CHERS results [65], which show core Li fractions below 0.1%. Additionally, to prevent fully toroidal currents from forming in the LLD, it was decided to divide it into 4 plates, each spanning 82.5° toroidally. This also leaves space between the plates for the placement of attendant diagnostics in the gap tiles, discussed in Section 3.5.6 below.

To maintain the liquid lithium surface at temperatures between 180 and 350° C, a heating and cooling system was also installed. The heating system initially consisted of 12 470W cartridge heaters per plate, but was later supplanted with a hot-air heating system utilizing the cooling system pipes. These pipes were initially designed to prevent thermal ratcheting throughout the day as discharges heated the LLD. Each consists of a 0.375 in diameter tube brazed to the underside of each plate, through which room temperature air is flowed. The design of the tubes was based on the capability to return the LLD to its pre-discharge temperature during the 10-minute interval between shots. Although ΔT of each plate could approach 10° C per discharge, no net thermal ratcheting was observed above 220° C. In another example of serendipity, the cooling system pipes proved capable of heating the LLD plates to an excess of 220° C, utilizing heated air when the cartridge heater system eventually failed due to an in-vacuum short-circuit. This facilitated contin-

ued LLD high-temperature operation and was instrumental in allowing the results of this thesis to be obtained. Although extensive heater testing was performed, as described in the section above, this particular failure was attributed to a shorting of the heater leads to each other, linked to an insulation failure along the heater cable run.

The initial fabrication of the plates was completed externally at Sandia Labs (Livermore, CA). A conic section of copper was formed to match the 22° angle of the NSTX outer divertor floor, and was then cut into the four quadrants. The thin stainless layer was then brazed onto the underlying copper and the channels for the cooling tubes and holes for heaters and thermocouples were milled into the plates. Following the machining, the plates were sent to Plasma Processing Incorporated in Huntsville, AL, where the Mo coating was applied. The completed plates were then shipped to PPPL for installation of heaters and thermocouples and eventual placement in the NSTX vacuum vessel. Figure 3.24 shows a schematic of an LLD plate. Another engineering drawing showing a 3D view of the cartridge heaters and air cooling/heating lines is shown in Figure 3.25. Finally, Figure 3.26 shows photographs of both an individual plate and the installed LLD in NSTX immediately preceding the 2010 run campaign.

3.5.5 Associated diagnostics

This section describes diagnostics external to the LLD, while those located in close proximity can be found in the following section. Many of the diagnostics associated with the measurements necessary to quantify the effects of the LLD have been described in the preceding sections in this chapter, including the D_α array, impurity measurement diagnostics, radiation bolometers, CHERS for ion temperature and density, and Thomson scattering for electron density and temperature measurements. In addition, SOL electron density and temperature profiles are augmented by results from a midplane reciprocating Langmuir probe [66], capable of plunging into the plasma and providing SOL radial midplane data.

The ORNL Reflectometer [67] is another diagnostic that had been previously employed

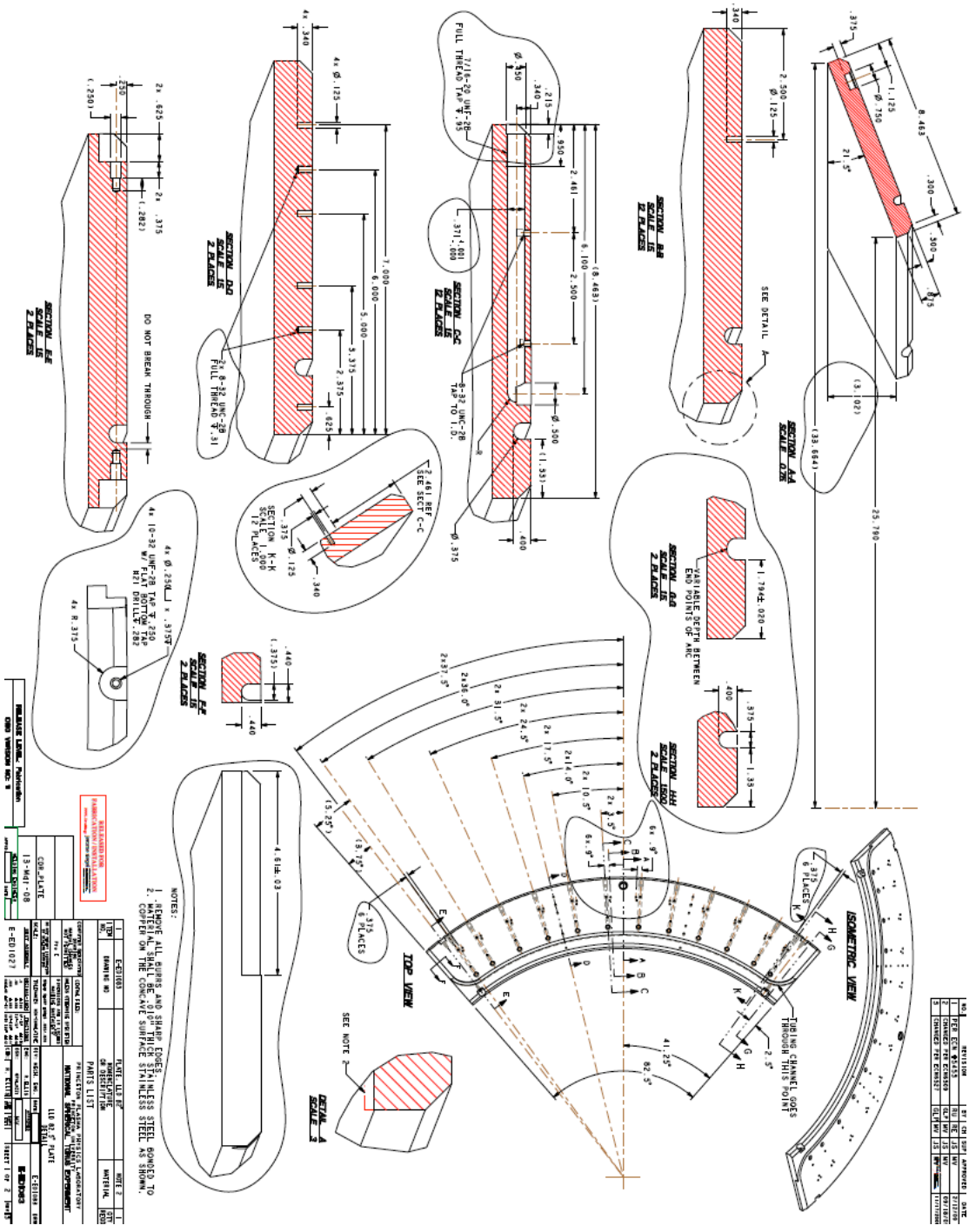

Figure 3.24: Engineering drawing of LLD plate

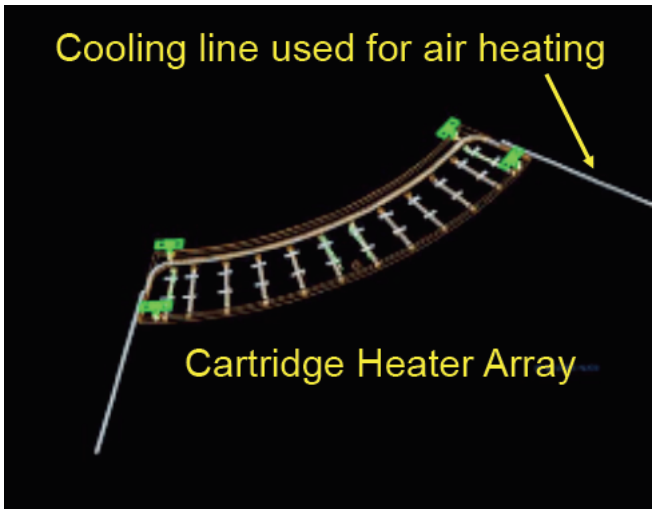

Figure 3.25: View of LLD heating systems

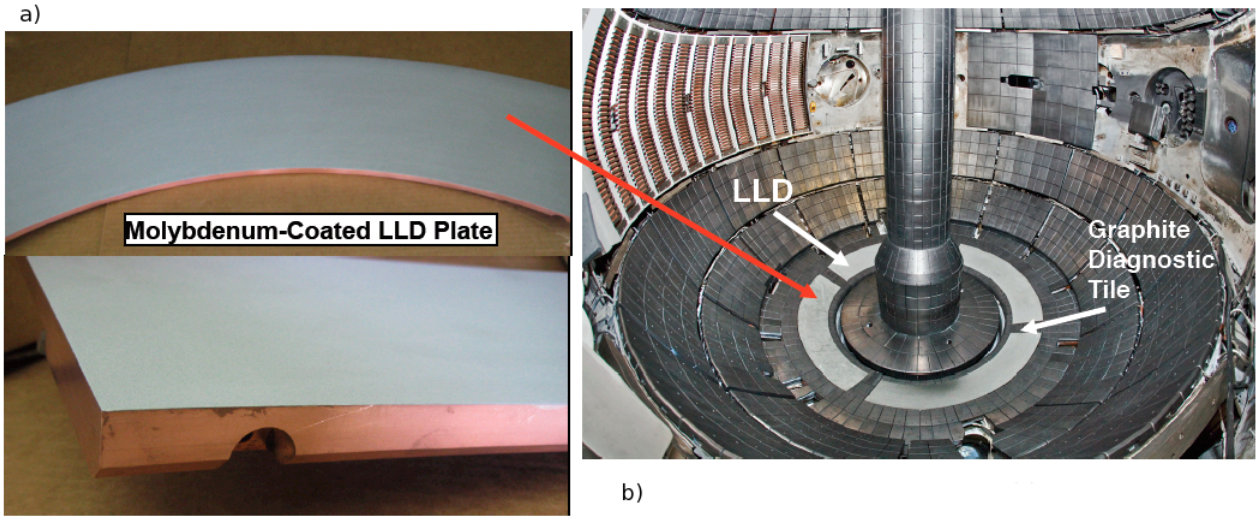

Figure 3.26: a) Individual LLD plate and b) all four plates installed in NSTX

to measure midplane density profiles under lithiated conditions, and could provide similar data under LLD operation. Utilizing 5.74 - 26.8 GHz microwave sweeps, it is capable of measuring 0.01 - 6.0 x $10^{12}/cm^{-3}$ electron densities, within the typical range of the NSTX midplane SOL. These measurements provide density profiles for determining how the midplane SOL profile is altered by the presence of the LLD.

Additional local impurity light emission measurements were enhanced by the installation of two downward-viewing Phantom v710 cameras to provide complete toroidal views of the LLD [68]. Depending on the resolution, these cameras can operate in the 7.5 kHz to 1.4 MHz range and have a spectral response that extends from 350-1050 nm, allowing the full visible and near IR wavelengths to be measured. A set of filters allows for specific impurity and main ion emission lines such as $D_{\alpha,\beta,\gamma}$, He I and II, Li I and II, C I, II, and III, Mo I and Fe I, and an IR bandpass filter. Full divertor spatial profiles can be reconstructed from these camera measurements, allowing for quantification of local impurity, heat, and recycling sources.

Another diagnostic takes advantage of the grounding scheme of the LLD plates, which calls for only a single point ground connection through a center post in each plate, designed to minimize eddy currents. This scheme ensures that all current transmitted through the tile passes through this single conduit. This feature allows for a straightforward measurement of the large currents that can occur during an NSTX disruption. To measure the magnitudes of these currents, a Rogowski coil was mounted around the center post of each plate [68]. This provides an effective means of determining the global currents induced in a disruption. NSTX discharges tend to terminate on the outboard divertor, and deposit the majority of the plasma current at the radial locations spanned by the LLD.

Another novel diagnostic installed for LLD measurements was a Lyman-α diode array [68] for measuring the hydrogen n=2 to n=1 transition at 121.6 nm. Due to metallic properties of liquid lithium, reflections of light from outside the spectrometer field of view can be a significant source of uncertainty in the visible wavelength range, where traditional

Balmer-α (D_α) measurements are made at 656.3 nm. This array consisted of a 1D-CCD camera viewing the divertor floor and made use of an absolutely calibrated extreme ultraviolet (AXUV) sensor for measurements. Unfortunately, overheating of the Lyman-α filter or amplifier malfunctions made array unavailable for 2010 run campaign measurements and did not provide data for the analysis described in later chapters.

Divertor heat flux magnitudes and profiles are provided by means of a two downward-viewing slow IR cameras operating at 30 Hz [69]. A high speed camera [29] was also used to provide 1.6-6.3 kHz measurements of the divertor heat flux. These diagnostics were instrumental in setting the design parameters for the LLD, but several new diagnostics were also necessary to assure optimal data collection in the new operating regimes anticipated with the LLD. Although a traditional IR camera is well-suited to providing heat flux profiles, calibrating the signal is complicated by the differing emissivities of solid and liquid lithium, especially if the lithium phase changes rapidly during a discharge as the LLD is heated by the incident plasma. It was thus necessary to develop a system that could account for this rapid emissivity change and provide accurate surface temperature and heat flux measurements. One method to eliminate the effect of emissivity changes is to use two separate IR wavelengths and then take the ratio of integrated IR emission. This, in combination with Planck's equation for emission, can yield an instantaneous LLD surface temperature useful in determining heat loading and probable phase state of the lithium. This diagnostic was utilized extensively in the present study, and is discussed in more detail in Chapter 5.

3.5.6 Inter-plate diagnostic tiles

The need for toroidal gaps between the LLD plates to limit current circulation provided an opportunity for the placement of diagnostics to measure local effects of the LLD. Four such radial gaps exist, and each one was filled with a particular type of tile. Biased electrode tiles were placed in the Bay E and Bay K gaps for use in SOL control. These electrodes

were based the a design for a set previously installed at the midplane [70] and utilized to control radial ExB flow. In order to attempt this control on a larger scale, the two gap tiles each had a pair of either radially or toroidally aligned electrodes installed, along with a corresponding suite of 5 Langmuir probes for local edge parameter measurements.

The Bay H gap maintains the existing 2D Mirnov coil sensors [41] for magnetic fluctuation measurements, and the toroidal orientation of the LLD is primarily set by a desire to maintain the existing 'clocking' of these sensors, i.e., providing poloidally contiguous measurements at a single toroidal location. The final gap, at Bay B, contains the tile that is the main focus of the remainder of this thesis, the dense Langmuir probe array tile. This tile was conceived of as a means of measuring with high spatial and temporal fidelity any changes to the edge density profiles that result from operating with liquid lithium coatings, and is discussed in depth in the following chapter.

Chapter 4

The Dense Langmuir Probe Array

Prior to the installation of the LLD, NSTX possessed a Langmuir probe system that provided some degree of poloidal coverage, albeit with relatively low spatial resolution [71]**.** These probes were based on a TdeV flush-mounted, single-probe design [72]. Five such probes were located in the lower outer divertor, although the magnetic limitations on the maximum major radius location of the outer strike point and shorting and arcing due to carbon dust accumulation meant that only two such probes were of practical utility by the 2009 NSTX run campaign. The changes to the NSTX divertor due to the LLD provided the opportunity for a new Langmuir probe system to be concurrently developed, fabricated, and installed in NSTX, with a focus on providing greater temporal and spatial resolution. An article detailing some of the aspects of the design of the array by the author can be found in Review of Scientific Instruments [73], but they are laid out in greater detail here.

4.1 Physics Requirements

The foremost goal of any diagnostic is to provide measurements on a relevant time scale and appropriate spatial resolution. Our particular interest was to measure the electron temperature and heat flux at the strike point divertor target and in the vicinity of the LLD. Such measurements would be able to provide a direct quantitative comparison among cases with

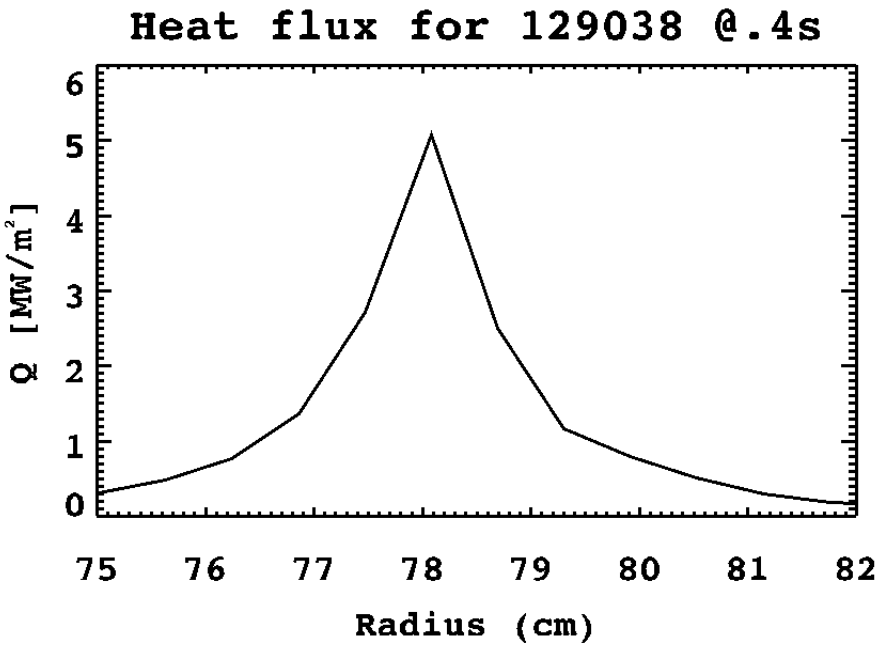

Figure 4.1: Heat flux profile at the strike point in a typical NSTX discharge

no lithium coatings, solid coatings, and liquid coatings. In addition, these data could then be utilized as the input to powerful simulation codes that can model macroscopic plasma behavior and transport, especially in the SOL. It is the desire to perform such measurements and understand the plasma processes driving them that guided much of the probe design process.

4.1.1 SOL widths

One of the primary concerns in probe design was the ability to capture phenomena at the scale length of the heat and particle flux gradients in the divertor region. Heat flux and density scale lengths on the order of 1 cm radially are common for NSTX discharges, and set the maximum probe size in this dimension [74]. Figure 4.1 shows the typical scale lengths and magnitude of outer divertor heat flux in NSTX. The figure shows a FWHM of 2 cm, and the radial resolution of the IR camera provides 5 measurements over this interval, essentially giving a 4 mm resolution for IR camera measurements and providing a

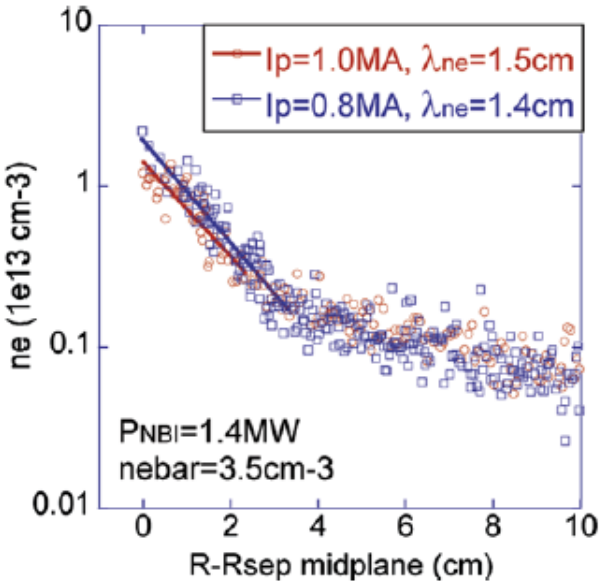

Figure 4.2: NSTX SOL density profile taken at z = -17.3 cm and mapped to the midplane [7]

benchmark for the probes.

Particle flux scale lengths at the divertor had not previously been measured in NSTX, but midplane data were available. A UCSD fast reciprocating Langmuir probe located 17.3 cm below the midplane had been used to measure SOL density and temperature profiles, as shown in Figure 4.2. The scale lengths determined are similar to the heat flux scale lengths, and can also be flux-mapped to the divertor target. This flux mapping is dependent on the magnetic geometry and other shaping parameters dependent on the individual discharge.

4.1.2 Temporal requirements

Time scales of events and features of interest set the temporal design constraints. Swept probes are able to provide full IV curves for edge temperature and density characterization, but practical limitations on the sweep frequency mean that they are of less utility for measuring temperatures during an ELM or fast turbulence. The temporal resolution needed for equilibrium measurements is not very stringent, as NSTX can have quiescent periods of tens or hundreds of ms, and the typical discharge lasts one second. Limits on the sweep

rate are generally set by the power supply used for biasing and the slew rate of various amplifiers in the probe circuitry. The digitization frequency can also play a role, as the higher the sweep rate, the fewer data points each IV curve will have. These electronics constraints are discussed below. The sweep rate of previous single probes in NSTX was typically 100 Hz - 1 kHz, and this was the desired operating range for the swept probes.

If measurements of transients are desired, divertor D_α light measurements show that ELMs can occur over 2-5 ms, with fine structure filament effects occurring over ~100 μs [28], and previous Langmuir probe data show turbulence on kHz to MHZ time scales [75], faster than viable sweep frequencies. To address this, it was decided that three sensors at each radial location could provide instantaneous triple-probe measurements, and a collaboration was established with the University of Illinois Urbana-Champaign to provide triple-probe circuitry.

4.2 Engineering Design Constraints

The engineering constraints also provided stringent conditions for the probe design. Steady-state heat flux in NSTX to the plasma facing components can be substantial: 1-10 MW/m^2, depending on the input power. A novel concern for NSTX divertor Langmuir probes is that a significant thickness (on the order of several μm) of evaporated lithium was to be deposited on the probes. The evaporators used to coat the LLD and described in Section 4.5 are positioned at the top of the machine, and also coat all of the surrounding surfaces. Elemental lithium is both conductive and corrosive, as well as being capable of reacting with underlying materials - the probe array and its supporting structures had to tolerate these lingering effects. Lastly, the spatial limitations for probes and wires precluded the use of many traditional assembly methods, such as securing wires with screws and mounting probes individually within the surface of the tile.

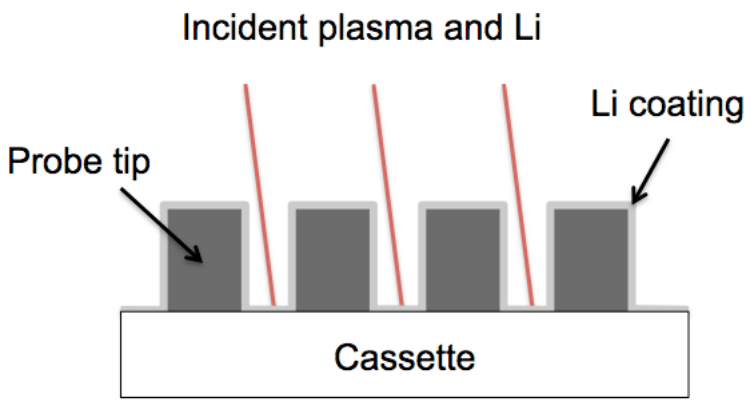

Figure 4.3: Cartoon showing interaction of plasma and lithium with straight-walled probe tips

4.2.1 Substructure protections

Although the probe tips themselves are intended to interact directly with the plasma and evaporated lithium coatings, the underlying surfaces and wires required protection from both lithium and plasma heat flux. This was necessary both to maintain the integrity of the surfaces themselves, but also to prevent excessive erosion of material into the discharge itself, a condition that can lead to radiative plasma collapse. In order to minimize this interaction, it was desirable to prevent a direct line of sight for both plasma and lithium incident flux. The simplest solution is to fill as much of the plasma-facing surface of the tile with probe tips, so as to minimize the gaps between probes. This method, however, competes with the constraint of maintaining enough distance between probe tips to prevent lithium bridges from forming and shorting out electrodes. In addition, a simple cylindrical or rectangular parallelepiped shape still allows fluxes with an inclination angle less than $tan^{-1}\left(\frac{height_{probe}}{spacing_{probe}}\right)$ to interact with the sub-structure, as pictured in Figure 4.3.

4.2.2 Materials concerns

One of the foremost issues related to probe design was the ability of both the probe tips and support structures to withstand the harsh environments present in NSTX. The most

basic requirement was that all materials be vacuum compatible, in that they would not be a significant outgassing source that could contribute impurities to the core plasma. There are a wide variety of materials that fit this description, but this does restrict the use of many adhesives that could aid in assembly. The next concern is the high heat flux incident on the probe tips. Instantaneous temperature rises due to plasma heating can cause cracking due to thermal stresses, but temperature ratcheting throughout a run day can also lead to increased erosion/sputtering rates which can not only affect the probes, but can also introduce impurities into the plasma. Damage due to differential thermal expansion of the probes and their housing can also result. The analysis and testing done to assess the thermal loads are discussed in Section 4.5. These concerns, while important, represent issues previously encountered in divertor probe operation.

The novel challenge facing the NSTX divertor probes was the large amount of lithium deposition planned for the 2010 run campaign and beyond. As discussed in Section 3.5.2.3, the LITERs have an efficiency of approximately 4-7%, requiring approximately 500 g to fill the 37 g capacity of the LLD. This is in addition to the 1-10 g of lithium deposited each plasma run day over the course of the 14 week run. The integral amount of lithium in the machine in 2010 was 1.5 kg. Using the density of lithium and the fractional area of a probe as compared to the whole machine, this results in a total deposition of approximately $400\mu m$. This lithium solidifies (and possibly oxidizes) nearly instantly after coming into contact with the probe surface, but can be heated by the plasma to a more readily reactive liquid state. Since the probes are in close proximity to the LLD, there also exists the possibility of direct liquid splashing onto the probe array during the course of an off-normal event. A study by Jeppson [76] shows the reactivities of common materials with liquid lithium. An additional constraint is that the probe material must also be electrically conductive, as conduction through the probe tip is the primary method of diagnosis.

Although modifications to avoid line of sight lithium deposition are utilized (discussed in Section 4.3), the probe mounting material must also be resistant to lithium corrosion

and heat flux as some plasma and lithium will still penetrate to the cassette floor. The cassette material must also be an insulator to electrically isolate the probes, as well as a good thermal conductor to aid in the removal of heat from the probe tips.

4.2.3 Spatial limitations

The spatial extent that the probe array could occupy was limited by the machine space provided, in this case a carbon divertor tile located between two LLD plates at Bay B, as seen in Figure 3.26. This was a very favorable location for measurement purposes, but a desire to have sufficient measurement resolution and the temporal resolution of triple-probes sets a maximum size for each individual probe tip. In addition, sufficient space must be reserved for the underlying mounting cassette and all of the probe wires and insulation. This also indirectly sets a current limit on the probes as the maximum wire size that could be used was constrained by the available space. The volume available for the entire probe apparatus was 2.5 cm vertically x 11.7 cm radially x 3.4 cm toroidally, as seen in Figure 4.4. This utilizes the maximum available tile volume, as screw bores for machine anchoring (seen adjacent to the array-mounting channel) were unable to be modified. This constraint then automatically sets maximum the probe width toroidally at ~7 mm for each triple-probe row. In order to prevent line-of-sight deposition, the maximum width must be the default width. The minimum spatial resolution of 4 mm (for IR camera comparison) and the radial extent of the channel then constrain the number of radial rows to 33. The factor that limits vertical extent, discussed further below, is the need to provide space for a mounting cassette and the underlying wiring.

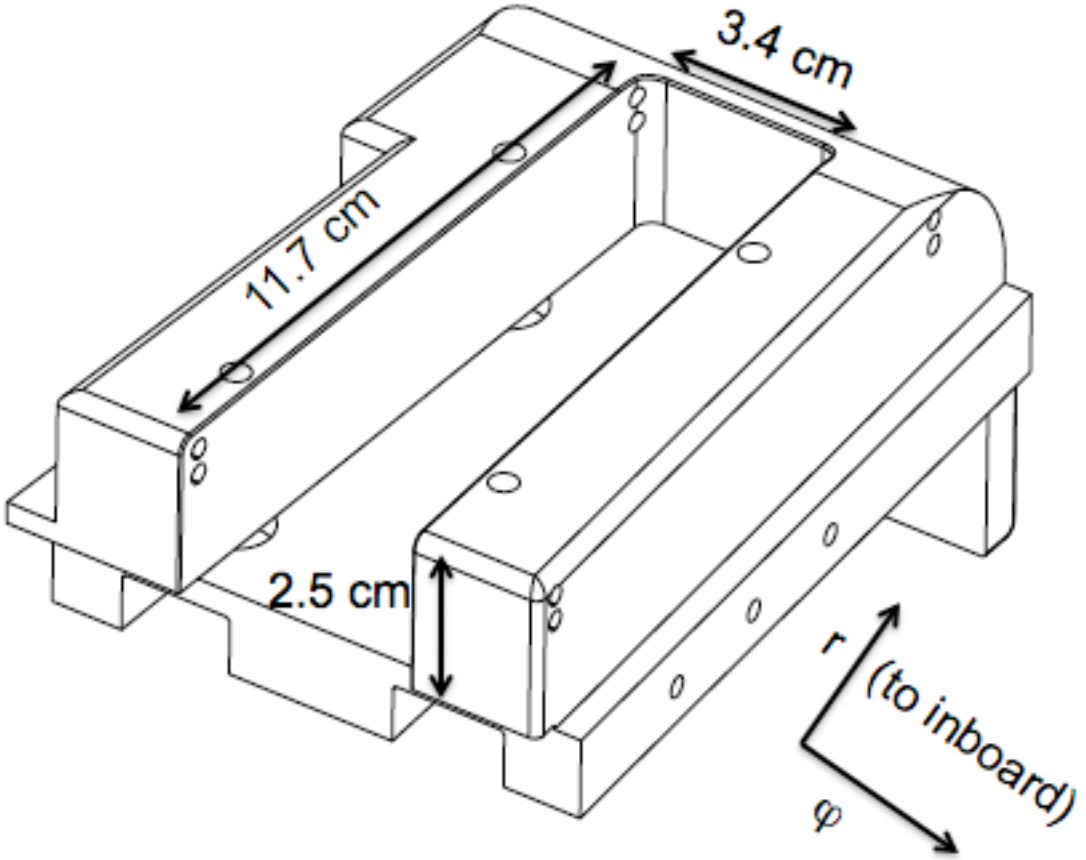

Figure 4.4: Drawing of divertor mounting tile for probe array

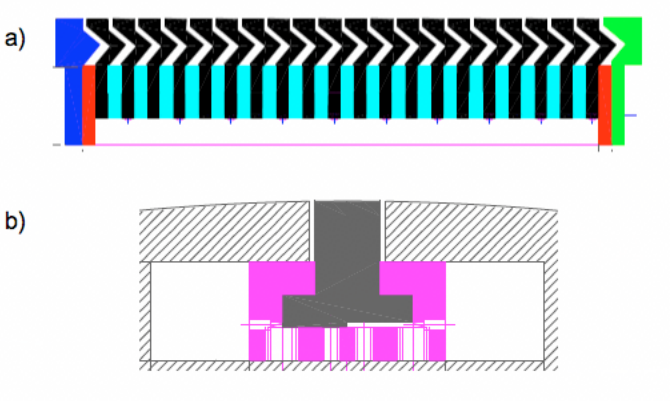

Figure 4.5: Side (a) and front (b) view schematics of MAST divertor Langmuir probe array [8]

4.3 Probe design

4.3.1 Original MAST Design

Several dense Langmuir probe arrays are installed in machines worldwide, and a survey was undertaken to find one that best matched the above requirements. After consideration of the potential concerns, a design based on the MAST divertor probe array [8] was chosen and modified to meet the NSTX needs. Two particular features of this array made it an attractive candidate for adaptation: the high density of probes and the bend introduced into each probe tip, seen in Figure 4.5a, which prevents line-of-sight plasma flux to the sub-structure.

Although this design provided a foundation for the final array, there were several issues that made it unsuitable for the present application. As seen in the front view of the probes in Figure 4.5b, the MAST probes are a single column of probe tips rather than the triple-tip probe layout desired in NSTX. This front view shows the supporting cassette extending far under the surrounding tile, which protects it from line-of-sight effects. If this same design were adapted for the triple-probes, the resulting toroidal spacing between probes would leave large gaps for plasma or lithium flux to enter. In addition, the probe materials were a potential concern, as the graphite probe tips and underlying MACOR cassette were

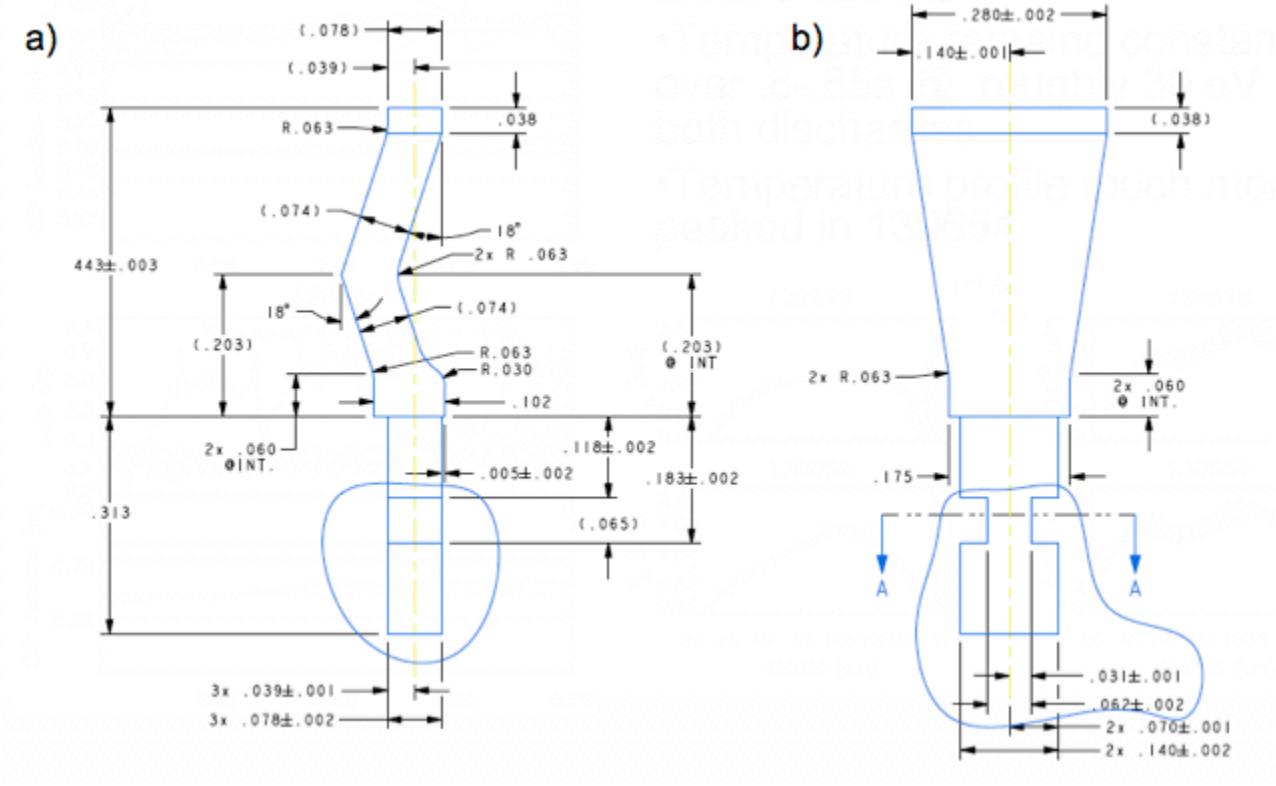

Figure 4.6: Side (a) and front (b) views of a single Langmuir probe tip. Dimensions are in inches.

potentially reactive with lithium.

4.3.2 Engineering design

Several design iterations were made and reviews conducted before a suitable triple-probe design was chosen. The probes were designed with rectangular heads with a dimension much similar to the MAST probes, 2 mm radially x 7 mm toroidally in NSTX vs 2.5 mm radially x 6 mm toroidally in MAST. The bend in the radial direction was retained, but a toroidally tapered design with sloped walls was chosen here to prevent line-of-sight effects in the toroidal direction as well. The final shape of a probe tip is shown in Figure 4.6. The narrowness of the base is necessary to allow enough space in the cassette for 3 tips per row and to retain enough cassette material to provide sufficient securement for each tip. The neck of each probe also contains two grooves for placement within the cassette itself. The

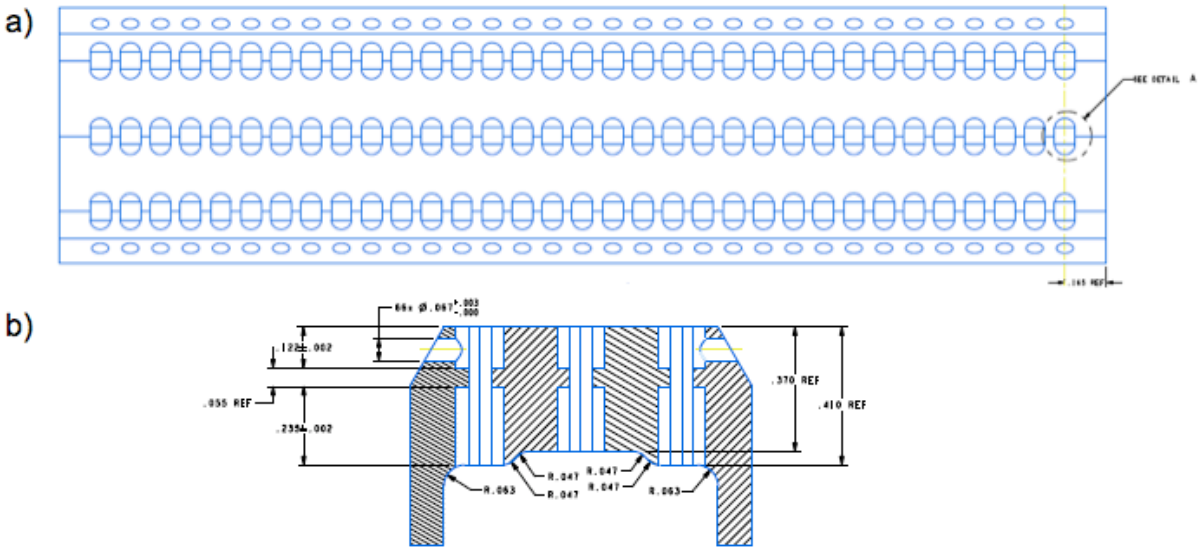

Figure 4.7: Top (a) and cutaway side (b) views of the probe cassette

original MAST cassette consisted of a single groove into which the probe tips and MACOR spacers were alternatingly placed. Horizontal attachment is provided by caps on each end of the groove, and vertical securement provided by the fins at the bottom of each tip as seen in Figure 4.5b. These fins, while effective, greatly increase the toroidal footprint of each probe and were unsuitable for present needs.

Our final groove design avoids this problem, but required a significant redesign of the cassette so that each probe could be seated individually. The resultant cassette design is shown in Figure 4.7. The cassette consists of four pieces, seen in Figure 4.8. The two edge and two center pieces are identical, for ease of manufacture. The holes in the sides of the cassette allow for the electrode wires to exit from the two side rows, while the center row wires exit through the bottom and are run in the gap under the cassette. Two end caps, shown in Figure 4.9 , are affixed with stainless steel pins to hold the final assembly together.

One feature noticeably absent from the design is the presence of screws to either affix the wires to the probes or hold the probes themselves in place. The high density of the probes makes such a method problematic, as the significant mechanical stresses introduced

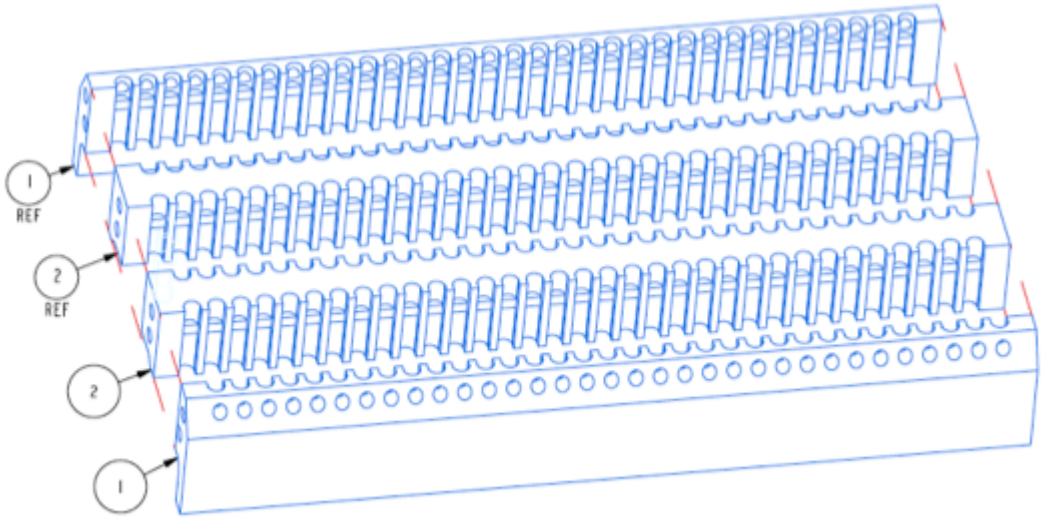

Figure 4.8: Exploded view of probe cassette, showing all four un-joined pieces

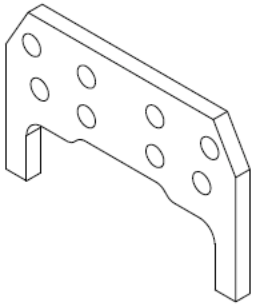

Figure 4.9: End cap for probe cassette

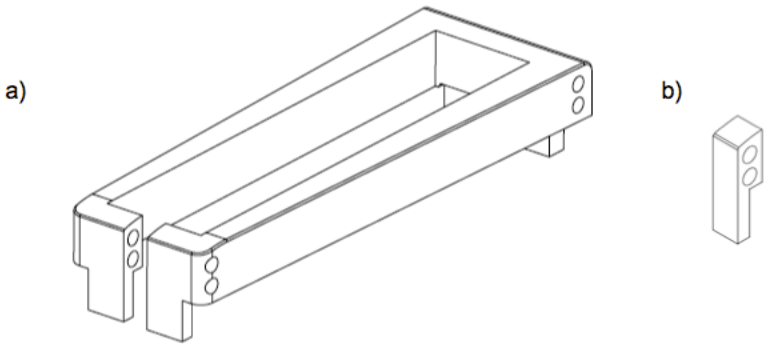

Figure 4.10: Keeper (a) and cap (b) for cassette-tile interface

into the cassette can cause it to fracture. The design of the cassette itself provides mechanical support and stability for the probes, but the issue of wire attachment still remains. This concern was surmounted through the use of graphite cement, which provided a method for bonding the wires directly to the probes without the need for mechanical devices such as screws. The wires themselves are 24-gauge, and the cabling run is discussed in Section 4.6.2.

The cassette is then mounted in the tile by means of a 'keeper', shown in Figure 4.10a, a brace which fits around the entire probe assembly and contains holes for fastening pins for attachment. The keeper also serves the dual function of providing protection for the exposed parts of the cassette, further reducing the possibility of line-of-sight plasma interaction. The keeper has a gap near the inboard side of the tile, where an additional cap, Figure 4.10b, is used to complete the assembly. The purpose of the cap is to aid machineability and allow for ease of installation.

4.4 Materials choices

A Langmuir probe can be constructed from any conductive material, but not all conductive materials are suitable for the lithiated tokamak environment inside NSTX. As described in Section 3.2.2, the NSTX divertor consists of a blanket of ATJ graphite tiles, and the existing divertor Langmuir probes are also fabricated from graphite. Although lithium can

Density	Thermal Conductivity	Specific Resistance	Flexural Strength
1.86 g/cm^3	90 $W/m \cdot K$	12.0 $\mu\Omega m$	85.0 MPa

Table 4.1: Tokai HK-6 Properties

Material	Density	Resistivity	Linear CTE	Thermal Conductivity @RT
Corning MACOR	2.52 g/cc	$>1 \times 10^{16} \Omega/cm$	9.3 $\mu m/m \cdot^\circ C$	1.46 $W/m \cdot K$
Boron Nitride	3.49 g/cc	$>1 \times 10^{14} \Omega/cm$	11.85 $\mu m/m \cdot^\circ C$	30.13 $W/m \cdot K$
ZSBN	2.9 g/cc	$>1 \times 10^{14} \Omega/cm$	1.98 $\mu m/m \cdot^\circ C$	40.21 $W/m \cdot K$

Table 4.2: Material properties of MACOR and boron nitride

corrode graphite, the existing Langmuir probes showed little evidence of signal degradation after lithium deposition during previous run years, potentially owing to no direct exposure to liquid lithium. Graphite was therefore a strong contender for the probe array material, especially given its thermal and mechanical properties, shown in Table 4.1. Molybdenum was also a potential material choice, as it is already the surface layer of the LLD and is unreactive with lithium, but cost concerns and issues with machining eventually let to the choice of graphite electrodes. The grade chosen was Tokai HK-6, the highest grade of electric discharge machined (EDM) graphite. EDM graphites are used in applications that require low wear and smooth surface finish and tolerances.

The cassette is essentially nothing more than a mechanism for holding the probes in place, and while there were no inherent restrictions on the material other than it be an insulator, it must satisfy the same requirements as the probes, i.e., be able to survive in a high heat-flux and lithiated environment. The MACOR used in the MAST probes was unsuitable for the latter reason, as **[76]** shows its potential reactivity with lithium. A similar machinable ceramic, boron nitride, was therefore chosen as a more lithium-compatible alternative. The grade chosen for this application was ZSBN, a high-strength BN variant, though the delicate work required to machine the cap necessitated the use of standard grade BN. The relative properties of the two materials are shown in Table 4.2. This was also chosen as the keeper material, as it was desired to place an insulator, rather than electrically conductive graphite, in proximity to the probe tips.

Graphite cement was used to cement the signal wires into cylindrical holes in the probes. This ensures a strong bond as the cement cures to essentially the same material as the probe tip, and eliminates the issue of differential thermal expansion that could occur with more traditional fastening methods. The cement contains volatile organic compounds, and thus testing was necessary to ensure vacuum compatibility, described in Section 4.5. The wire was OFHC copper, a standard wire type used in NSTX, and was threaded through glass braid insulation. OFHC copper of a 24-gauge size is capable of carrying a sustained current of approximately 0.5 A, which sets the maximum steady-state operating limit.

4.5 Analysis and testing

One of the primary issues raised in the design meetings for the probes was the question of heat handling capability. An analysis was undertaken to determine the temperature equilibrium point for the probes and testing was done to quantify the e-folding time for probe tip cooling.

4.5.1 Thermal equilibrium analysis

As a first step, a radiative equilibrium analysis was conducted, starting from the basic properties of the probes themselves. The single probe mass of $3.28 \cdot 10^{-4} kg$ is derived from the probe volume, calculated by the Pro-E software suite on which the probes were designed, and from the probe density, taken from the material sheet and given above in Table 4.1. The relevant surface area for radiative heat loss is $1.4 \cdot 10^{-5} m^2$. The heat capacity of $1600 \frac{J}{kg \cdot K}$ and emissivity of 0.85 are taken from material sheet. The probe temperature rise over a one second discharge at $10 MW/m^2$ of deposited power can then be determined by the familiar equation:

$$PAt = mc\Delta T \tag{4.1}$$

$$10 \cdot 10^6 \cdot 1.4 \cdot 10^{-5} \cdot 1 = 3.28 \cdot 10^{-4} \cdot 1600 \cdot \Delta T \tag{4.2}$$

$$140 = .525\Delta T \tag{4.3}$$

$$\Delta T = 266K \tag{4.4}$$

Assuming exponential cooling under radiation, an ansatz for the probe temperature is:

$$T = T_0 e^{-kt} \tag{4.5}$$

Given 600 seconds (10 minutes between discharges) as an allowed cooling time for 266 K:

$$T_0 - 266 = T_0 e^{-600k} \tag{4.6}$$

$$T_0 = \frac{266}{1 - e^{-600k}} \tag{4.7}$$

The purely radiative heat flux out of the probe can then be described by the Stefan-Boltzmann equation:

$$mc\Delta T = \int_0^{600} \varepsilon\sigma T^4 A \cdot dt, \tag{4.8}$$

where

$$3.28 \cdot 10^{-4} \cdot 1600 \cdot 266 = \int_0^{600} .85 \cdot 5.67 \cdot 10^{-8} \cdot T_0^4 e^{-4kt} \cdot dt, \tag{4.9}$$

and

$$1.4 \cdot 10^{-2} = 6.7 \cdot 10^{-13} T_0^4 \int_0^{600} e^{-4kt} \cdot dt \tag{4.10}$$

so that

$$2 \cdot 10^{14} = \frac{T_0^4}{-4k}\left[e^{-2400k} - 1\right]. \tag{4.11}$$

Substituting the expression for T_0 from Eq. 4.7 yields:

$$k = 6 \cdot 10^{-4} \tag{4.12}$$

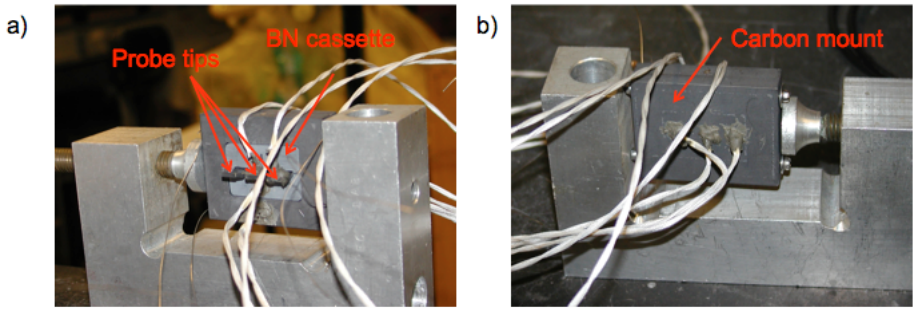

Figure 4.11: Front (a) and back (b) views of sample cassette used for probe array thermal testing

Substituting this back into Eq. 4.7 leads to:

$$T_0 = 886K \tag{4.13}$$

So, the probes will reach 613°C before they can radiate away all the power from a discharge. This represents a conservative estimate, as a heat flux of $10MW/m^2$ for one second assumes a maximum input power and the strike point depositing all of this power on a probe tip for the entire second. As plasma start and ramp-up usually take 200 ms or more, and the maximum input power is not planned to be used when the strike point is located on the LLD, the actual temperature rise should be much lower. Nevertheless, it was still deemed prudent to construct a test stand to determine the cooling response empirically.

4.5.2 Thermal testing

In order to determine the thermal response of the probe apparatus, a small-scale test array was assembled utilizing early probe tip prototypes. The array consisted of a single row of three probe tips placed in a boron nitride cassette and then inserted into a dummy graphite block. Seven thermocouples were installed at various locations to monitor the temperature of different parts of the array, and the apparatus is pictured in Figure 4.11. The probes are held in place through grooves in the boron nitride cassette, much in the same way

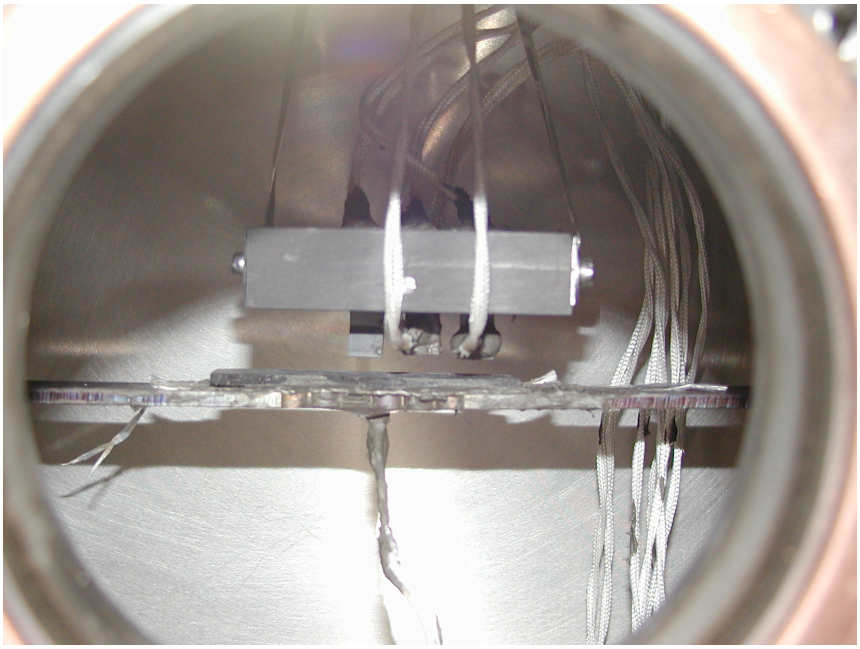

Figure 4.12: Probe heat test assembly in vacuum chamber

they are in the real array. The cassette itself is secured by means of a single compressive screw, as the machine tolerances for this mock-up left a slight gap between the cassette and carbon. The thermocouples were secured in place using the same graphite cement planned for final wire attachment, as this would provide an opportunity to test its strength and vacuum compatibility.

Heating was provided by means of a resistive stainless steel strip placed between two high-current leads. An additional thermocouple was installed for monitoring the heating strip temperature. A thin graphite strip was also attached to the resistive heating element with graphite cement in order to provide a uniformly heated area for the probe tips. The entire probe assembly was then suspended from a linear motion feedthrough by means of two stainless steel strips. The final experimental setup is pictured in Figure 4.12.

The chamber was then evacuated to a pressure in the 10^{-7} Torr range, indicating that outgassing of the graphite cement would not be a hindrance to achieving good vacuum conditions. Thermal tests were conducted by raising the resistive heating element to approximately 700°C and then lowering the probes to come into contact, as pictured in Figure

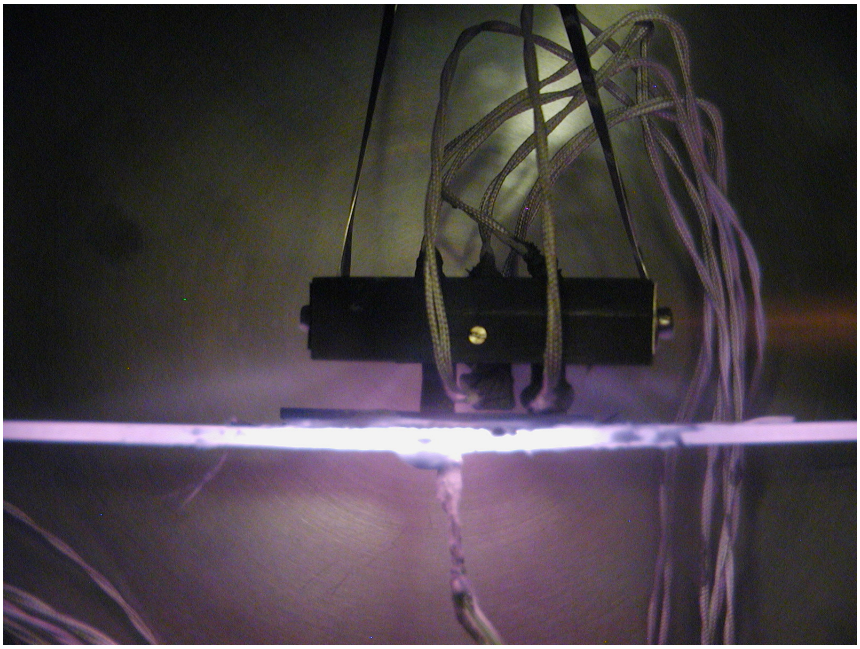

Figure 4.13: Probes in contact with heating element during thermal testing

4.13. The probe tip in best thermal contact with the heating element was able to reach temperatures of up to 350°C, at which point power was cut to the heating strip and the probes were raised up the 1" stroke of the linear feedthrough. Temperatures were recorded every two minutes initially and then every five minutes as the cooling slowed.

A typical cooling curve along with fitted exponential cooling response (from equation 4.5) is shown in Figure 4.14. The e-folding time calculated is 27 minutes. This is again a conservative estimate, as the sample was thermally isolated from its surroundings rather than in thermal contact with surrounding tiles and the underlying copper passive plate to which it will be attached during installation. It demonstrated that the cooling time was on the order of the shot cycle duration and not so large as to limit shot repetition rate.

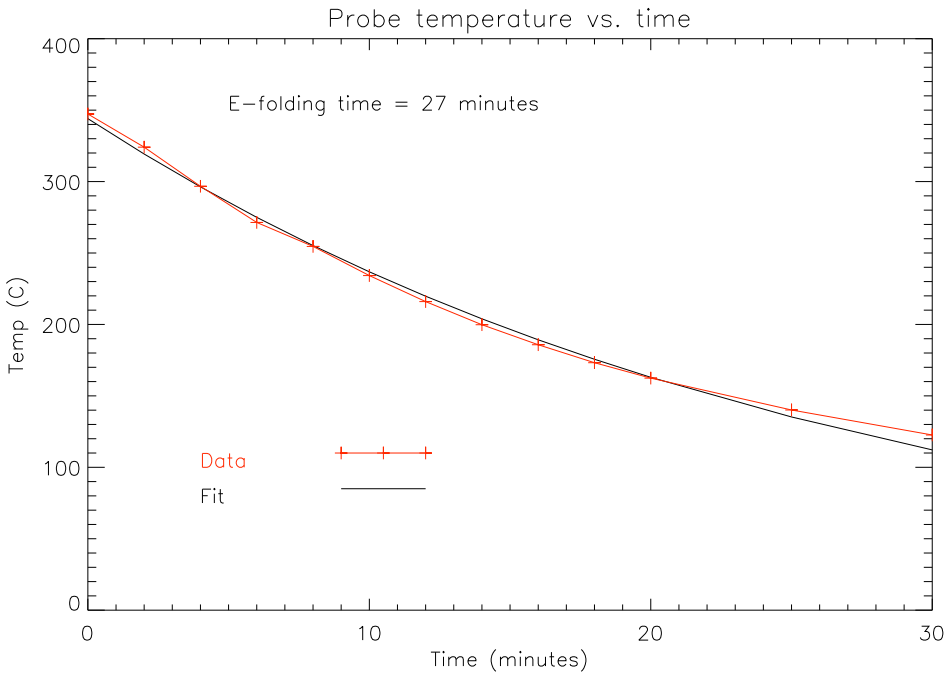

Figure 4.14: Cooling response of heated probe tip during heating tests

4.6 Assembly and In-vessel Installation

4.6.1 Assembly

All of the components for the probe array were manufactured by Zenex Precision Instruments, based on a set of engineering drawings that includes the figures cited in Section 4.3. The probe array was assembled in stages, and the design lends itself to a preferred order, beginning with the assembly of probe tips and wires.

The probe tips came machined with 1 mm diameter holes for wire insertion that reached a depth of 2.5 mm, as seen in Figure 4.15. It was decided, however, that in order to avoid blind holes as much as possible and to increase the strength of the graphite cement bond, the holes in the side rows of probes should be extended all the way through the tip. This was accomplished by means of a 1/32” hand drill. The 24-gauge copper wire was then cut to 2 m lengths for the initial cable run, and inserted completely through the mounting hole and affixed with the graphite cement. The cement requires a 1-3 hour air-curing period,

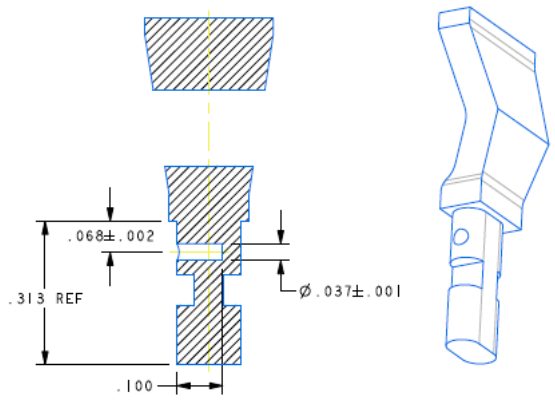

Figure 4.15: Probe head detail showing wiring hole (dimensions in inches)

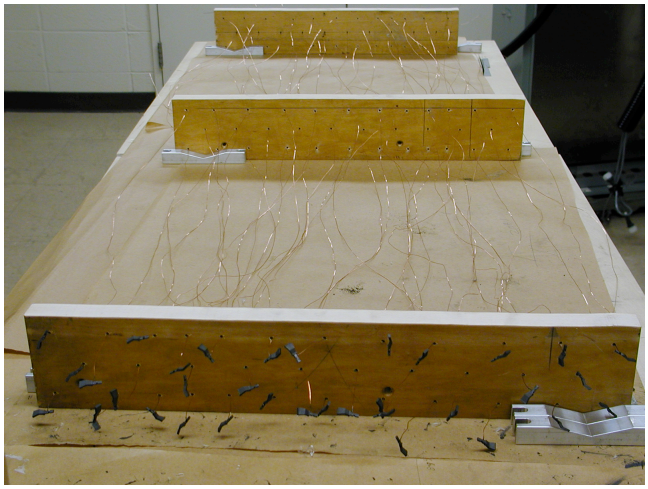

Figure 4.16: Probe drying apparatus

and a drying stand, shown in Figure 4.16, was constructed for this purpose so as to allow for maximum air throughput. The cement then had to be heat-cured at 245°F for at least two hours, which which was done in 10-probe batches on a hot plate. After this step was completed, the excess cement was trimmed and filed away, and the bond was tested for strength with a vigorous arm pull (roughly 20 N). Probes that failed this test were re-cemented and tested again following the heat cure. An electrical continuity check was also performed to ensure a resistance below an arbitrary threshold, here set at 10 Ω. Typical resistances were in the 0.7-8 Ω range. The failure rate for a cement bond was approximately 10%, but improved throughout the process as the author's technique in applying the cement

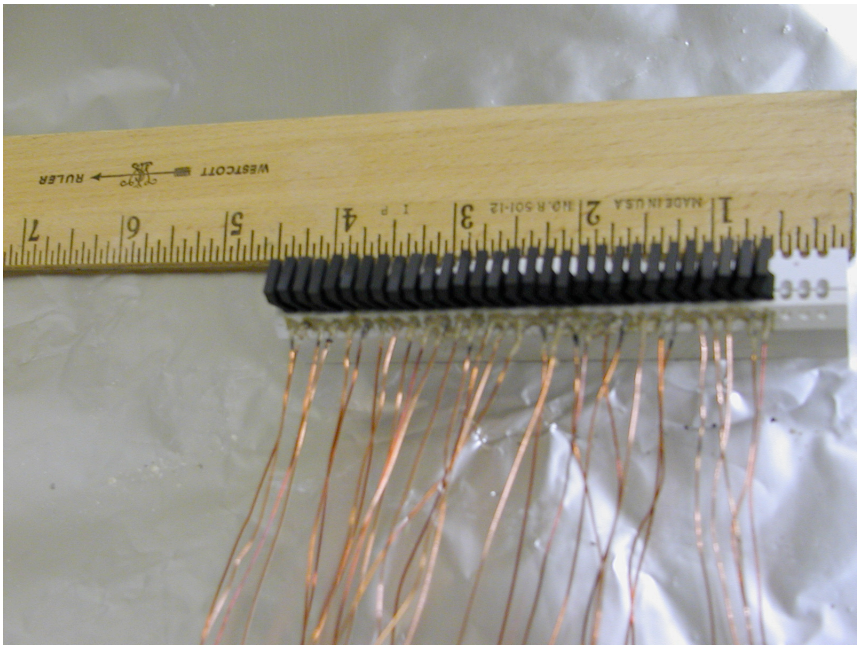

Figure 4.17: Completed side cassette probe row

to fill the voids improved.

Once all 99 probe tips (and a few spares) were assembled by this method, the probes were seated in the BN cassette quadrants. The side rows were assembled first: probe wires were threaded through holes in the sides of the cassette, and then Fortafix, a vacuum compatible adhesive, was applied for strain relief. A finished 33-probe side row is shown in Figure 4.17. The next step was to thread the insulation over the probe wires. This could not be accomplished for the side rows before mounting due to the fact that the 18-gauge glass insulation material could not fit through the wire holes on the sides of the cassette, and therefore had to be threaded once the probes were seated. The central row did not have this issue and the insulation could be threaded at the time of probe tip assembly. The method of threading the insulation involved first threading a large-gauge wire through the insulation and then soldering it to the smaller probe wire. This allowed the insulation to be easily slid onto the smaller wire without much friction, and the large wire could then be cut away. Since the assembled probe elements were very fragile at this juncture, a careful system of strain relief was utilized to ensure that damage did not occur. A continuity check

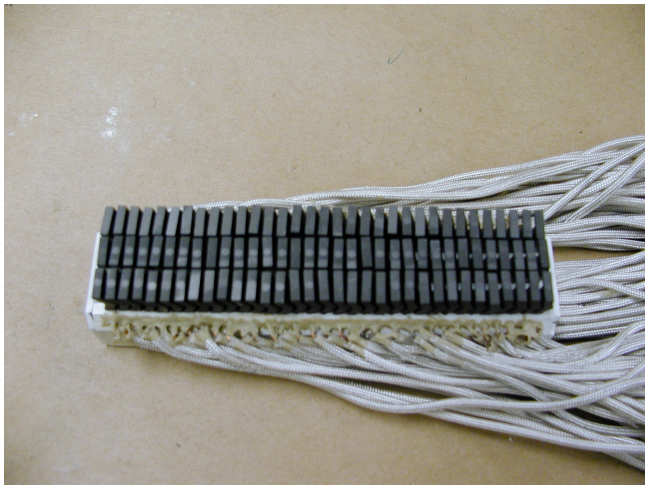

Figure 4.18: Completed cassette assembly

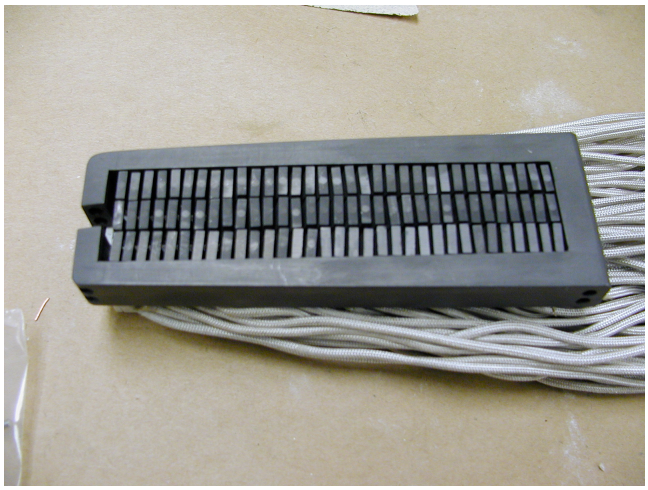

Figure 4.19: Cassette with boron nitride keeper in place

was again performed, and any probes which failed were replaced with spares.

Once the two side cassette pieces were assembled, the center probes were seated in the middle row, the wires attached with Fortafix, and the cables run out the groove under the cassette. The entire cassette assembly (after some filing of protruding graphite surfaces) was secured by means of the end caps and stainless steel pins described in 4.3. The resulting cassette structure is shown in Figure 4.18. The BN keeper was then mounted over the cassette, as shown in Figure 4.19. As seen in the picture, a flaw with the probe mounting method is that after some of the excess graphite cement had been filed away, the probe tips

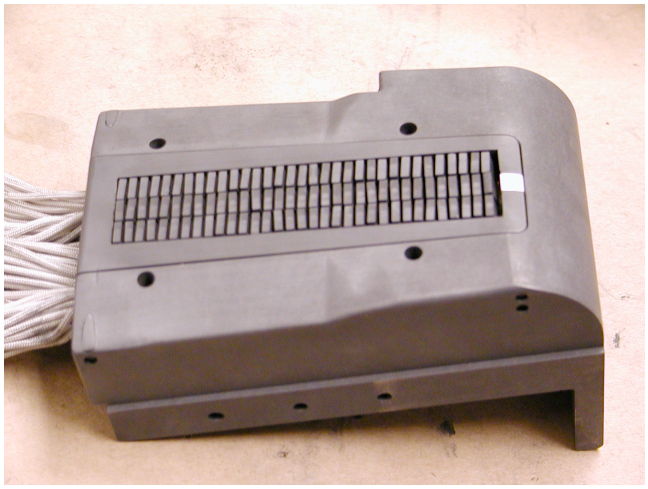

Figure 4.20: Completed tile assembly

were not perfectly aligned in the keeper, though held securely. To deal with any shorting issues this could potentially introduce, the tips were sanded slightly to increase the gap between the probes and the walls and between each other. Electrical continuity checks were again performed to check for damage or probe shorting. The entire assembly was then mounted in the tile by means of the graphite pins described in 4.3. The pins also had to be filed to conform with the chamfering added to the tile surface to allow for interface with the as-built LLD, which was of a different height than the intended LLD design on which the probes were based. This chamfering step is described below in Section 4.6.2. The complete assembly can be seen in Figure 4.20.

One final step remained before installation, which was the labelling of the individual probe wires. This was necessary as the 2 m wire run from the array was not sufficient to reach an NSTX feedthrough. It was decided to keep this wire run short to ease assembly, although this design requires a splice to a longer cable for the final feedthrough run. To ensure proper connections, it was necessary to label the wires originating from the tile and have corresponding labels for those extending to the feedthrough. This identification was accomplished by means of small plastic beads, of which there were 5 colors. Using a base-5 numbering system, one can describe all 99 pins using three beads. The beads were placed on a small loop at the ends of the wires to allow for ease of removal and to prevent stray

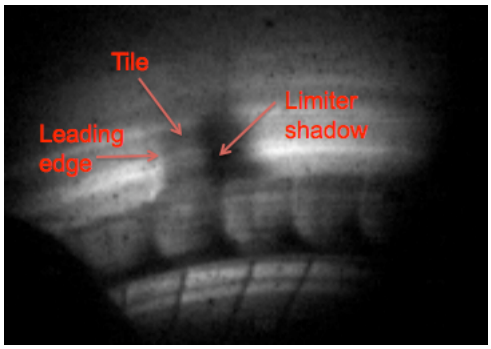

Figure 4.21: View from NSTX camera during plasma shot 137622 through Li I filter showing tile, leading edge, and limiter shadow

beads from ending up in NSTX. Probe tips were identified by means of resistive continuity, which also served as a final check on the wiring before installation.

4.6.2 Installation

As mentioned above, the tile required some modification before it could be installed in NSTX. The actual height of the LLD in the machine was approximately 1/8" lower than originally intended, so the tile had to be machined to match so as not to be too proud relative to the LLD surface. As the assembly was nearly complete when this situation was discovered, the design of the array could not be reworked and an alternative solution was necessary. As the probe tip height was now immutable without massive reconstruction, a tapered design was adopted. Before the cassette assembly was inserted, the two long (toroidal) edges of the tile were lowered by the necessary 1/8" and then the tile surface coradial with the LLD was tapered so as to match the probe height in the middle, leaving 1/8" on each side of the keeper so as to provide a leading edge limiter to protect the probes. This design, the one shown in Figure 4.20, implements the desired LLD interface but essentially turns the tile into a poloidal limiter and provides a larger surface area on which the plasma can deposit heat flux. A limiter shadow is visible when the plasma comes into contact with the tile, as seen in 4.21.

Once the modifications were complete, the tiles outboard of the probe array had to

be machined as well to accommodate the wire runs. The wires were separated into three bundles, measured, and then the tiles were machined to fit by NSTX technicians. The probe array was brought out to the vessel for installation, seated, and then the corresponding outboard tiles were seated once the wires had all been fit properly. The initial wires run from the tile were only 2 m, which was enough distance to reach behind the NSTX passive plate and out of plasma view for the final run to the feedthrough.

This last section of cable had the same gauge wire and insulation, but was covered with a stainless steel braid to reduce noise pickup. The total secondary wire length was approximately 4 m, with the stainless braid covering the 2 m of toroidal run to reach a vertical section of pipe that extended downwards to the feedthrough. The final 2 m of wire that extended down the pipe had the braid stripped to ease the space constraints, as much of the wiring for the LLD and its related components shared similar feedthrough access. Due to the hydrocarbon residues from the manufacturing process of the braided wire, all of these secondary wires required ultrasonic cleaning before they were vacuum qualified prior to installation.

Once the wires had been prepared, they had to be labeled with the same beading system described above in Section 4.6.1 in order to ensure that the proper connections were made. The secondary wires were then spliced to those originating from the tile by means of a small stainless steel hypodermic tube, into which both wires were inserted and which was then crimped to ensure good electrical contact. An additional piece of insulation (previously threaded over the wire) was then cemented in place with Fortafix to ensure that no conducting surfaces were exposed. The 99 wires were then connected to four 32-pin feedthroughs to bring the signals out of the vessel. A picture of the installed tile can be seen in Figure 4.22.

The next step was to ensure that the wire labeling system had been effective, and that all probes had electrical continuity. To test this, an ohm-meter was used to measure both the resistance between the probe tip and the corresponding feedthrough pin and the probe tip

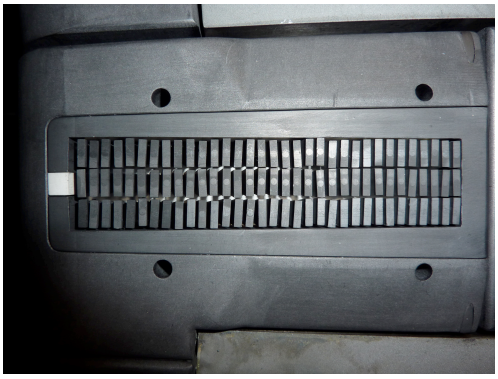

Figure 4.22: View of the probe array installed in NSTX

and ground. This meant that one person had to apply one of the ohm-meter pins to the probe tip, and another person the other to the feedthrough pin. It was found that all 99 probes exhibited continuity to their appropriate pins and were isolated from each other. Although two pins exhibited non-infinite ($> 10M\Omega$) resistance to ground, it was later verified after pump-down that this finite resistance had disappeared.

The final in-vessel step was to determine the absolute probe location so as to verify where measurements were taken. This was done utilizing the NSTX FARO arm, a commercially available measurement device that provides an absolute radial and toroidal location in the vessel by positioning its tip, in this case placed at several calibrating points on the tile. Figure 4.23 shows the author and several NSTX engineers measuring the probe locations inside the NSTX vacuum vessel. A table giving all of the probe locations in NSTX coordinates can be found in Appendix A.

4.7 Post-run conditions

This section provides some brief visual evidence of the survival of the probe array following the 2010 run year, confirming the validity of the analyses in this chapter. Figure 4.24 shows the probe array at the end of the run, exhibiting depositions of lithium compounds and the very few instances where lithium has bridged the gap between electrodes. Figure 4.25 shows the probe array after a cleaning procedure involving vinegar and Q-tips to react

Figure 4.23: The author along with Craig Priniski and Dan Stevens measuring the probe locations in NSTX

Figure 4.24: Probe array after 2010 run year, pre-cleaning

Figure 4.25: Probe array post-cleaning

away the lithium compounds. The array resembles its pre-installation state and shows that it was able to successfully survive both the heat and lithium loads of an NSTX run year. Some residue was found between the probes, but checks with an ohm-meter showed them to be electrically isolated from one another. This residue consisted of compounds that were of a whitish color and dissolved with vinegar application, resembling the lithium carbonate deposits found elsewhere in the vacuum vessel following venting to atmosphere. Lithium carbonate is an insulating compound which forms when there is an abundance of carbon dioxide, and which is believed to form after exposure to atmosphere. Lithium hydroxide, most likely its precursor, and which more commonly forms in water-rich high vacuum environments, is an insulator as well.

4.8 Ex-vessel electronics

Only a brief description of the ex-vessel electronics are described here, as a more complete description can be found in a paper by M.A. Jaworski. Circuit diagrams can be found in Appendix A. The electronics were prepared as part of a collaboration with the University of Illinois at Urbana-Champaign One of the most important design features is a patch-panel, which allows individual probe tips to be associated with any of the different probe circuits, allowing for quick reconfiguration should a tip malfunction, to measure in a different location, or to change the type of probe measurements.

4.8.1 Single Probes

Initial electronics were provided for four single swept probe tips. A 400W, $\pm$50V Kepco bipolar power supply provides the driving voltage, while a Wavetek programmable function generator provides the input waveform, most commonly between 100 and 500 Hz.

4.8.2 Triple Probes

Any three probe tips can be wired together using the patch-panel into a triple probe. The initial installation provided for 10 triple probe sub-units, which bias the positive and negative tips at 48 V relative to each other, referenced to the third, floating tip, which provides the reference voltage.

4.8.3 SOL Current Perpendicular and Parallel

The SOL current probes provide an electronics feature implemented to utilize the probe tips as current monitors, either referenced to the inner vacuum vessel through a resistor for parallel SOL current flows, or to another probe tip within the array for perpendicular SOL current measurements. These measurement techniques are custom uses of the probe tips, and are not discussed in this thesis in detail.

Chapter 5

Experimental Derivation of Sheath Heat Transmission Coefficient

The present study relies on two complementary diagnostics to provide an accurate picture of the sheath heat transmission coefficient, γ. As mentioned above in Section 2.5.2, the equation that describes sheath heat transmission is $q = \gamma k_B T_e \Gamma$. It is therefore necessary to know the heat flux directly, as well as the electron temperature and particle flux. The former is provided by an IR camera, described below in Section 5.3, while the latter is provided by Langmuir probe data. This chapter is concerned with the methodologies applied to the measured signals from both diagnostics, and how they are analyzed and combined to produce a result for γ.

5.1 Single Probe Signal Analysis

Much of the theory behind single-tip swept Langmuir probes has already been described in Section 2.6.1. This section instead focuses on the practical realities of probe data interpretation and the computational analysis methods used to produce input data for sheath heat flux comparison.

5.1.1 Circuit Contributions

The electrical diagrams for the single probe circuitry are provided in Appendix B, but are only part of the overall Langmuir probe system. Each probe tip exists as a physical, carbon entity in the machine, and is connected to the circuit through a copper wire down to the vacuum feed-through. The resistance of the tip itself and the graphite cement connecting it to the wire both contribute to the voltage (and thus inferred current) measured by the digitizer. In an effort to quantify these contributions, measurements were made before the run campaign of the tip to feed-through resistance using a standard ohm-meter and recorded to two decimal points of precision. The typical resistances measured fell in the $2-50\Omega$ range, with the bulk of the measurements lying between $2-10\Omega$. These values were recorded and used as corrections to the measured probe currents in the analysis codes.

In the circuit itself, the sensing resistor, across which the probe current is measured, must also be taken into account as it affects the measured bias voltage applied to the probe. These resistors have a magnitude of 2Ω, and therefore the net contribution to the measured voltage from the in-vessel hardware and sensing resistor is $V_{offset} = (R_{probe} + R_{sense})I_{probe}$. By analyzing the circuit network, the attenuation that occurs in the circuit before the signal is digitized can also be determined. This results in a gain of 200 V/V for the bias voltage signals, and of 0.5 A/V for the current signals. Due to the 1% precision resistors used in the circuit, an approximately 3% uncertainty is also added into the measurements. By multiplying by these gain factors and adding the correction described above, a voltage and current signal at each time point (in this case every $4\mu s$) are then measured. Of additional note is that although the digitizers record at 250 kSamples/s, a low-pass filter is applied with a cutoff of 133 kHz to reduce the effects of high-frequency noise. The digitizer itself has 16 bit resolution, which has significant dynamic range for the signal-to-noise ratios in the probe measurements.

The signals obtained through the digitizers are then stored within the MDSPlus [77] database tree for later use. The database stores the raw digitizer signals, the gain values,

the electrode associated with each signal (including its radial and z-positions as well as its resistance), and the timebase of the measured signal.

5.1.2 Temperature, Saturation Current, and Floating Potential Fitting

A code was developed to extract the signals stored in the MDSPlus tree and turn them into meaningful physical data. The first stage of the code simply retrieves the MDSPlus signals stored in the tree for a given discharge and utilizes the gain factors to convert them into actual currents and voltages. The next step involves converting a raw signal into a well-defined voltage sweep, which simply involves knowing the sweep frequency and digitizer frequency. If both values are known, then the number of data points per sweep can be obtained by dividing the digitizer frequency by twice the sweep frequency. The endpoints of a sweep can be found by taking the minimum and maximum of the voltage signal within this range. By checking whether the voltage maximum occurs before or after the voltage minimum in the vector region of interest, the code can determine whether it is looking at the positive or negative portion of the voltage sweep. If it is the positive portion, then the corresponding voltages and currents are placed directly into a secondary variable that holds the I-V curve for this time point (defined as the average of the time vector for this interval). If it is the negative portion, the signals are then inverted before being placed into the secondary variable. This method is depicted graphically in Figure 5.1, which shows an initial region being examined, the slope identified, and the maximum used as the starting point for the next sweep, which will invert the data order before placing it in the array.

This standardizing of the variable format for both positive and negative sweeps allows for a doubling of the effective resolution of a single sweep period. This higher resolution allows for a retention of a large number of data points when multiple sweeps are combined to smooth out noise and fluctuations. To further smooth out high-frequency noise, the voltage signals are also separated into a user-specified number of bins. The voltages and

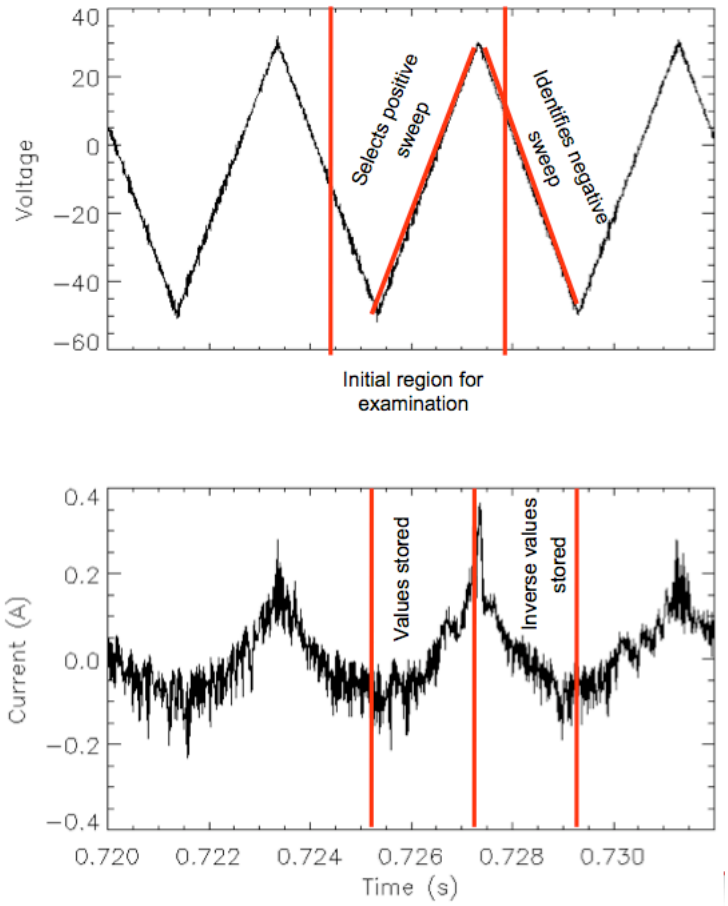

Figure 5.1: Data sorting technique for using all the parts of the probe trace

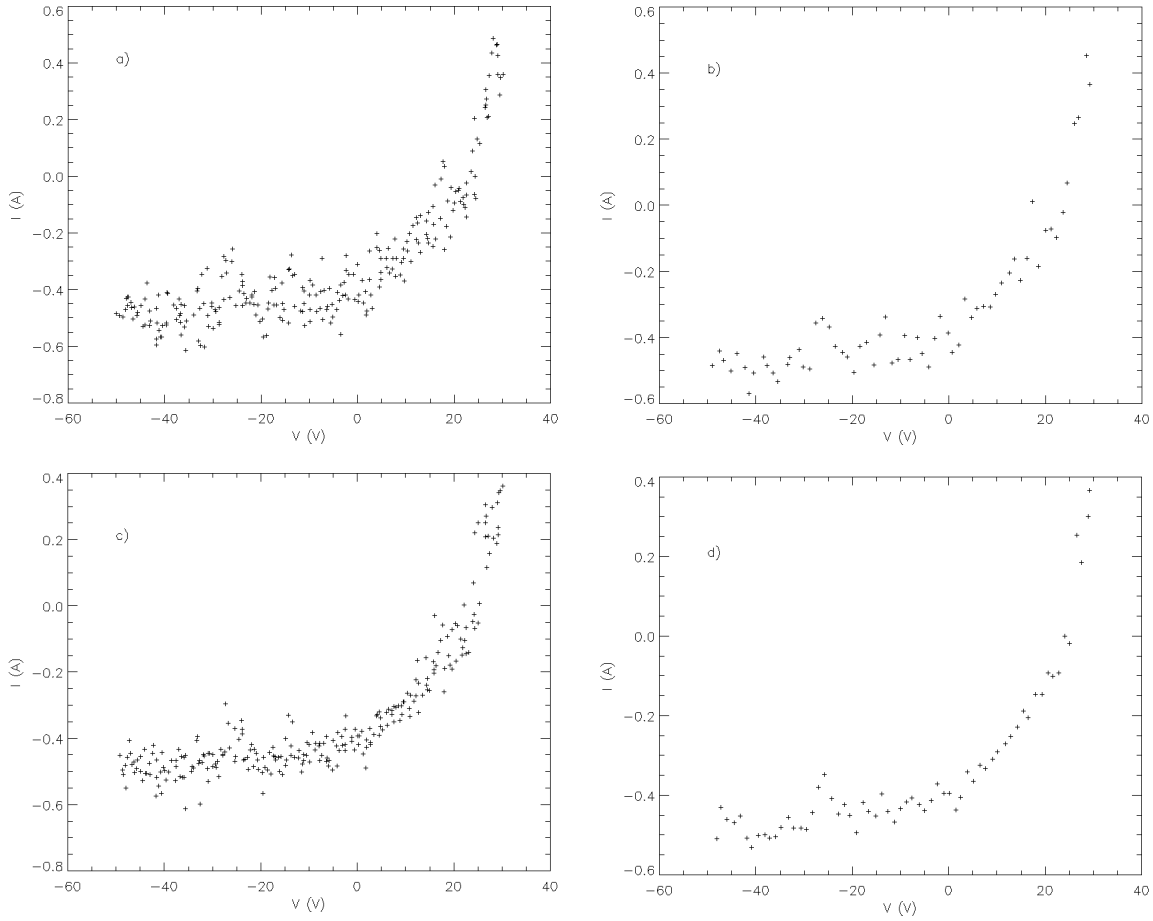

Figure 5.2: Results from different smoothing methods of a single time point (720 ms) in shot 139622. a) no smoothing. b) one sweep, 3 voltage and current points per bin. c) smoothing of 4 traces with no binning. d) smoothing of 4 traces with 3 voltage and current points per bin

currents in each bin are then averaged to produce an average current at an average voltage within each bin. These two smoothing factors can be used to greatly reduce the noise present in a 'single' effective I-V sweep, as pictured in Figure 5.2. This ultimately resulted in a choice of 3 voltages per bin and the combination of three individual sweeps per signal utilized for analysis.

A three-parameter exponential fit is then applied to the I-V curve, utilizing the single probe current equation, Eq.2.40. The free parameters are the ion saturation current, floating potential, and electron temperature. Due to the large electron current measured with respect to the ion current, the swept probes are run from -40/+28 V. Previous efforts to measure

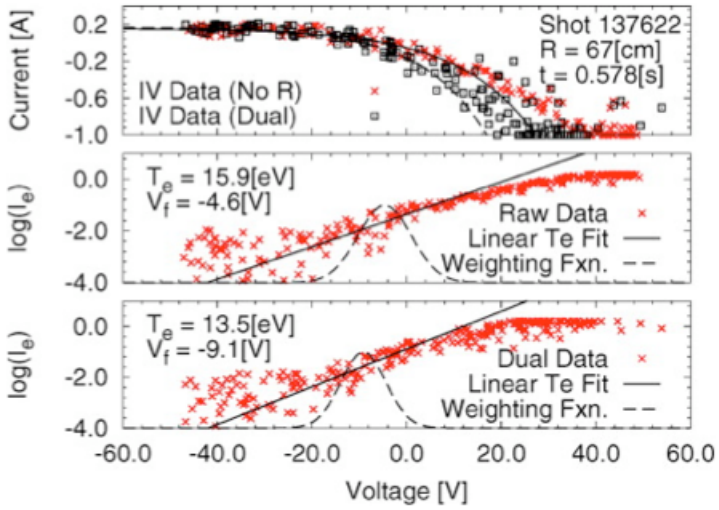

Figure 5.3: Probe fitting using different weighting for single probe current trace. The change of fitting region affects the measured temperature. Reproduced from [9]

electron temperature in magnetized plasma regimes will often discount any portion of the probe current that lies above the floating potential, assuming that it no longer follows the standard exponential Boltzmann response [[78]]. This choice, however, restricts the electron data to the highly energetic particles at the tail of the electron distribution and thus reduces the available data set. Depending on the floating potential voltage, choosing to cut off the electron contribution at different voltage values in the sweep causes a difference in measured temperatures of up to 50%. The other quantities, as expected, are minimally affected by this choice, generally varying by under 10%. This method is demonstrated graphically in Figure 5.3.

As a greater portion of the electron branch is taken into consideration, the chi-square of the exponential fit also increases, which provides a method to quantify the uncertainty obtained in the fit. A temperature fit is obtained for six voltage cutoffs, beginning at the full sweep and ending at approximately the floating potential. A weighted average of the fitted temperatures, floating potentials, and ion saturation currents is then taken, with the contribution of each fit being the inverse proportion of its chi-square to the sum of all the obtained chi-squares for all six fits. The error bars are then defined by the minimum

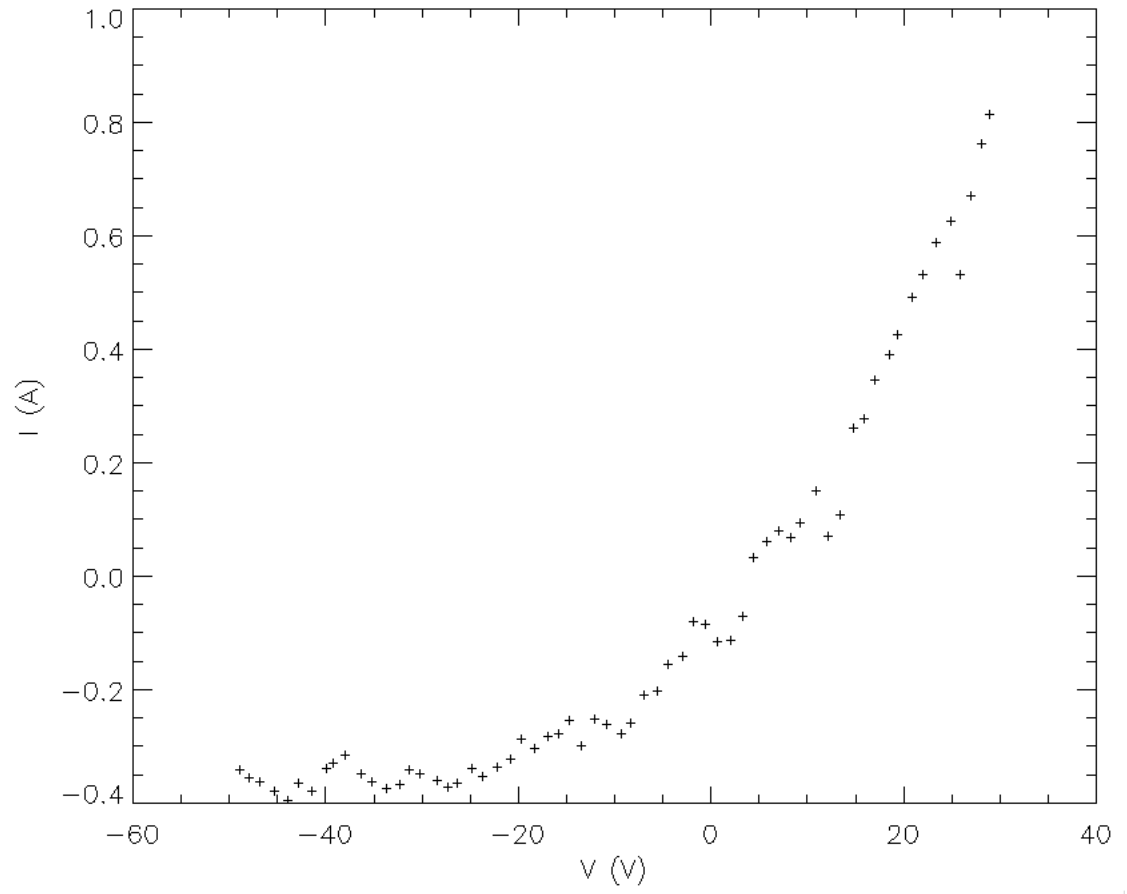

Figure 5.4: Probe characteristic used for fitting study, from 139622@.7s. Smoothed over 4 traces and binned into 3 points/bin

and maximum values obtained for each parameter normalized by their inverse chi-square weights. The results of this fitting method can be seen in Figure 5.4 and Table 5.1.

5.1.3 Density Determination

Once the temperature and saturation current are known, the density can be obtained from Equation 2.41, with the electron temperature providing the input into the sound speed. The uncertainties here carry over from those obtained in the determination of the saturation current and density described in the previous section. A final term is necessary for an accurate measurement of the density, which is the area of the probe. This area only corresponds to

Cutoff Voltage (V)	Temperature (eV)	$I_{sat}(A)$	Floating potential (V)
2	15.5	0.39	5.4
7	14.6	0.38	4.7
12	18.3	0.41	5.7
17	19.1	0.41	5.9
22	19.1	0.41	5.9
27	22.3	0.44	5.5

Table 5.1: Comparison of derived probe quantities vs. cutoff voltage

the physical probe area when the particle flux is exactly normal to the probe surface, which is far from reality in a tokamak environment.

5.1.3.1 Magnetic Field Angle

The field line pitch in NSTX is approximately 5° in the toroidal direction, and can vary in the poloidal direction depending on the plasma shaping. The effective probe area is therefore the scalar product of the probe normal vector with the magnetic field tangent vector. Standard tokamak coordinates are used, with the components being (r,z,ϕ). The normal vector of a probe sitting on the 22° divertor floor is therefore a flat probe tip with a normal vector (0,1,0) rotationally transformed by 22° in the r,z plane.

The magnetic field tangent vector can then be determined from the magnetic equilibrium reconstruction as given by the EFIT code [79]. This code solves the Grad-Shafranov equation based on magnetic sensor data, and utilizes a bi-cubic interpolation to give the r,z,ϕ components of the magnetic field vector at any point in space within the torus. Since the probe positions are known, this value can be readily obtained. The scalar product of these two vectors is then taken, giving the effective normal probe fraction. Multiplying by the physical probe area then gives the effective area for use in the saturation current equation, yielding the plasma density.

Although the density is not used in any of the present calculations, the probes can be used to produce edge plasma densities for other studies. The important factors that contribute to the uncertainty in this measurement are the effective probe area, saturation cur-

rent, and electron temperature. The temperature and saturation current errors are discussed in Section 5.1.2, and the probe physical area uncertainty is discussed in 5.1.5. This leaves the contribution from the field line angle, which is primarily due to the toroidal field uncertainty. If the field angle contributes a factor of $1/\sin\theta$, to the overall measurement, the percent derivative contribution is $\cot\theta$. For a base angle of 5° and an uncertainty estimate of 1°, this contribution will be approximately 12%.

5.1.4 Particle flux

The ion saturation current represents the physical perpendicular current flow to the probe. While it is necessarily modified by the field angle from the net parallel flow in the SOL, it is sufficient in and of itself to determine the real particle flux to the surface, Γ. This quantity is of interest to the sheath heat flux as a necessary input, and can be determined directly from the ion saturation current. Beginning with the equation for saturation current:

$$I_{sat} = \frac{1}{2} n_0 e c_s A_{probe}, \quad I_{sat} = \Gamma e A_{probe} \tag{5.1}$$

$$\Gamma = \frac{I_{sat}}{e A_{probe}} \tag{5.2}$$

If we are interested in the measured flux at the probe tip, then the field angle is not necessarily relevant, as the physical probe area gives us the actual current and therefore flux to the probe. Simply dividing the current by the physical area and the electron charge yields the flux, in particles per square meter per second to the probe tip.

5.1.5 Error Analysis

To provide input into the sheath heat transmission equation, the uncertainties of both the electron temperature and particle flux must be quantified. Section 5.1.2 provides details on how the electron temperature is calculated, leaving the matter of error propagation in

the flux equation. The two uncertain quantities in this equation are the ion saturation current and the physical probe area. The ion saturation current uncertainty is also described in the section above, and the probe area uncertainty can be determined from the machine tolerances of the probe tips themselves. These are rated at $\pm 10^{-5} m$, quadratically propagating through the area of a rectangular face to give approximately a 5% uncertainty due to geometric effects.

5.2 Triple Probe Signal Analysis

The triple probe setup utilizes the same in-vessel hardware as the single probes, and so faces similar issues when trying to determine the actual values of derived quantities from the raw signals. Each electrode has an effective resistance that was measured at the time of installation, as well as contributions from the circuit itself. The main difference in interpretation and error analysis comes instead from combining signals from three electrode tips rather than a single probe, which introduces a larger degree of uncertainty into the data.

5.2.1 Circuit Contributions

The circuit contributions are handled in a similar manner to the single probe case, producing direct errors on the measured floating potential, voltage on one probe tip, and saturation current. The circuit resistor uncertainties present in the single probe setup also affect these results, introducing the approximately 3% uncertainty into each measurement. The circuit is configured with the same gain factors as in the single probes as well, so applying these various corrections and uncertainties can produce a measured probe voltage, floating potential, and saturation current. A similar low-pass filter is also applied, cutting off signals above 160 kHz. The dynamic range of the digitizer is again not a limiting factor.

5.2.2 Temperature, Density, Floating Potential and Saturation Current Determination

Although the acquisition hardware is more complicated for a triple probe, the analysis routines are much simpler as there is no curve fitting necessary. Equation (2.44) gives the electron temperature as a function of the bias voltage and the voltage on one of the probe tips. The floating potential can be directly determined from the signal on the tip which is dedicated to measuring it. The ion saturation current is determined by taking the maximum signal measured on the probe tip in the ion saturation region and subtracting the electron current contribution in that region. This contribution is generally negligible, but can become significant given a high enough electron temperature: some of the tail electrons can change the effectively measured maximum ion current. The density can be derived from the ion saturation current in the same manner as in the single-probe case, taking into account the magnetic field angle as well.

The raw signals from the various probe tips are shown in Figure 5.5, and the derived quantities are shown in Figure 5.6. These raw signals are stored in the MDSPlus data tree and the derived values are calculated via the analysis codes and stored in local data structures.

5.2.3 Signal Smoothing

Unlike the swept probes, which are able to provide parameter values at a maximum of twice per voltage sweep, the triple probes can provide values at each digitized time point. The effective frequency is therefore the Nyquist frequency or half of the digitization rate. Since the digitizer takes 250 kSamples/s, the effective maximum frequency of a triple-probe set is 125 kHz. Since plasma fluctuations and circuit noise can still cause variations over even this time period, the signals are smoothed using a median filter. The actual rate of smoothing is user-selectable, and in this study was chosen to have one triple-probe data

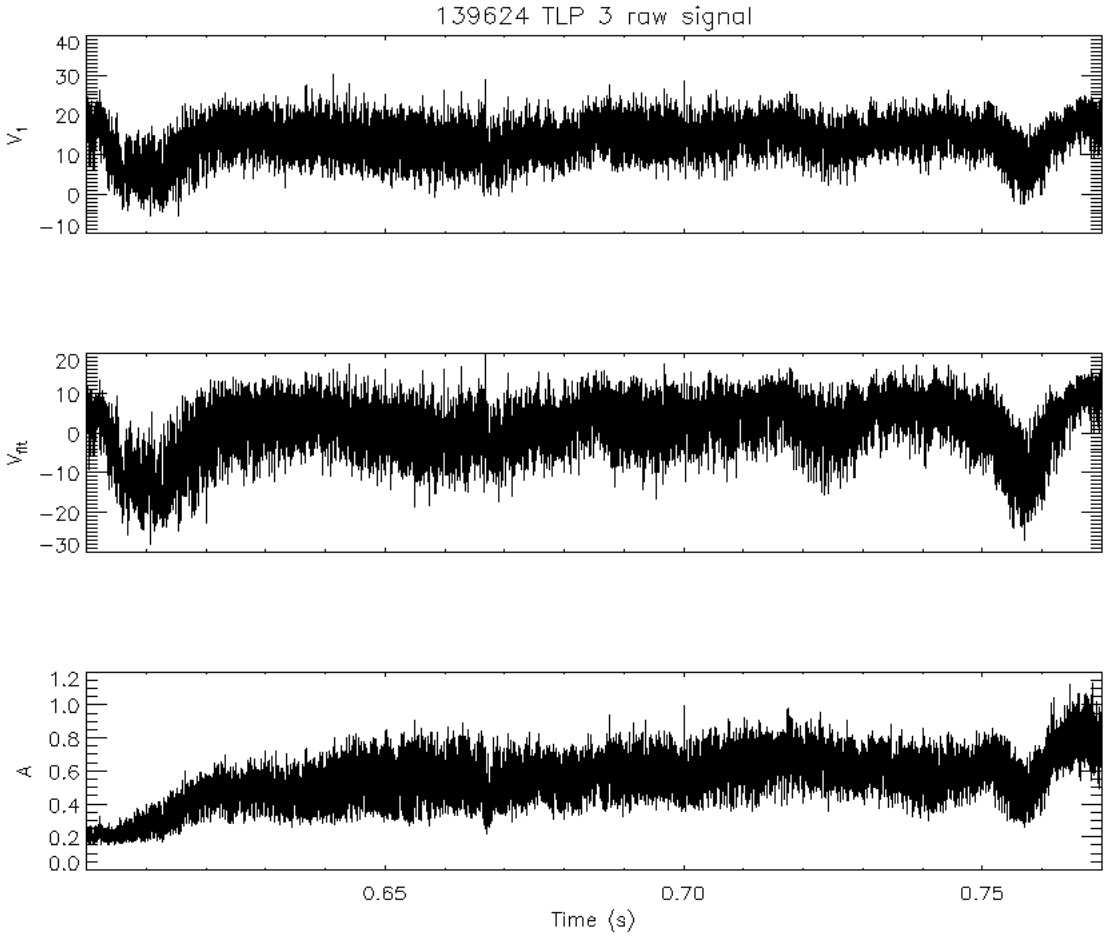

Figure 5.5: Raw triple probe signals from TLP 3 during 0.6-0.7s in 139624

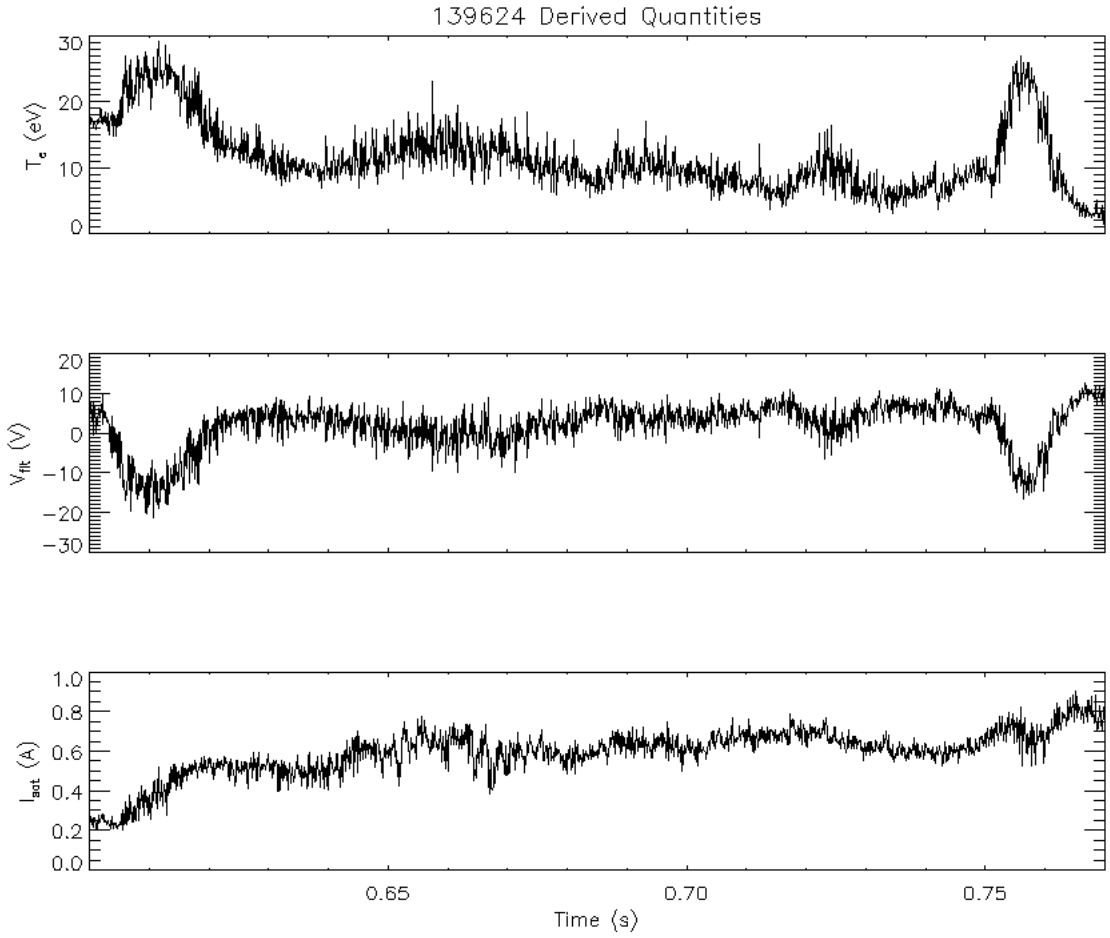

Figure 5.6: Derived signals from 139624 from 0.6-0.77s

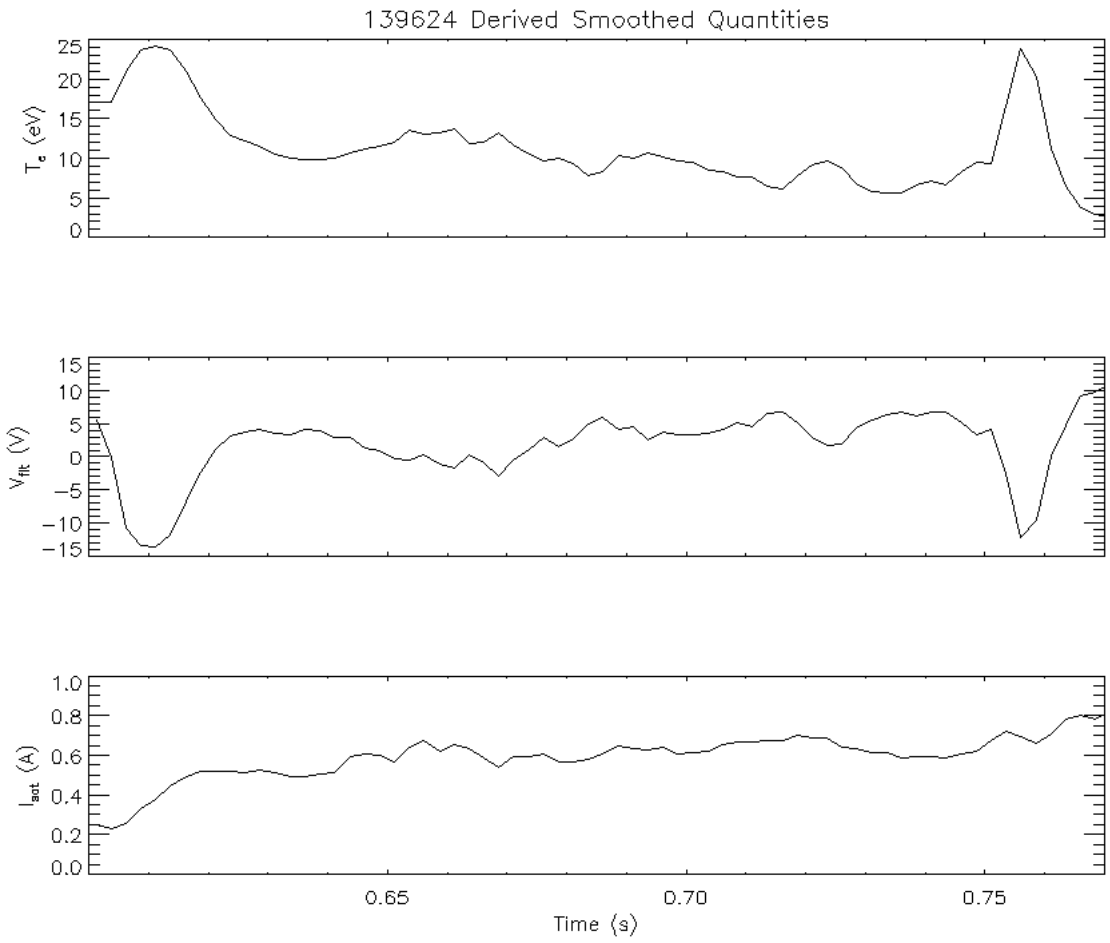

Figure 5.7: Smoothed TLP signals - 625 smoothed points per bin

point correspond roughly to one smoothed IR data point. This results in a median filtering of roughly 625 raw data points per final data point, resulting in 400 points/second. The signals from Figure 5.6 are shown with this median smoothing in Figure 5.7.

5.2.4 Error Analysis

Much of the error analysis applied to the triple probes has already been described in the single probe sections and circuit analysis section above. The additional contribution in this case is actually a reduction due to the smoothing described in the previous section. If 625 raw points are included for each derived point, then the uncertainty in each signal point is actually reduced to approximately 4% of its previous value. The systematic errors

are still included in the raw signals, but the combination of many data points allows for a greater degree of confidence in any individual signal. The two important quantities for this study are again electron temperature and particle flux. The former utilizes the circuit and measurement uncertainties, while the latter primarily depends on the saturation current uncertainties as well as the geometric area measurement uncertainties.

5.3 IR Data Analysis

The second component necessary for determining the sheath heat transmission is the direct heat flux measurement. In NSTX, this is obtained via a fast IR camera with a view of the divertor floor.

5.3.1 IR Camera Description

A detailed description of the IR camera hardware and theory can be found in [80], and only a brief overview will be given here. The camera itself is a Santa Barbara Focal Plane ImagIR fast camera [81], capable of operating from 1.6-6.3 kHz over the 1.5-11 μm range. An image depicting the field of view of the camera on the NSTX divertor floor can be seen in Figure 5.8. The camera system employs beam-splitting optics in order to produce two identical images on separate parts of the CCD in two different wavelengths. One signal is in the 7.2 μm band and the other is in the 5.0 μm band.

A temperature calibration was performed at several intervals during the NSTX run, utilizing the heated LLD plates. The ratio of the two different wavelength signals is mapped to the temperatures measured from thermocouples positioned in the LLD plates. The advantage of viewing the same region in two different wavelengths is that the emissivity term in the radiated power equation can be cancelled in the analysis (assuming that the emissivity does not change much with wavelength in this range). This is an important feature in the presence of lithium coatings, as the emissivity can be time-varying during a run day or even

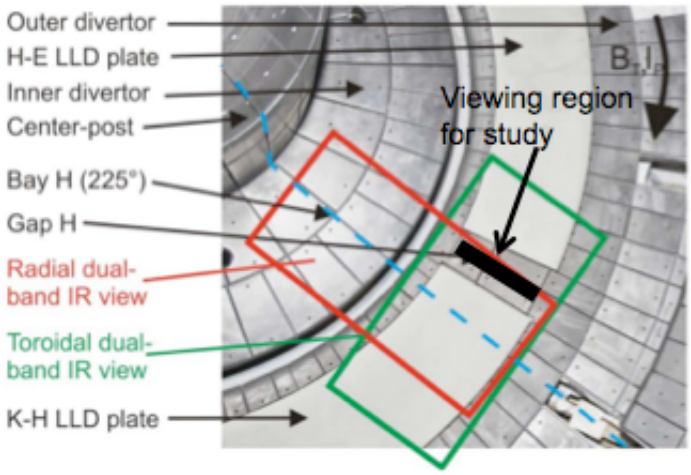

Figure 5.8: Image of NSTX divertor floor with IR camera viewing region highlighted, as well as region utilized in present study.

discharge as the impurity content or phase of the lithium surface changes. Along with the spatial calibration of the camera pixels to torus location, the camera is capable of producing a temperature reading for each camera frame - taken at 1.6 kHz. These temperature data then provide the input for a 2D heat conduction code to produce an inferred heat flux into the surface.

5.3.2 THEODOR and Heat Flux Determination

The raw temperature data are utilized as input into a 1D/2D heat conduction code, FURNACE [80], that models the surface as a thin film on a bulk thermal conductor. The code is based on a 1D model from Carslaw and Jaeger [82] and the THEODOR heat conduction code for tokamak surfaces [83]. This code therefore accounts for the thermal effect of the thin lithium film deposited on all NSTX plasma-facing surfaces. The 2D heat-conduction model then calculates the heat flux necessary to produce the observed temperature profile. An example temperature and temperature profile for an NSTX discharge can be seen in Figure 5.9. The IR data used in these analyses have been provided by A. McLean, and he has supplied an estimated uncertainty of 25% in the heat flux measurements [84]. This is the value that is used in the subsequent error propagation calculations in determining the

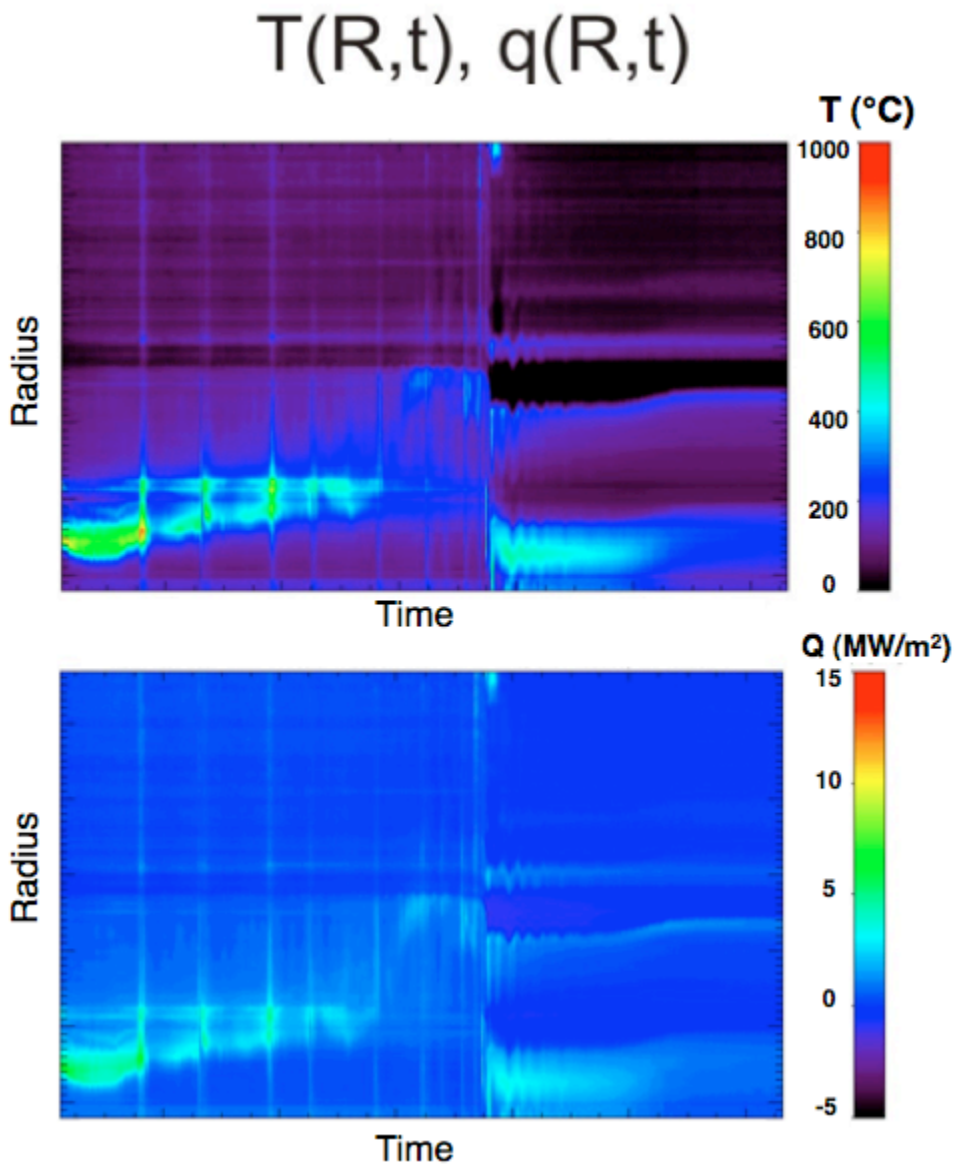

Figure 5.9: Sample temperature and heat flux profile produced from 2D IR data

final value of γ.

5.3.3 Signal Smoothing

Of concern to the present analysis is that fluctuations in the signals due to noise or turbulence may affect the results. Much like the Langmuir probe data, the IR camera data are smoothed temporally to reduce these effects. Five time points are combined into a single data point for use in the analysis. This corresponds to a 400 Hz signal, roughly on the same time scale with the triple probes, but still faster than the single probes. In the case of the triple probes, the nearest IR time point to a single triple probe time point is used for comparison. For the single probes, the IR data is further temporally averaged so that again the time bases match for ease of comparison.

Additionally, the IR camera pixel resolution is approximately 120 radial points by 70 toroidal points. The choice of toroidal central location is the center of a carbon tile, as seen in Figure 5.8. This location is utilized since the Langmuir probe array is also located on a carbon tile, as well as due to the fact that the THEODOR code is optimized for a thin film on a bulk thermal conductor, which the tile represents better than the multi-layered LLD. To further reduce uncertainties in measurements while still retaining confidence that the area surveyed is uniform, five toroidal points around and including the central pixel are averaged to produce a final result. The determination of the exact radial centroid is more complicated, relying on toroidal symmetry to assume that plasma conditions at one radial flux surface are the same at all toroidal locations in the device. The method for finding that surface is described in Section 5.4.1.

5.4 Experimental Derivation of γ

Knowing the heat flux, electron temperature, and particle flux provides all of the necessary variables to determine the sheath heat transmission coefficient. Since $q = \gamma k_B T_e \Gamma$, this can

be solved to give:

$$\gamma = \frac{q}{k_B T_e \Gamma} \tag{5.3}$$

The camera is measuring the perpendicular heat flux entering the surface rather than the parallel heat flux through the SOL, so the probe flux can be directly compared to the IR camera heat flux without taking into account the field angle. The temporal smoothing to match the signal time points is described in the sections above. Spatial calibration is also of paramount importance, and is discussed at length in the following section.

5.4.1 Flux Mapping

The assumption of toroidal axisymmetry allows for the comparison of data from two diagnostics in different toroidal locations. This is based on the idea that if both diagnostics are looking at the same plasma flux surface, then they will be sampling the same region. If the divertor geometry were truly toroidally uniform, then looking at two identical radial positions would imply that one is looking at identical plasma conditions. Due to the unique surface geometry of the LLD and the Langmuir probe array, this simple comparison is not possible. The main difference is that due to the 22° angle of the divertor floor and the height of the probe array, the radial position of points on the same flux surface will differ at a different toroidal location in the machine (i.e., at the probe array and IR viewing locations).

To compensate for the geometry variations, a method was developed to match the poloidal flux at a Langmuir probe with the same value along the chosen sightline of the camera. This is accomplished by having detailed knowledge of the surface topography of the divertor floor at both the probe array and IR camera toroidal locations. The EFIT equilibrium reconstruction code provides the capability to interpolate the poloidal flux at any r,z location in NSTX, and thus a method for matching flux space with real space.

The probes exist at fixed spatial positions and therefore the first step in the process is

to determine the flux at a probe position. A 2D r,z grid is then built over the IR camera viewing region with a 4.5mm resolution and the poloidal flux is calculated at each of these points. The point with the closest flux to the Langmuir probe location is selected and then the camera radial point (z coordinates for camera points are not contained in the camera data files) closest to this location is chosen as the comparison point for the γ analysis. As the plasma is constantly moving during the discharge, this process is carried out for each IR time point, before any smoothing takes place. An example of the signal overlay obtained by this method is shown in Figure 5.10.

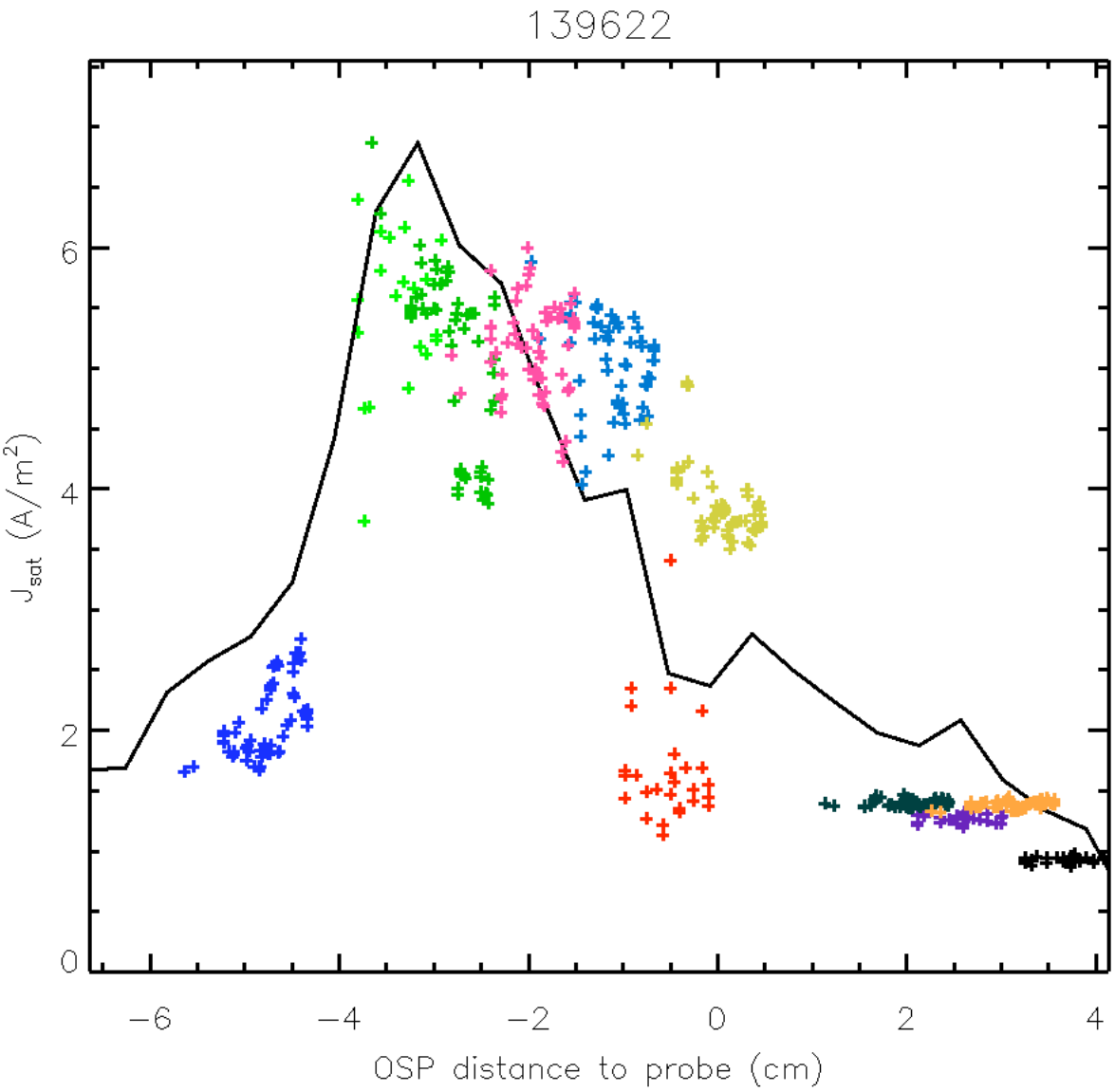

Figure 5.10: Overlay of probe signals and IR average trace from 0.65-0.79s in 139622

Chapter 6

Observed Value of Sheath Heat Transmission Coefficient

This chapter is concerned with the empirical determination of the sheath heat transmission coefficient, γ, in NSTX discharges. In order to obtain the most reliable comparison to the theoretical fluid picture of γ, a set of data selection criteria was implemented; these criteria are discussed in the first section. The second section is concerned with the comparison methods utilized to connect the IR and Langmuir probe data. The final section discusses the statistical analysis used to determine the measurement error on γ.

6.1 Data Selection Criteria

6.1.1 Quiescent Periods

The derivation of γ obtained in Section 2.5.2 is valid for a collisional fluid edge at equilibrium. As the NSTX SOL is subject to transient events such as edge localized modes, the use of quiescent time periods was a necessity for this study. A quiescent time period is defined as one where there are no variations in the saturation current that exceed ~100% of the signal. ELMs can typically produce variations in the signal of 200% or more, so this

filtering excludes such events. A deviation on a single probe is not necessarily an indication of an ELM as it can imply strike point movement over that probe, but variations across multiple probes typically indicate such an event. Figure 6.1 shows an ELM appearing in an NSTX discharge, here producing signal variations exceeding 300%.

6.1.2 Signal Strength

An additional criterion was that the probes and IR camera would see sufficient signal to assure a good signal/noise ratio. This effectively limits the available shots to those where the plasma outer strike point is placed directly on the probe array. Since we are interested in measuring γ in the SOL region, this means that the strike point needs to be ideally inboard of the probe array, or at worst on the inboard edge of it. This restricts the number of available discharges to essentially those that were run during the LLD experimental campaign, when most of the discharges were placed at that general radial location. This also restricts the time intervals within discharges that were used, as the strike point sweeps outboard at the beginning of the discharge before control algorithms keep it at a fixed radial location. The movement of the strike point in one such discharge can be seen in Figure 6.2. It should be noted, however, that the peak in particle flux is often found to be inboard of the calculated strike point from EFIT. The particle flux peak, along with the zero crossing of the floating potential, can be used to give the physical location of the strike point. It is therefore this physical location that is relevant when determining whether or not the strike point is located above the probe array. This is illustrated in Figures 6.3 and 6.4, which show the saturation and floating potential profiles, respectively. Here the first inboard zero crossing is used as the reference for the strike point location. Both figures show that the measured strike point should be approximately 3 cm inboard of the EFIT calculated strike point. Therefore one can effectively utilize discharges where the strike point as measured by EFIT is $\gtrsim 65cm$. Nevertheless, this still restricts the usable discharges to those that were intentionally run out on the LLD, which represent a small subset of total discharges run

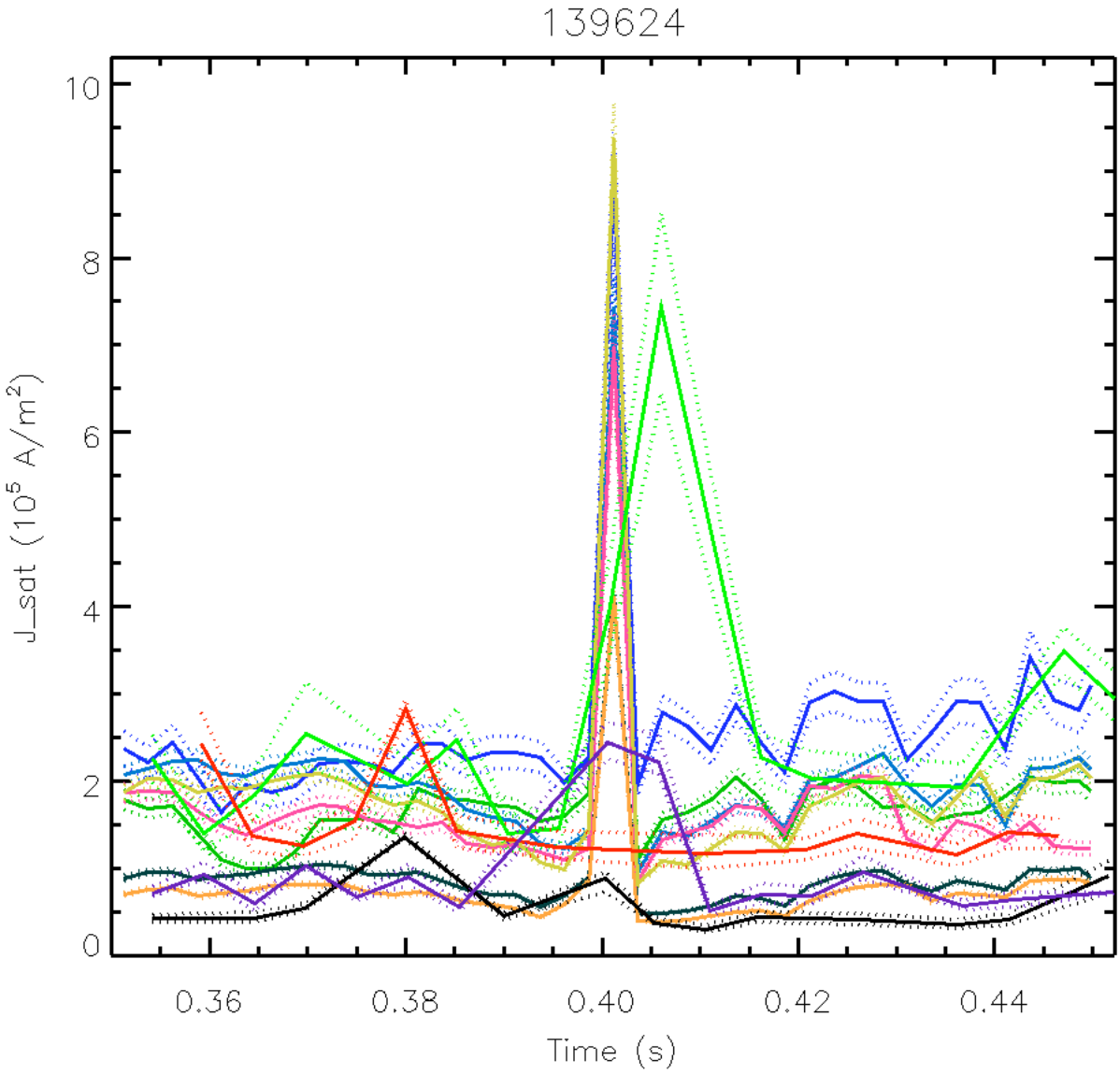

Figure 6.1: Appearance of an ELM on Langmuir probe data at approximately 0.4s

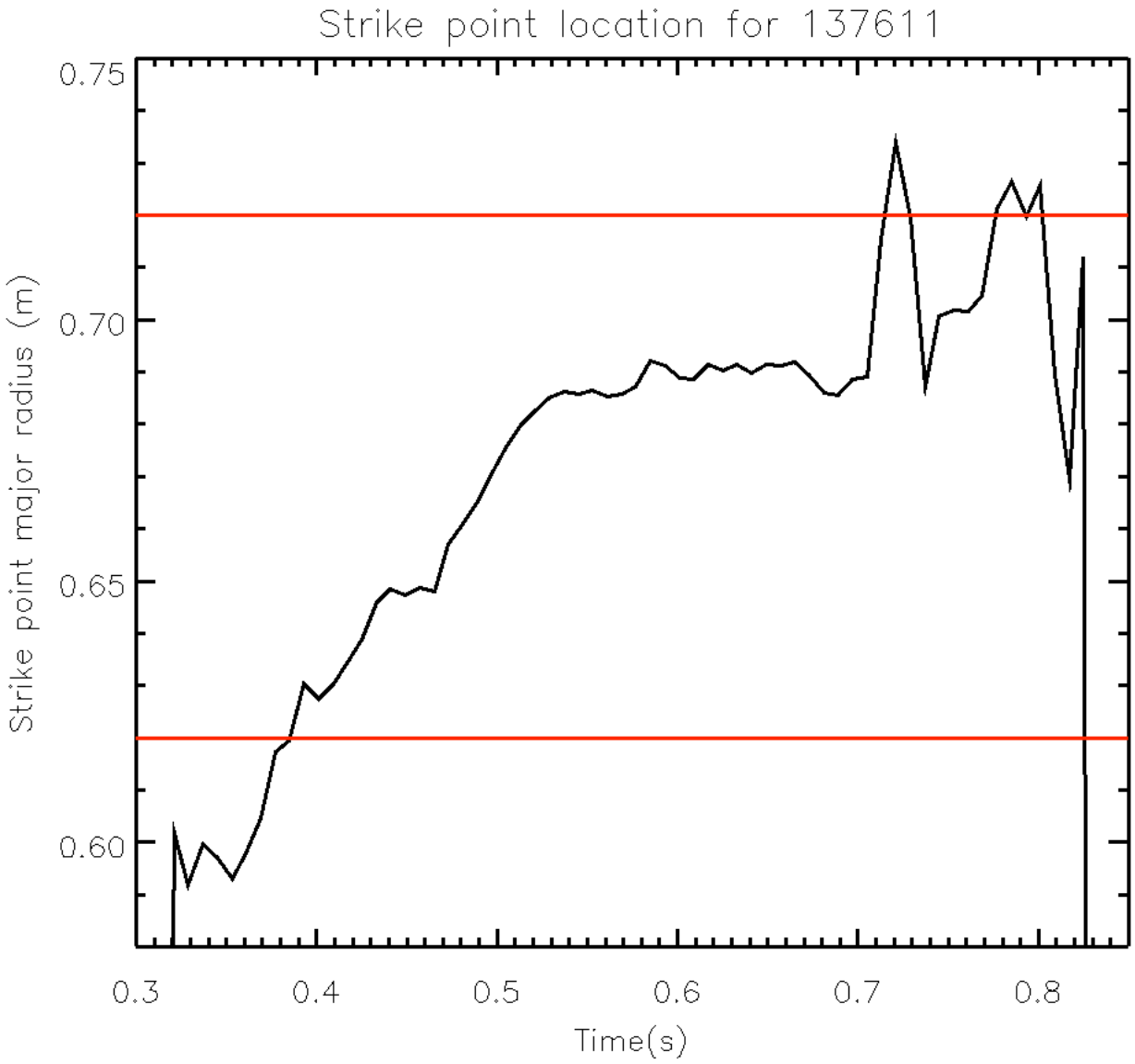

Figure 6.2: Strike point position evolution throughout NSTX discharge 137611 as calculated by EFIT02. The red lines show the radial extent of the Langmuir probe array.

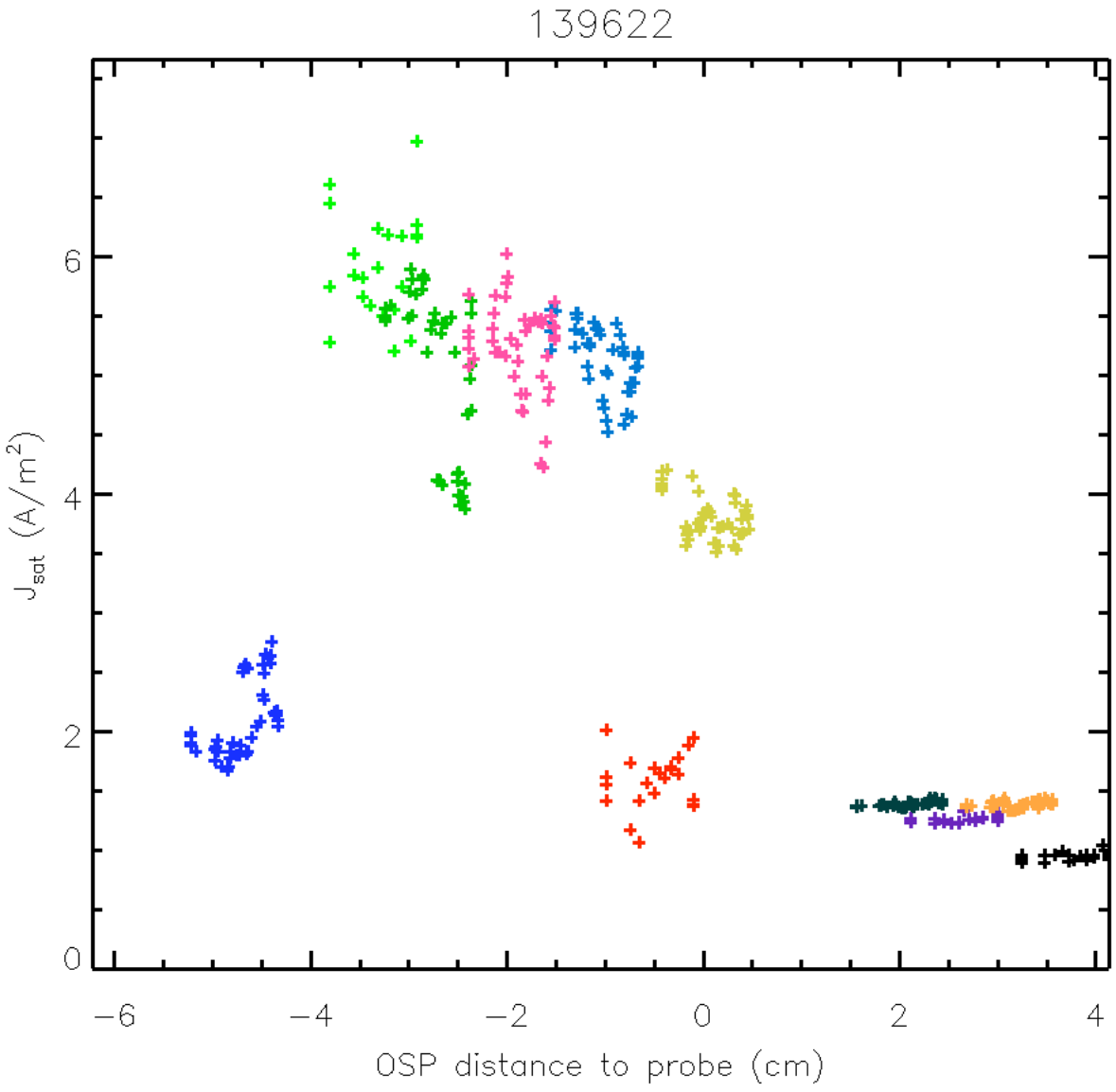

Figure 6.3: Langmuir probe saturation current profile for NSTX discharge 139622, plotted vs distance from EFIT02 strike point position.

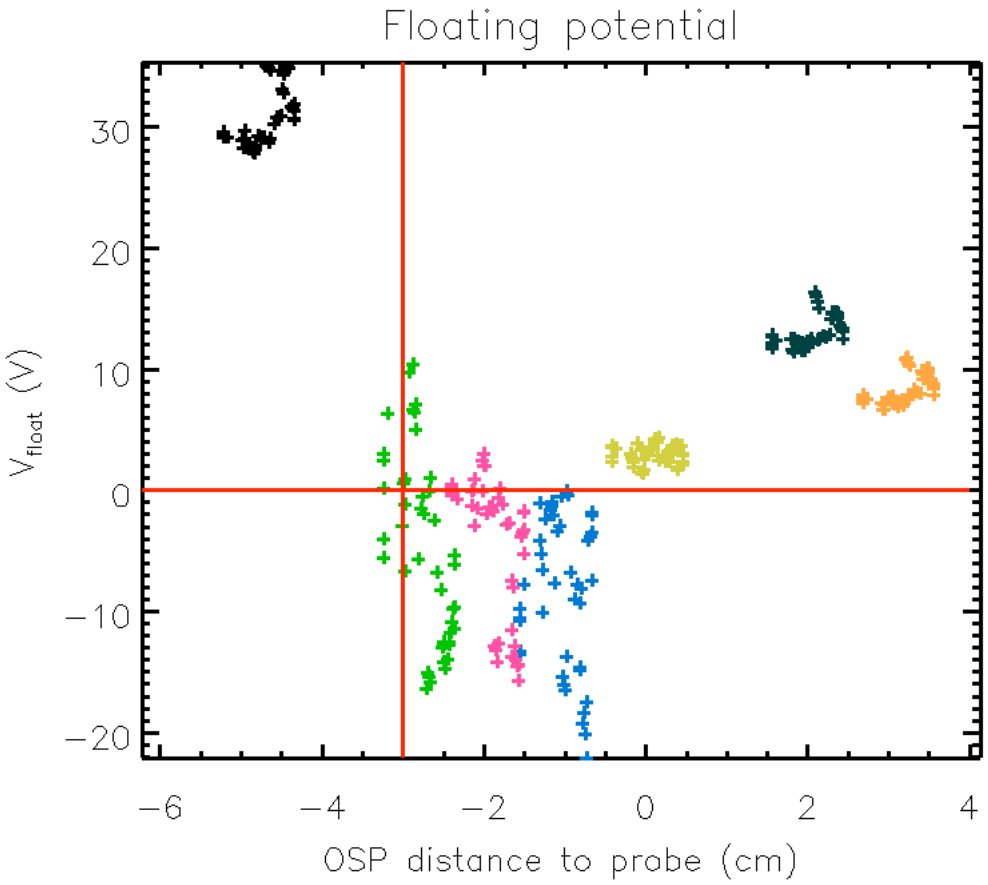

Figure 6.4: Floating potential profile for NSTX discharge 139622 with zero crossing shown

during the 2010 run campaign.

6.1.2.1 Floating Potential Criterion

The range of floating potential values chosen for this study is -7.5 and +7.5 V. Restricting the floating potential range for usable probe data can be considered a corollary to the signal strength criterion. As discussed above, the floating potential zero crossing is associated with the strike point position and location of maximum flux. This restriction therefore ensures a large signal will be present on the probes. In addition, the full derivation of γ given in Eq. 2.30 includes a contribution from V_f, which will necessarily be different for the different probe locations. A final benefit of this method is that by excluding large magnitude values of the floating potential, the probes can be directly compared without having to account for this additional quantity.

6.1.3 Probe Reliability/Intermittency

Although the probe array was engineering to minimize the deleterious effects of evaporated lithium on operation, the large amount of lithium evaporated throughout the FY10 NSTX run year still led to some arcing/intermittency issues in the measured probe data. These effects can manifest themselves as high or low variations in the measured saturation current, or large excursions in a single signal during a relatively quiescent period when corrected for strike point position. An example of a signal that was excluded from the analysis due to these concerns can be seen in Figure 6.5.

6.2 Comparison Methods

As mentioned in Section 5.3.3, the IR signal is temporally smoothed to match the time base of the Langmuir probe signal. This typically results in approximately 4 or 8 IR time points combined into one signal point for comparison with the probe signals, for triple and single

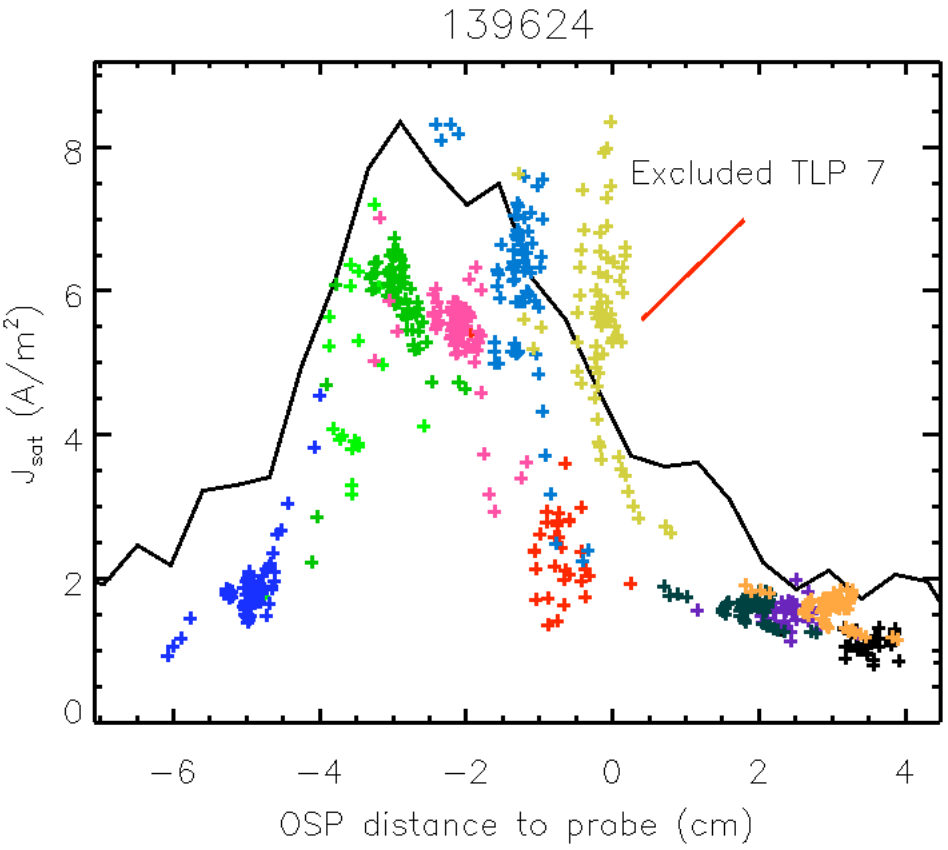

Figure 6.5: Plot of saturation current signals vs OSP radius showing intermittent signal marked for exclusion

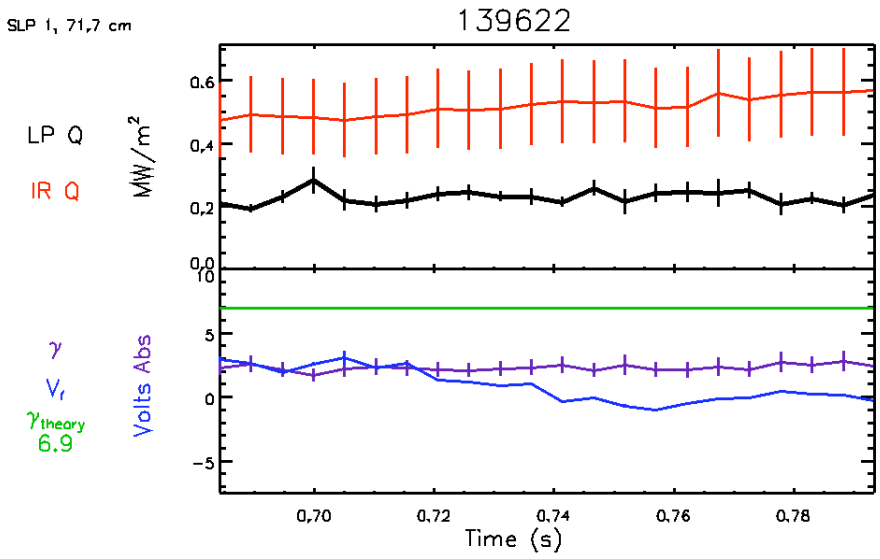

Figure 6.6: Comparison of probe heat flux to IR camera heat flux, with derived γ, V_f. Classical γ is included for reference

probes, respectively. The flux mapping is performed for each probe location at each time point to ensure matching of plasma parameters. Utilizing Equation 5.3, the empirical γ can be determined by taking the ratio of the smoothed, realigned IR and Langmuir probe signals at each of the corresponding time points. It is not necessary to account for the field angle in this case, as the camera is measuring the heat flux directed into the surface, much in the same way that the saturation current on the probes is measuring the perpendicular flux. The combined results plotted for a single probe during a quiescent time interval can be seen in Figure 6.6.

6.3 Statistical Analysis

The final stage in the analysis is the determination of the measurement uncertainty. Since γ is dependent on the ratio of the IR heat flux and the Langmuir probe temperature and flux, the measurement error can be derived from standard error propagation methods:

$$\delta\gamma = \sqrt{\left(\frac{\delta q}{k_B T_e \Gamma}\right)^2 + \left(\frac{\delta T_e}{k_B T_e^2 \Gamma}\right)^2 + \left(\frac{\delta \Gamma}{k_B T_e \Gamma^2}\right)^2} \tag{6.1}$$

Shot Number	Time Interval	Plasma Current (kA)	NB Power (MW)	LLD Bulk Temp (°C)
139622	0.68 - 0.79s	950	3	93
139624	0.60 - 0.77s	950	3	98
139625	0.66 - 0.78s	950	3	104

Table 6.1: Selected discharges and time periods aggregated for study

This then generates error bars for each single measurement of γ utilized in the study.

6.3.1 Shot Aggregation

The data selection criteria mentioned above served to limit the number of points utilized for the comparison, but also decreased the reliability of the measurement by decreasing the sample size. To remedy this issue, data from several shots with very similar plasma conditions (plasma shaping, neutral beam power, plasma current) were aggregated to increase the number of points of measurement of γ. The selected discharges and time periods for the first study are summarized in Table 6.1. Approximately 170 g of lithium had been deposited in the machine the previous week to facilitate LLD operation, bringing the total amount of lithium in the machine to 500 g. In the morning before these discharges were taken, 1.2 g of lithium had been deposited, and lithium deposition had ceased for the day four discharges prior to 139622. The decision to halt deposition was made due to the density depletion observed in prior discharges indicative, indicative of active lithium surfaces. The plots of some of the key waveforms in these discharges can be seen in Figure 6.7, which show them to be macroscopically very similar.

6.3.2 Gaussian Uncertainty

This whole process would naturally be made much simpler if one could assume that the measurement followed a Gaussian distribution. The uncertainty would then be simply related to the standard deviation of the measurement and the number of measurements. One method for determining graphically whether this is a viable assumption is the normal proba-

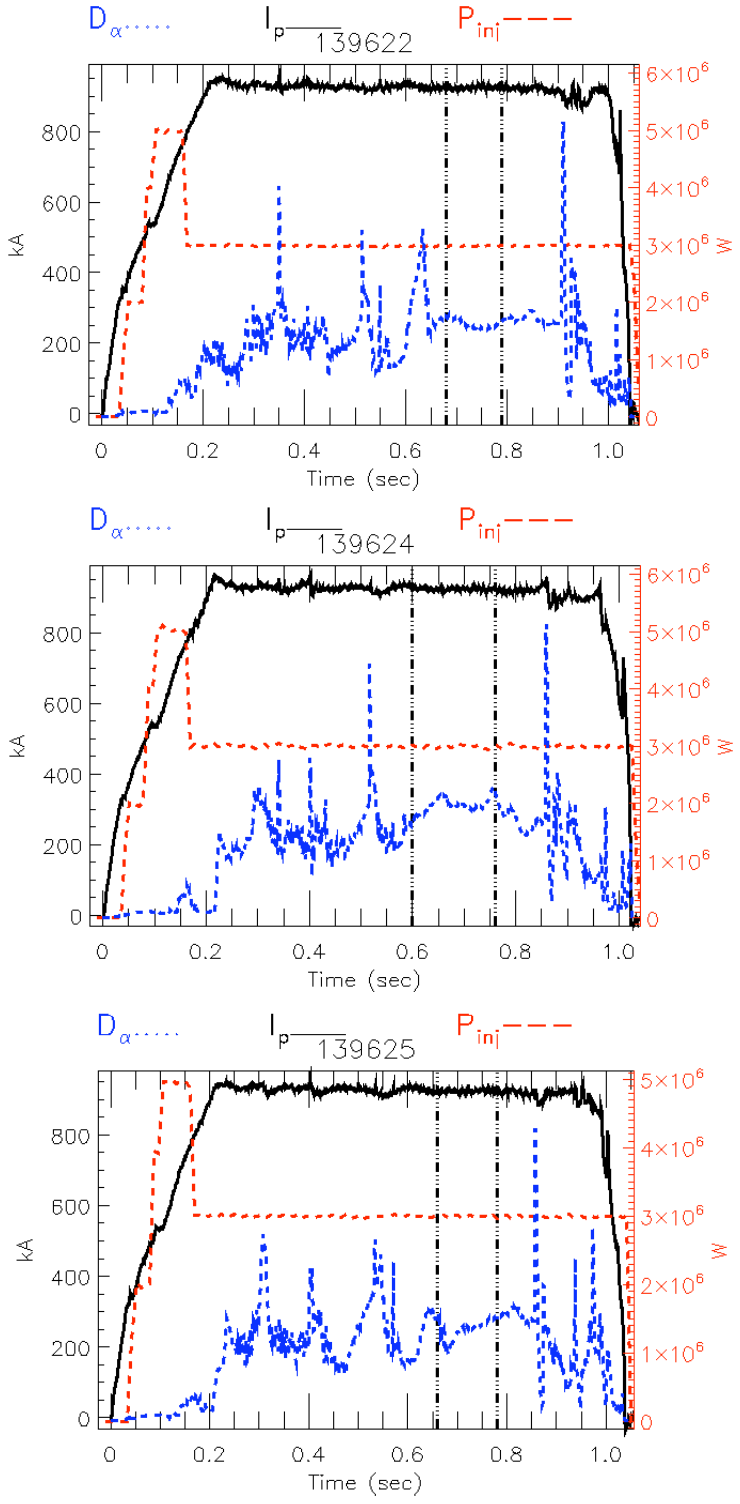

Figure 6.7: Summary plots of discharges used for study, showing identical plasma current and heading power, and similar ELM behavior over time of interest. Black vertical bars indicate time intervals used in analysis.

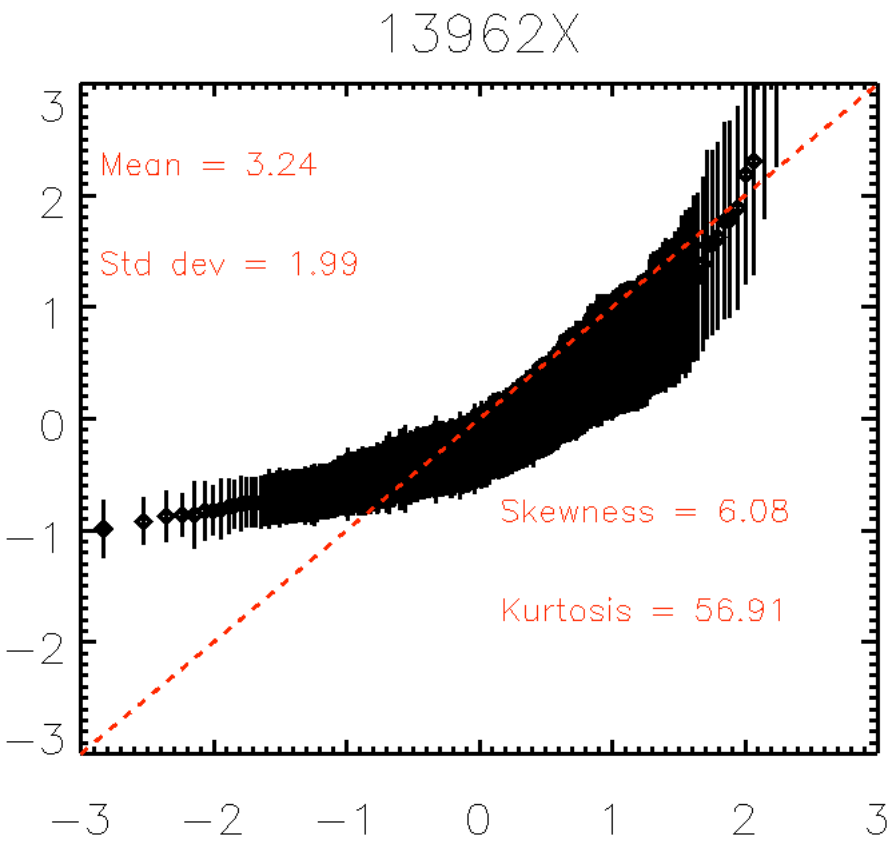

Figure 6.8: Normal probability plot for aggregate data series. Distribution is right-tailed with a leptokurtic (many values in tail) spread.

bility plot [85]. This is a method for plotting the ordered response values of a measurement vs. the normal order statistic medians. If the variable has a Gaussian response, the plot should be a straight line with a slope of one. This plot for the aggregate data is shown in Figure 6.8. This plot shows a significant deviation from purely Gaussian statistics, as is also evident in the histogram plot shown in Figure 6.9. Under this analysis, one obtains a value of 3.24 for γ with a standard deviation of 1.99. Given the deviations discussed above, this is unlikely to be the most accurate value for γ, necessitating a different approach.

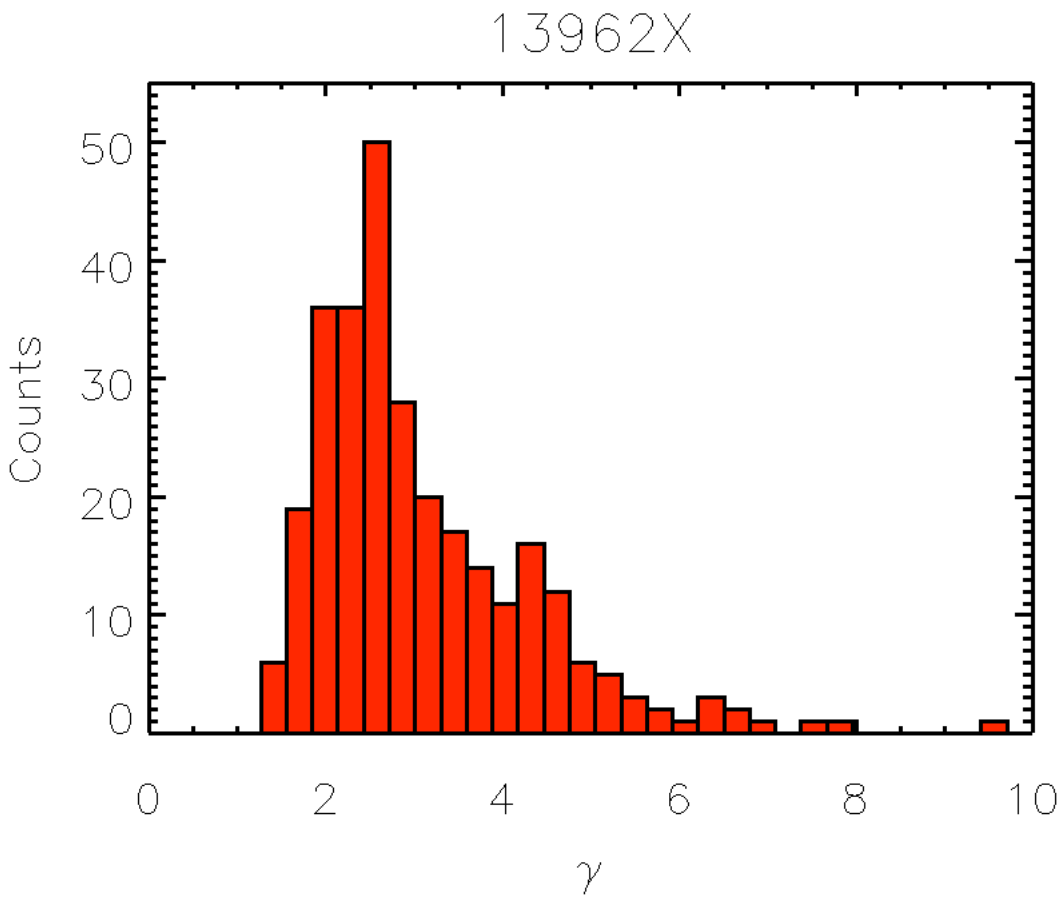

Figure 6.9: Histogram plot of aggregated γ

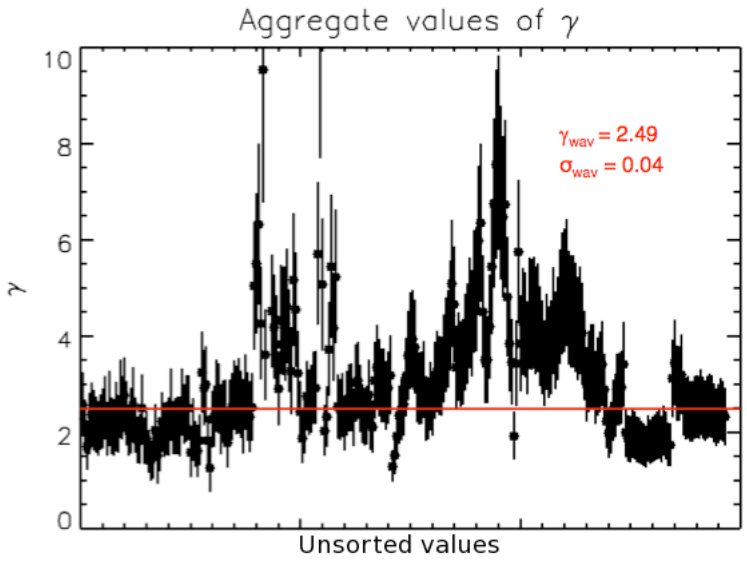

Figure 6.10: Aggregate unsorted data for γ showing error bars, weighted average, and measurement uncertainty

6.3.3 Weighted Average

The mean value of γ can still be determined if one adopts a weighted average model. The weighted average can be then be determined from the formula:

$$\gamma_{wav} = \frac{\sum w_i \gamma_i}{\sum w_i},$$

where w_i is defined as $1/(\delta\gamma_i)^2$. This weighting can then be used to determine the uncertainty in the measurement, using the formula:

$$\sigma_{wav} = \frac{1}{\sqrt{\sum w_i}}$$

Looking at the aggregate data from the shot series under this analysis, one obtains Figure 6.10. The weighed average value comes out close to 30% lower, at 2.49, with a weighted error of 0.04. This ultimately is much smaller than the classically derived coefficient of ~ 7, and this discrepancy is the focus of the final chapter.

Chapter 7

Conclusions and Discussion

7.1 Cross-device Comparison of Measured γ

As discussed in the final section of the last chapter, the measured value of γ is 2.49 ± 0.04, which places it well outside the classically expected value. The fact that many individually accurate measurements were combined leads to a result that deviates from the theoretical result in a statistically significant way. This lower measured value does is generally consistent with previous measurements of γ in other devices. Figure 7.1 shows a plot of obtained values from TCV using a similar method to this study. Data from DIII-D is shown in Figure 7.2, giving a sheath heat transmission factor of ~ 2. Since these results all deviate from the simple classical picture, further examination into the assumptions of this view are necessary.

7.2 Mitigating Factors on γ

As a reminder of our initial assumptions for γ, the simple classical equation is given again:

$$\gamma = 2.5\frac{T_i}{T_e} + \frac{2}{1-\delta_e} - 0.5\ln\left[\left(\frac{2\pi m_e}{m_i}\right)\left(1+\frac{T_i}{T_e}\right)\left(\frac{2}{(1-\delta_e)^2}\right)\right] \tag{7.1}$$

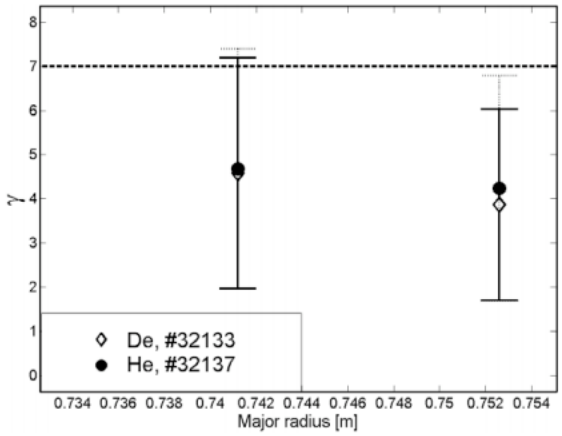

Figure 7.1: Profiles of γ across the outer target for matched D and He discharges ($\phi = 3°$). The horizontal dashed line denotes the expected value of γ (Eq. (2)) for the simplifying assumptions from Section 2. (Taken from Figure 3 in [10])

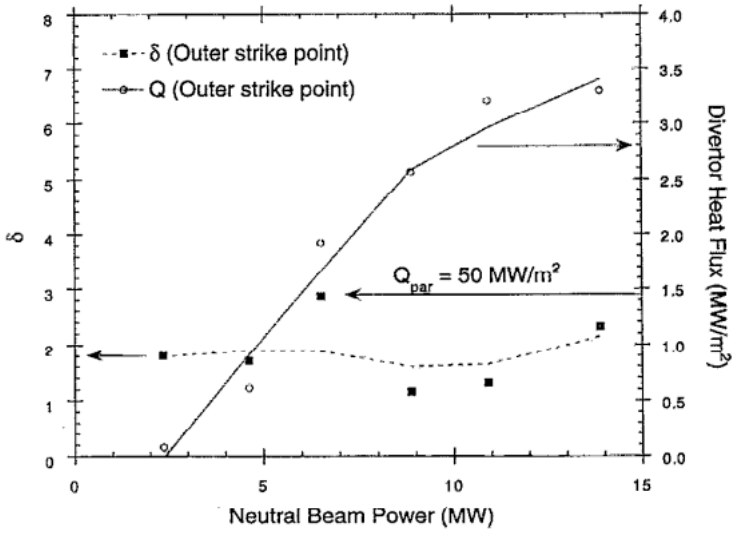

Figure 7.2: Dependence of the power flux to particle flux ratio (δ) and divertor power flux with input neutral beam power at the outer strike point. (Figure 1 in [11])

With $T_i = T_e$, $\delta_e = 0$, and $m_i = m_{Deuterium}$, the resultant value of γ is approximately 7. This section will examine these various assumptions and see if they contribute to the discrepancy.

7.2.1 Temperature Assumption

The assumption that $T_i = T_e$ could lead to artificially inflated values of γ if the ion temperature is indeed lower than the electron temperature. Since there are unfortunately no direct measurements of divertor ion temperature, a solution of Eq. 7.1 was performed with the respect to the temperature ratio. Taking $\gamma = 2.5$ from the experimental result, one solve for $x = \frac{T_i}{T_e}$ in the following manner (with $\delta_e = 0$ and $m_e/m_i = 2.72x10^{-4}$):

$$2*(2.5) - 4 + \ln\left(4\pi * 2.72x10^{-4}\right) = 5x - \ln(1+x) \tag{7.2}$$

$$5 - 4 - 5.68 = 5x - \ln(1+x) \tag{7.3}$$

$$e^{-4.68} = \frac{e^{5x}}{1+x}, \quad 0.009 = \frac{e^{5x}}{1+x} \tag{7.4}$$

This equation, when solved numerically, gives negative values of x, which we know to be unphysical. Assuming a more conservative value of γ, e.g., a Gaussian average of 3.5, still gives negative values. Even eliminating the ions altogether from the equation, e.g., that $T_i = 0$, does not produce a value of γ low enough to match the experimental results.

7.2.2 Secondary Electron Emission

We can perform another analysis in the same fashion, this time keeping $T_i = T_e$ fixed and now altering the secondary electron emission coefficient. This will serve to drive up γ in the electron flux term, but drive it down in the potential term. Solving for $x = 1 - \delta_e$ yields:

$$0.289 = e^{\frac{1}{x}}\sqrt{x} \tag{7.5}$$

Again, to get a sufficiently small value for the left hand side requires a negative value of x, which could not be possible for a real result of the square root, but also unrealistic in assuming a secondary electron emission coefficient of greater than 1.

7.2.3 Mass ratio

This term can be dealt with fairly simply, given that a smaller mass ratio (i.e., the presence of higher mass impurities) would serve to make the argument of the natural log term even smaller, resulting in even higher values of γ. The final term in 7.1 increases proportionately to

$$-0.5\ln\frac{m_e}{m_i}, \tag{7.6}$$

so an increased ion mass, e.g., with singly ionized impurities, results in a more negative natural log and a greater additive term to γ. Therefore, impurities cannot be contributing to a decreased value.

7.3 Reflection Effects

There is one term that can contribute significantly to the classical picture of γ, and has heretofore been ignored in the present analysis: the reflection coefficient. This quantity is different than the recycling coefficient in the sense that cold neutrals recycled from the wall are not carrying much in the way of energy with them. Hot ions and electrons, directly reflected from the wall, can indeed substantially reduce the net power flux that the surface experiences. These terms come into the equation in this manner:

$$\gamma = 2.5\frac{T_i}{T_e}(1-R_i)+\frac{2}{1-\delta_e}(1-R_e)-0.5\ln\left[\left(2\pi\frac{m_e}{m_i}\right)\left(1+\frac{T_i}{T_e}\right)\left(\frac{2}{(1-\delta_e)^2}\right)\right] \tag{7.7}$$

where R_i, R_e represent the ion and electron reflection coefficients, respectively. These coefficients have been calculated for deuterium on carbon at various energies [12], also taking

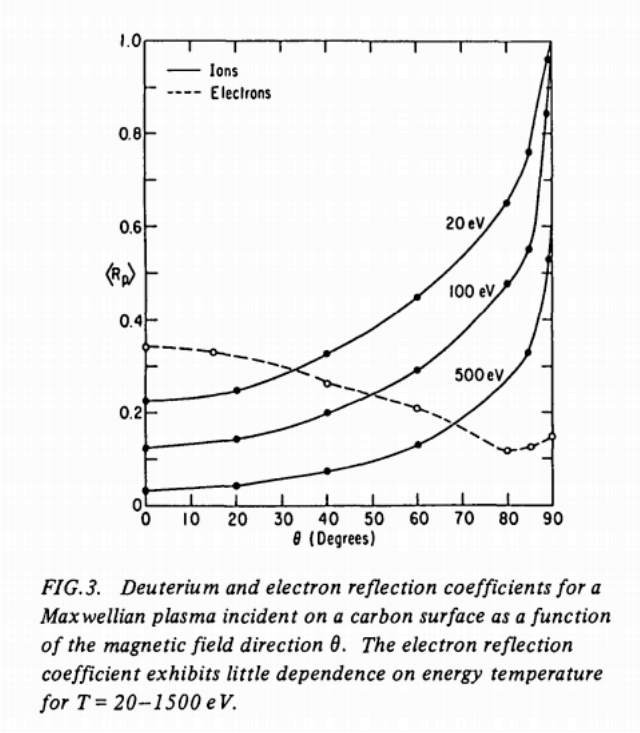

FIG. 3. Deuterium and electron reflection coefficients for a Maxwellian plasma incident on a carbon surface as a function of the magnetic field direction θ. The electron reflection coefficient exhibits little dependence on energy temperature for T = 20–1500 eV.

Figure 7.3: Reproduction of Figure 3 from [12], showing energy reflection coefficients for particles incident on carbon as a function of angle

into account the effect of field angle. The closer the angle is to parallel incidence, the more single scattering events become important, causing this reflection factor to increase greatly. The angular and energy dependence of these coefficients can be seen in Figure 7.3 . Using a field angle of $85^{\diamond}$ (from the normal) and $T_i = T_e = 20eV$ yields a value of approximate 0.1 for electrons and 0.8 for ions. This reduces the theoretical value of γ to approximately 4.8, still not enough to match the experimental result. Recent work by Qiu and Ruzic has examined the reflection coefficients for deuterium incident on lithium surfaces [86]. These results show that the reflection coefficient for lithium is generally lower than that for carbon, indicating that highly lithiated surfaces such as those present in NSTX should suffer fewer direct reflections than carbon surfaces, further reducing the significance of this effect.

7.4 Electron/Ion Distribution

7.4.1 Collisionality Assumptions

This derivation of γ comes from a fluid picture of the plasma edge at thermodynamic equilibrium. Changes to the edge conditions due to lithium surface coatings can cause reductions in the collisionality by lowering the edge density or increasing the edge temperature. A more in-depth examination of edge collisionality regimes is given in Section 2.3 - this section will discuss the implications of those regimes.

As previously discussed, the important relationship is the ratio of the mean free path to the scale length of the SOL, or $\nu^* = L/\lambda_{ee}$. If this number is large, then electrons can undergo several collisions before impacting the divertor target, resulting in a thermal distribution. If the electron and ion temperatures are the same, then this result holds for the ion distribution as well. A smaller value of ν^* leads to fewer (or perhaps no collisions) in the SOL, leaving the distribution essentially identical to that of the particles escaping core confinement. Assuming that the distribution in the core is thermalized means that this may not be a large issue. An important caveat exists, however, if only the most energetic electrons are able to overcome the potential drop at the sheath, then this portion of the distribution will become selectively depleted and not replenished due to collision-induced thermalization. If this electron term is indeed reduced (as can be seen in earlier kinetic studies with departures from Maxwellian distributions [87]) , then its overall contribution, i.e, the logarithmic term in the equation for γ, will be greatly diminished, possibly accounting for the smaller observed value.

This has the potential to be an important effect, even more so with the use of lithium in NSTX plasmas. If indeed in these discharges lithium coatings were altering the SOL collisionality, it would be reducing it and moving the discharge toward a sheath-limited regime, as lithium has been shown to increase edge temperature while decreasing edge density, lowering the value of ν^*. The density and temperature values involved in this calculation

are the upstream values (at the mid-plane). The NSTX Thomson scattering diagnostic does provide some sight lines in the SOL region, which can be used for comparison. Examining discharge 139624 (which has an edge q of 10 and a radius of approximately 146 cm at the mid-plane SOL), and using the upstream density of $3x10^{18}m^{-3}$:

$$\nu^* = 10^{-16}\pi Rq\frac{n}{T^2} = 10^{-16}\pi(1.5)*10*3x10^{18}/T^2 = 1.3x10^4/T^2$$

This result is heavily dependent on the upstream value of the temperature. The threshold value for placing $\nu^* \leq 10$ is $T \gtrsim 35eV$. The measured temperature from the Thomson scattering at 700 ms is 20 eV. This value is not sufficient to place to discharge solidly in the sheath-limited regime. However, the Langmuir probes at the strike point measure ~25 eV electron temperature at this time point. This discrepancy with the Thomson value could be due to the fact that the low density at the plasma edge can reduce the reliability of the upstream measurement, and precludes any definitive conclusion. Another possibility is to deduce the upstream temperature and density would be to use modeling to connect the target temperatures to the mid-plane results via the two point model. This method, however, requires knowledge of the SOL transport regime. A putative solution would be to conduct such modeling for both regimes and attempt to make a determination on which result is more reliable, but such an effort lies outside the scope of this thesis.

7.4.2 Empirically Derived Distribution

Analysis by M.A. Jaworski [88] on the NSTX dense Langmuir probe array has demonstrated the ability to directly extract the electron energy distribution function. Rather than using the standard Maxwellian analysis described in Chapter 2, this function can be integrated directly to provide a measure of the electron energy deposition on the target surface. This result would provide an explicit picture of the electron contribution to γ and would allow for a more accurate theoretical determination its value for comparison. Such work

is ongoing at the time, and when completed could provide a direct kinetic picture of the conditions at the divertor target.

7.5 Conclusions

A study was conducted in NSTX discharges with lithium coatings to determine the sheath heat transmission coefficient, γ. This research was enabled by the installation of new diagnostics to support the NSTX Liquid Lithium Divertor, namely a dense Langmuir probe array (Chapter 4) and a fast, dual-band IR camera (Chapter 5). A series of similar discharges with similar macroscopic properties taken during an LLD experimental campaign were used for comparison. Quiescent periods in these discharges were taken for comparison, and the ratio of the heat flux data from the probes and IR camera was taken.

This empirical value for γ has been derived to be 2.49 ± 0.04, significantly below the classical value of 7. The earlier sections of this chapter explore some possible mitigating factors that could drive down the classical value to the observed result. None of these factors, however, is enough to explain the value measured. This lends credence to the notion that the collisionality effects at the very least need a thorough treatment in a model that does not make inherent assumptions about the ion and electron distributions.

7.6 Future Work

The classical equation for γ contains several contributing terms that are necessary to explore empirically in order to compare with the present result. These include the ion temperature, secondary electron emission, and impurity distribution of the edge plasma. If these values are known, then a more accurate theoretical value of γ can be obtained. If the results match a lower value as obtained in this study, then the classical result can be confirmed. If this value proves to match the classical result, then there are two possibilities: the present study may need to be re-evaluated or a different analysis of the formula for γ may be necessary.

The acquisition of more accurate midplane temperature and density data would also allow for a comparison of target and midplane temperature and density values. This would allow for a different method of assessing the SOL heat transport regime and provide a means for determining the accuracy of the models for extrapolating midplane temperature and density profiles from the divertor target values and vice versa. The high number of spatial data points from the Langmuir probe array could provide a high degree of confidence for comparison with midplane values. Depending on what relationship these two-point comparisons follow, the heat transport regime could then be inferred.

A priori, the effect of lithium PFC coatings should be to lower the edge density and raise the edge temperature. If this were to occur, the edge collisionality would decrease. This could cause the plasma to transition to a sheath-limited rather than collisional regime. The tail of the electron distribution extracted by a material surface would then not be collisionally replenished. Since these electrons are the only ones with energies sufficient to exceed the plasma-wall potential difference, they would no longer be able to carry a large fraction of the heat out of the plasma and be a large contributor to the value of γ. Should such a condition exist, the value of γ measured would be consistent with these effects.

In the discharges examined, the quiescent time periods chosen were late in the discharge, occurring after sufficient time to allow the depletion of the high energy portion of the electron population. If more quiescent plasma conditions could be obtained early in the discharge, a measurement of the evolution (or lack thereof) of γ could lend support to this hypothesis. These results also suggest a series of experiments with varying lithium coatings and fueling profiles to ensure that the SOL transport is in either the sheath-limited or conduction-limited regime. Such a study would enable an explicit determination of regime transition as a function of target density and temperature, as well as the different values of γ that may result as the transition is achieved.

Appendix A

Probe Array Positions and Circuitry

The position of each probe tip, as well as the resistance from probe tip to feedthrough exit, can be found in Tables A.1-3. The circuit diagrams for the swept probe bias and acquisition electronics can be found in Figures A.1-2. The circuit diagrams for the triple probe bias and acquisition electronics can be found in Figures A.3-4. The patch panel used to assign electrodes to different probe circuitry can be found in Figure A.5.

Probe	R (cm)	Z (cm)	ϕ (deg)	Row	Resistance (Ω)
1	62.69	-159.50	53.61	1	10
2	62.69	-159.50	54.22	1	20
3	62.69	-159.50	54.83	1	10
4	62.97	-159.39	53.61	2	4
5	62.97	-159.39	54.22	2	50
6	62.97	-159.39	54.83	2	4
7	63.25	-159.28	53.61	3	4
8	63.25	-159.28	54.22	3	6.5
9	63.25	-159.28	54.83	3	2.3
10	63.54	-159.17	53.61	4	5
11	63.54	-159.17	54.22	4	4
12	63.54	-159.17	54.83	4	10
13	63.82	-159.06	53.61	5	4
14	63.82	-159.06	54.22	5	3
15	63.82	-159.06	54.83	5	2
16	64.10	-158.95	53.61	6	3
17	64.10	-158.95	54.22	6	5
18	64.10	-158.95	54.83	6	3
19	64.38	-158.84	53.61	7	3
20	64.38	-158.84	54.22	7	3.3
21	64.38	-158.84	54.83	7	5
22	64.67	-158.73	53.61	8	2
23	64.67	-158.73	54.22	8	3.5
24	64.67	-158.73	54.83	8	4
25	64.95	-158.62	53.61	9	3
26	64.95	-158.62	54.22	9	7
27	64.95	-158.62	54.83	9	2.7
28	65.23	-158.51	53.61	10	3
29	65.23	-158.51	54.22	10	10
30	65.23	-158.51	54.83	10	30
31	65.51	-158.40	53.61	11	22
32	65.51	-158.40	54.22	11	15
33	65.51	-158.40	54.83	11	5

Table A.1: Probe locations and resistances (Probes 1-33)

Probe	R (cm)	Z (cm)	ϕ (deg)	Row	Resistance (Ω)
34	65.79	-158.29	53.61	12	6.8
35	65.79	-158.29	54.22	12	3.5
36	65.79	-158.29	54.83	12	2.5
37	66.08	-158.18	53.61	13	2.1
38	66.08	-158.18	54.22	13	4
39	66.08	-158.18	54.83	13	30
40	66.36	-158.06	53.61	14	2
41	66.36	-158.06	54.22	14	2
42	66.36	-158.06	54.83	14	30
43	66.64	-157.95	53.61	15	2.5
44	66.64	-157.95	54.22	15	2.5
45	66.64	-157.95	54.83	15	6
46	66.92	-157.84	53.61	16	9
47	66.92	-157.84	54.22	16	8
48	66.92	-157.84	54.83	16	3
49	67.20	-157.73	53.61	17	7
50	67.20	-157.73	54.22	17	3
51	67.20	-157.73	54.83	17	7
52	67.49	-157.62	53.61	18	6
53	67.49	-157.62	54.22	18	5
54	67.49	-157.62	54.83	18	6
55	67.77	-157.51	53.61	19	1.5
56	67.77	-157.51	54.22	19	10
57	67.77	-157.51	54.83	19	1.7
58	68.05	-157.40	53.61	20	3
59	68.05	-157.40	54.22	20	3.3
60	68.05	-157.40	54.83	20	2
61	68.33	-157.29	53.61	21	2
62	68.33	-157.29	54.22	21	2
63	68.33	-157.29	54.83	21	2
64	68.62	-157.18	53.61	22	6
65	68.62	-157.18	54.22	22	8
66	68.62	-157.18	54.83	22	2

Table A.2: Probe locations and resistances (Probes 34-66)

Probe	R (cm)	Z (cm)	ϕ (deg)	Row	Resistance (Ω)
67	68.90	-157.07	53.61	23	3
68	68.90	-157.07	54.22	23	2.7
69	68.90	-157.07	54.83	23	5
70	69.18	-156.96	53.61	24	6
71	69.18	-156.96	54.22	24	4
72	69.18	-156.96	54.83	24	3.4
73	69.46	-156.85	53.61	25	3.2
74	69.46	-156.85	54.22	25	3.4
75	69.46	-156.85	54.83	25	1.5
76	69.74	-156.74	53.61	26	2.2
77	69.74	-156.74	54.22	26	4
78	69.74	-156.74	54.83	26	1.9
79	70.03	-156.63	53.61	27	1.8
80	70.03	-156.63	54.22	27	13
81	70.03	-156.63	54.83	27	1.8
82	70.31	-156.52	53.61	28	2.5
83	70.31	-156.52	54.22	28	3
84	70.31	-156.52	54.83	28	2.5
85	70.59	-156.41	53.61	29	5
86	70.59	-156.41	54.22	29	4
87	70.59	-156.41	54.83	29	5
88	70.87	-156.30	53.61	30	50
89	70.87	-156.30	54.22	30	1.8
90	70.87	-156.30	54.83	30	11
91	71.15	-156.19	53.61	31	3.2
92	71.15	-156.19	54.22	31	2.8
93	71.15	-156.19	54.83	31	3.3
94	71.44	-156.08	53.61	32	8.8
95	71.44	-156.08	54.22	32	2.7
96	71.44	-156.08	54.83	32	1.8
97	71.72	-155.97	53.61	33	2.5
98	71.72	-155.97	54.22	33	4.1
99	71.72	-155.97	54.83	33	9

Table A.3: Probe locations and resistances (Probes 67-99)

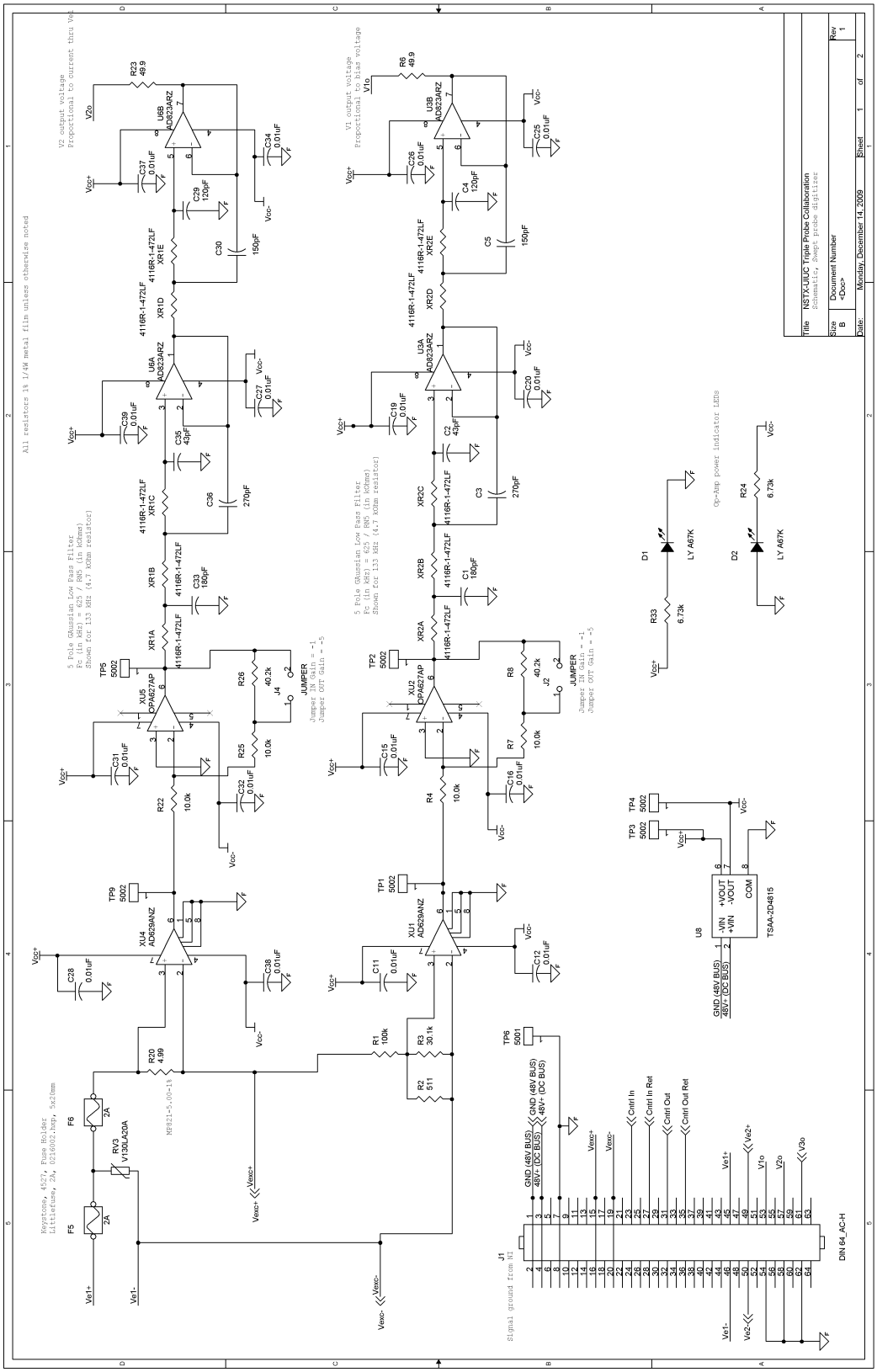

Figure A.1: Swept probe bias/acquisition electronics I

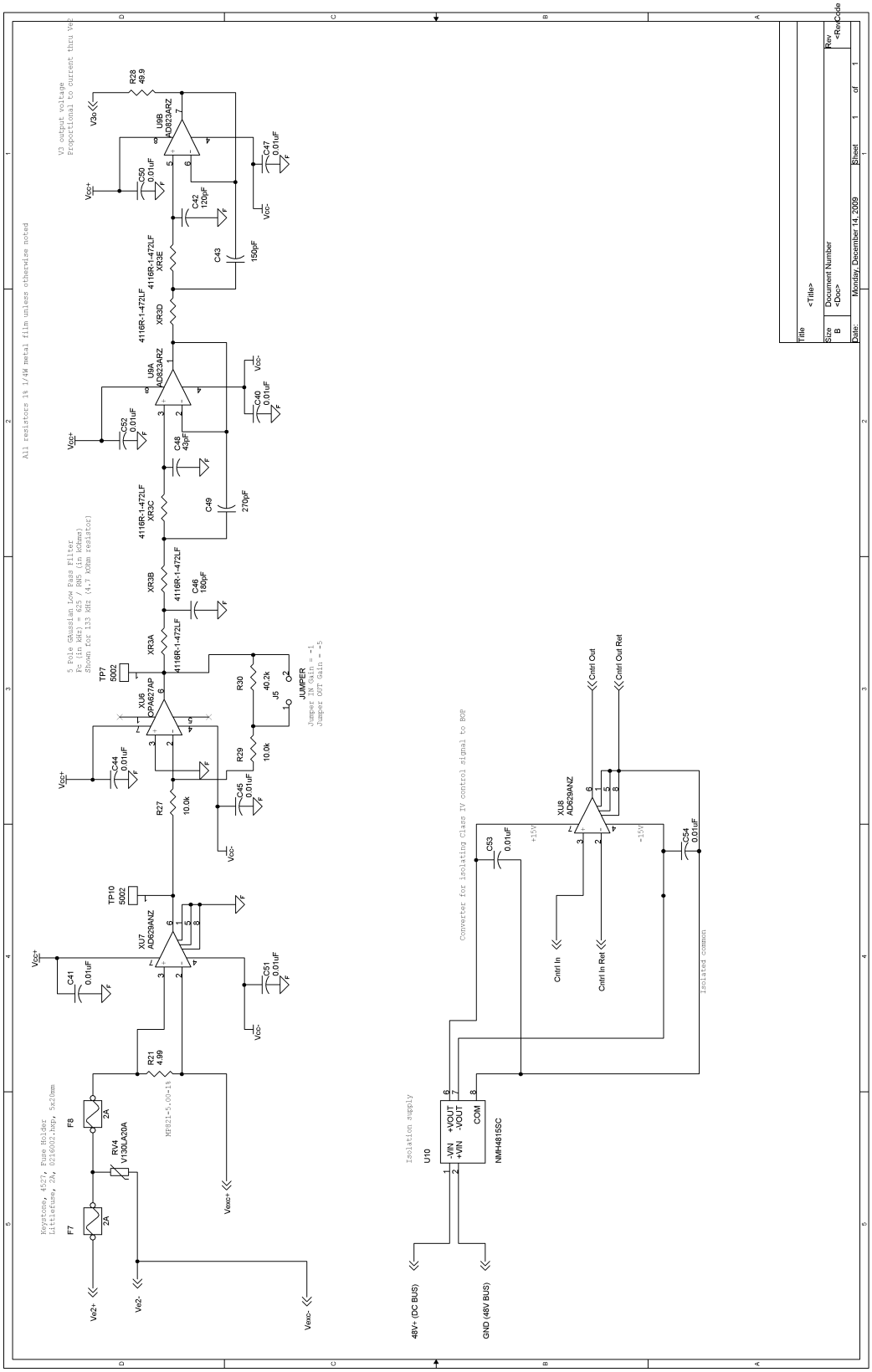

Figure A.2: Swept probe bias/acquisition electronics II

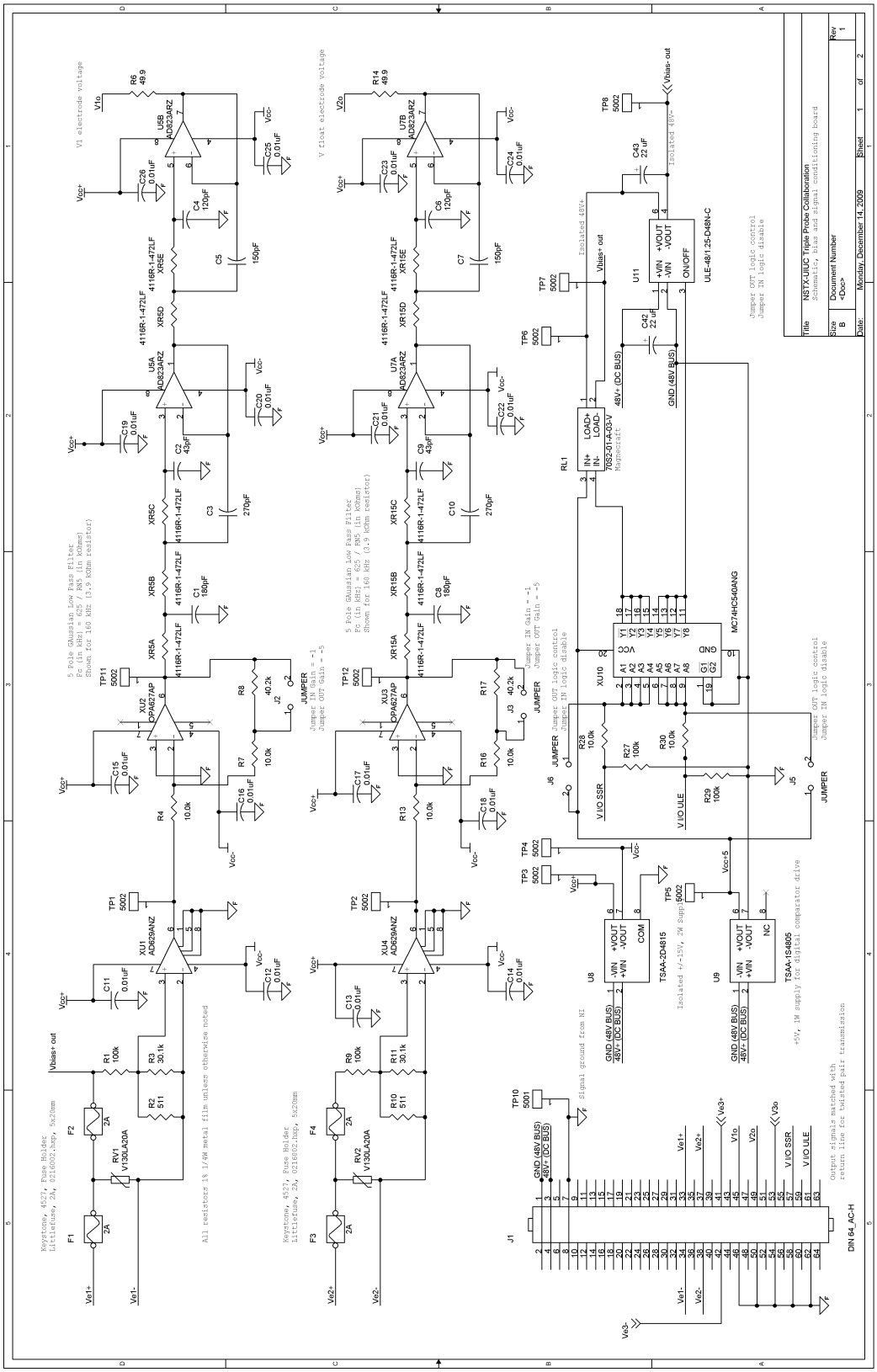

Figure A.3: Triple probe bias/acquisition electronics I

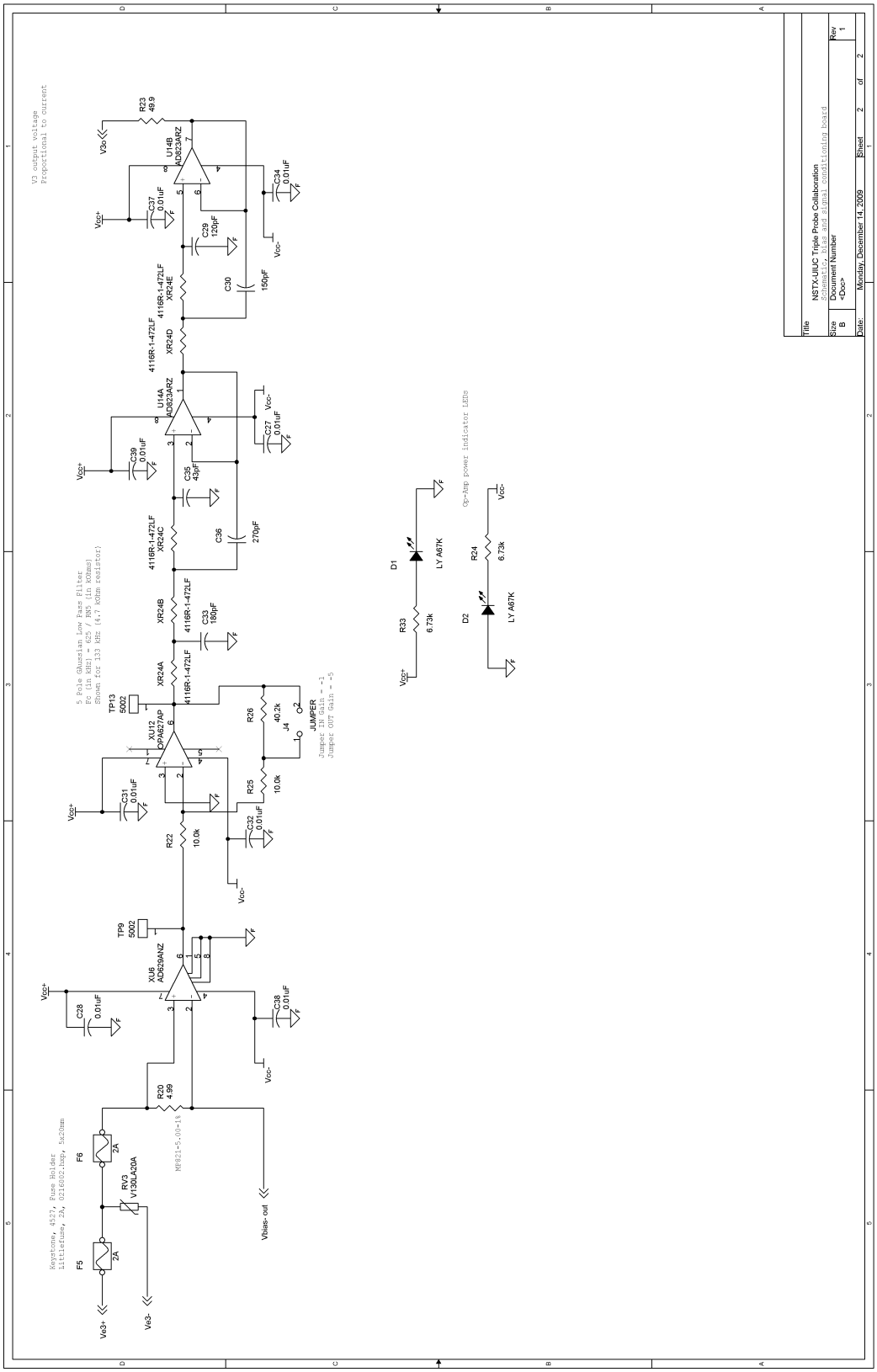

Figure A.4: Triple probe bias/acquisition electronics II

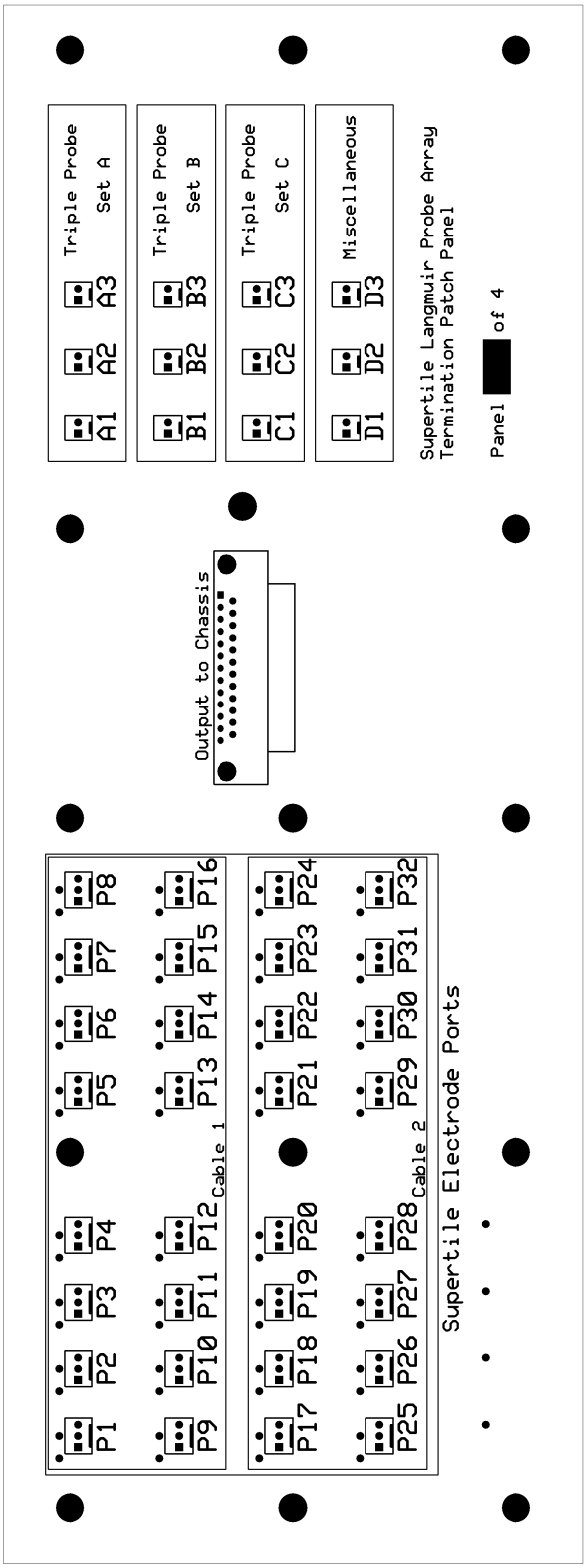

Figure A.5: Patch panel for electrode assignment, showing electrodes on left side (bottom), with probe elements on right (top).

Bibliography

[1] J. P. Freidberg. *Ideal Magnetohydrodynamics*. Springer, 1987.

[2] Peter C Stangeby. *The Plasma Boundary of Magnetic Fusion Devices*. Institute of Physics Publishing, 2000.

[3] R. Chodura. Plasma-wall transition in an oblique magnetic field. *Phys. Fluids*, 25(9), 1982.

[4] D. P. Stotler, R. Maingi, L.E. Zakharov, H.W. Kugel, A.Yu. Pigarov, T.D. Rognlien, and V. A. Soukhanovskii. Simulations of nstx with a liquid lithium divertor module. *Contributions to Plasma Physics*, 50(3-5):368–373, 2010.

[5] H. W. Kugel, M. G. Bell, J.-W. Ahn, J. P. Allain, R. Bell, J. Boedo, C. Bush, D. Gates, T. Gray, S. Kaye, R. Kaita, B. LeBlanc, R. Maingi, R. Majeski, D. Mansfield, J. Menard, D. Mueller, M. Ono, S. Paul, R. Raman, A. L. Roquemore, P. W. Ross, S. Sabbagh, H. Schneider, C. H. Skinner, V. Soukhanovskii, T. Stevenson, J. Timberlake, W. R. Wampler, and L. Zakharov. The effect of lithium surface coatings on plasma performance in the national spherical torus experiment. *Physics of Plasmas*, 15(5):056118, 2008.

[6] H.W. Kugel, M. Bell, L. Berzak, A. Brooks, R. Ellis, S. Gerhardt, H. Harjes, R. Kaita, J. Kallman, R. Maingi, R. Majeski, D. Mansfield, J. Menard, R.E. Nygren, V. Soukhanovskii, D. Stotler, P. Wakeland, and L.E. Zakharov. Physics design

requirements for the national spherical torus experiment liquid lithium divertor. *Fusion Engineering and Design*, 84(7-11):1125 – 1129, 2009. Proceeding of the 25th Symposium on Fusion Technology - (SOFT-25).

[7] J.-W. Ahn, R. Maingi, J.A. Boedo, and V. Soukhanovskii. Dependence of sol widths on plasma current and density in nstx h-mode plasmas. *Journal of Nuclear Materials*, 390-391:421 – 424, 2009. Proceedings of the 18th International Conference on Plasma-Surface Interactions in Controlled Fusion Device, Proceedings of the 18th International Conference on Plasma-Surface Interactions in Controlled Fusion Device.

[8] J-W. Ahn. *Investigations of the Boundary Plasma in the MAST Spherical Tokamak*. PhD thesis, Imperial College of Science,Technology,and Medicine, 2002.

[9] M. A. Jaworski, J. Kallman, R. Kaita, H. Kugel, B. LeBlanc, R. Marsala, and D. N. Ruzic. Biasing, acquisition, and interpretation of a dense langmuir probe array in nstx. *Review of Scientific Instruments*, 81(10):10E130, 2010.

[10] J. Marki, R.A. Pitts, T. Eich, A. Herrmann, J. Horacek, F. Sanchez, and G. Veres. Sheath heat transmission factors on tcv. *Journal of Nuclear Materials*, 363-365:382 – 388, 2007. Plasma-Surface Interactions-17.

[11] D. Buchenauer, J. W. Cuthbertson, J. A. Whaley, J. D. Miller, J. G. Watkins, R. Junge, W. P. West, and D. N. Hill. Sheath physics study using the divertor materials evaluation system (dimes) on diii-d. *Review of Scientific Instruments*, 66(1):827–829, 1995.

[12] R.J. Knize. Plasma particle and energy reflection at a wall with an obliquely incident magnetic field. *Nuclear Fusion*, 25(10):1498, 1985.

[13] BP. Statistical review of world energy, 2009.

[14] IAEA. Nuclear technology review. Technical report, Vienna, 2009.

[15] D. Eckhartt. Nuclear fuels for low-beta fusion reactors: Lithium resources revisited. *Journal of Fusion Energy*, 14(4):329–341, December 1995.

[16] IEA. Energy demand by fuel. `http://www.iea.org/country/graphs/weo_2009/Þg1-1.jpg`, 2009.

[17] IPCC Core Writing Team. Ipcc synthesis report. `http://www.ipcc.ch/publications_and_data/publications_ipcc_fourth_assessment_report_synthesis_report.htm`, 2007.

[18] J.D. Lawson. Some criteria for a power producing thermonuclear reactor. *Proceedings of the Physical Society. Section B*, 70:6–10, 1957.

[19] M. C. Zarnstorff, M. G. Bell, M. Bitter, R. J. Goldston, B. Grek, R. J. Hawryluk, K. Hill, D. Johnson, D. McCune, H. Park, A. Ramsey, G. Taylor, and R. Wieland. Bootstrap current in tftr. *Phys. Rev. Lett.*, 60(13):1306–1309, Mar 1988.

[20] J.P. Allain, D.L. Rokusek, S.S. Harilal, M. Nieto-Perez, C.H. Skinner, H.W. Kugel, B. Heim, R. Kaita, and R. Majeski. Experimental studies of lithium-based surface chemistry for fusion plasma-facing materials applications. *Journal of Nuclear Materials*, 390-391:942 – 946, 2009. Proceedings of the 18th International Conference on Plasma-Surface Interactions in Controlled Fusion Device, Proceedings of the 18th International Conference on Plasma-Surface Interactions in Controlled Fusion Device.

[21] D. Bohm. *The Characteristics of Electrical Discharges in a Magnetic Field*, chapter Minimum ionic kinetic energy for a stable sheath, page 77. McGraw-Hill, 1949.

[22] H Bolt, V Barabash, G Federici, J Linke, A Loarte, J Roth, and K Sato. Plasma facing and high heat flux materials - needs for iter and beyond. *Journal of Nuclear Materials*, 307-311(Part 1):43 – 52, 2002.

[23] H. M. Mott-Smith and Irving Langmuir. The theory of collectors in gaseous discharges. *Phys. Rev.*, 28(4):727–763, Oct 1926.

[24] H.F. Dylla, M. Ulrickson, M.G. Bell, D.K. Owens, D. Buchenauer, R.V. Budny, K.W. Hill, S.J. Kilpatrick, D.M. Manos, P.H. LaMarche, A.T. Ramsey, G.L. Schmidt, and M. Zarnstorff. First-wall conditioning for enhanced confinement discharges and the dt experiments in tftr. *Journal of Nuclear Materials*, 162-164:128 – 137, 1989.

[25] F. Wagner, G. Becker, K. Behringer, D. Campbell, A. Eberhagen, W. Engelhardt, G. Fussmann, O. Gehre, J. Gernhardt, G. v. Gierke, G. Haas, M. Huang, F. Karger, M. Keilhacker, O. Klüber, M. Kornherr, K. Lackner, G. Lisitano, G. G. Lister, H. M. Mayer, D. Meisel, E. R. Müller, H. Murmann, H. Niedermeyer, W. Poschenrieder, H. Rapp, H. Röhr, F. Schneider, G. Siller, E. Speth, A. Stäbler, K. H. Steuer, G. Venus, O. Vollmer, and Z. Yü. Regime of improved confinement and high beta in neutral-beam-heated divertor discharges of the asdex tokamak. *Phys. Rev. Lett.*, 49(19):1408–1412, Nov 1982.

[26] C. E. Bush, M. G. Bell, R. E. Bell, J. Boedo, E. D. Fredrickson, S. M. Kaye, S. Kubota, B. P. LeBlanc, R. Maingi, R. J. Maqueda, S. A. Sabbagh, V. A. Soukhanovskii, D. Stutman, D. W. Swain, J. B. Wilgen, S. J. Zweben, W. M. Davis, D. A. Gates, D. W. Johnson, R. Kaita, H. W. Kugel, K. C. Lee, D. Mastrovito, S. Medley, J. E. Menard, D. Mueller, M. Ono, F. Paoletti, H. Park, S. J. Paul, Y-K. M. Peng, R. Raman, P. G. Roney, A. L. Roquemore, C. H. Skinner, E. J. Synakowski, and G. Taylor NSTX Team. H-mode threshold and dynamics in the national spherical torus experiment. *Physics of Plasmas*, 10(5):1755–1764, 2003.

[27] H R Wilson, S C Cowley, A Kirk, and P B Snyder. Magneto-hydrodynamic stability of the h-mode transport barrier as a model for edge localized modes: an overview. *Plasma Physics and Controlled Fusion*, 48(5A):A71, 2006.

[28] R. Maingi, S.A. Sabbagh, C.E. Bush, E.D. Fredrickson, J.E. Menard, D. Stutman, K. Tritz, M.G. Bell, R.E. Bell, J.A. Boedo, D.A. Gates, D.W. Johnson, R. Kaita, S.M. Kaye, H.W. Kugel, B.P. LeBlanc, D. Mueller, R. Raman, A.L. Roquemore, V.A. Soukhanovskii, and T. Stevenson. Elms and the h-mode pedestal in nstx. *Journal of Nuclear Materials*, 337-339:727 – 731, 2005. PSI-16.

[29] J.-W. Ahn, R. Maingi, D. Mastrovito, and A. L. Roquemore. High speed infrared camera diagnostic for heat flux measurement in nstx. *Review of Scientific Instruments*, 81(2):023501, 2010.

[30] V.A. Soukhanovskii, R.E. Bell, C. Bush, R. Kaita, H.W. Kugel, B.P. LeBlanc, R. Maingi, R. Raman, and A.L. Roquemore. On the secular density rises in nbi-heated h-mode plasmas in nstx. *Journal of Nuclear Materials*, 390-391:516 – 519, 2009. Proceedings of the 18th International Conference on Plasma-Surface Interactions in Controlled Fusion Device, Proceedings of the 18th International Conference on Plasma-Surface Interactions in Controlled Fusion Device.

[31] J.E. Menard, M.G. Bell, R.E. Bell, S. Bernabei, J. Bialek, T. Biewer, W. Blanchard, J. Boedo, C.E. Bush, M.D. Carter, W. Choe, N.A. Crocker, D.S. Darrow, W. Davis, L. Delgado-Aparicio, S. Diem, C.W. Domier, D.A. D'Ippolito, J. Ferron, A. Field, J. Foley, E.D. Fredrickson, D.A. Gates, T. Gibney, R. Harvey, R.E. Hatcher, W. Heidbrink, K.W. Hill, J.C. Hosea, T.R. Jarboe, D.W. Johnson, R. Kaita, S.M. Kaye, C.E. Kessel, S. Kubota, H.W. Kugel, J. Lawson, B.P. LeBlanc, K.C. Lee, F.M. Levinton, N.C. Luhmann Jr., R. Maingi, R.P. Majeski, J. Manickam, D.K. Mansfield, R. Maqueda, R. Marsala, D. Mastrovito, T.K. Mau, E. Mazzucato, S.S. Medley, H. Meyer, D.R. Mikkelsen, D. Mueller, T. Munsat, J.R. Myra, B.A. Nelson, C. Neumeyer, N. Nishino, M. Ono, H.K. Park, W. Park, S.F. Paul, T. Peebles, M. Peng, C. Phillips, A. Pigarov, R. Pinsker, A. Ram, S. Ramakrishnan, R. Raman, D. Rasmussen, M. Redi, M. Rensink, G. Rewoldt, J. Robinson, P. Roney, A.L. Roquemore,

E. Ruskov, P. Ryan, S.A. Sabbagh, H. Schneider, C.H. Skinner, D.R. Smith, A. Sontag, V. Soukhanovskii, T. Stevenson, D. Stotler, B.C. Stratton, D. Stutman, D. Swain, E. Synakowski, Y. Takase, G. Taylor, K. Tritz, A. von Halle, M. Wade, R. White, J. Wilgen, M. Williams, J.R. Wilson, H. Yuh, L.E. Zakharov, W. Zhu, S.J. Zweben, R. Akers, P. Beiersdorfer, R. Betti, T. Bigelow, M. Bitter, P. Bonoli, C. Bourdelle, C.S. Chang, J. Chrzanowski, L. Dudek, P.C. Efthimion, M. Finkenthal, E. Fredd, G.Y. Fu, A. Glasser, R.J. Goldston, N.L. Greenough, L.R. Grisham, N. Gorelenkov, L. Guazzotto, R.J. Hawryluk, J. Hogan, W. Houlberg, D. Humphreys, F. Jaeger, M. Kalish, S. Krasheninnikov, L.L. Lao, J. Lawrence, J. Leuer, D. Liu, G. Oliaro, D. Pacella, R. Parsells, M. Schaffer, I. Semenov, K.C. Shaing, M.A. Shapiro, K. Shinohara, P. Sichta, X. Tang, R. Vero, M. Walker, and W. Wampler. Overview of recent physics results from the national spherical torus experiment (nstx). *Nuclear Fusion*, 47(10):S645, 2007.

[32] D. K. Mansfield, K. W. Hill, J. D. Strachan, M. G. Bell, S. D. Scott, R. Budny, E. S. Marmar, J. A. Snipes, J. L. Terry, S. Batha, R. E. Bell, M. Bitter, C. E. Bush, Z. Chang, D. S. Darrow, D. Ernst, E. Fredrickson, B. Grek, H. W. Herrmann, A. Janos, D. L. Jassby, F. C. Jobes, D. W. Johnson, L. C. Johnson, F. M. Levinton, D. R. Mikkelsen, D. Mueller, D. K. Owens, H. Park, A. T. Ramsey, A. L. Roquemore, C. H. Skinner, T. Stevenson, B. C. Stratton, E. Synakowski, G. Taylor, A. von Halle, S. von Goeler, K. L. Wong, and S. J. Zweben TFTR Group. Enhancement of tokamak fusion test reactor performance by lithium conditioning. *Physics of Plasmas*, 3(5):1892–1897, 1996.

[33] R. Kaita, R. Majeski, R. Doerner, T. Gray, H. Kugel, T. Lynch, R. Maingi, D. Mansfield, V. Soukhanovskii, J. Spaleta, J. Timberlake, and L. Zakharov. Extremely low recycling and high power density handling in cdx-u lithium experiments. *Journal of Nuclear Materials*, 363-365:1231 – 1235, 2007. Plasma-Surface Interactions-17.

[34] H.W. Kugel, M.G. Bell, R. Bell, C. Bush, D. Gates, T. Gray, R. Kaita, B. Leblanc, R. Maingi, R. Majeski, D. Mansfield, D. Mueller, S. Paul, R. Raman, A.L. Roquemore, S. Sabbagh, C.H. Skinner, V. Soukhanovskii, T. Stevenson, and L. Zakharov. Effect of lithium pfc coatings on nstx density control. *Journal of Nuclear Materials*, 363-365:791 – 796, 2007. Plasma-Surface Interactions-17.

[35] D.K. Mansfield, H.W. Kugel, R. Maingi, M.G. Bell, R. Bell, R. Kaita, J. Kallman, S. Kaye, B. LeBlanc, D. Mueller, S. Paul, R. Raman, L. Roquemore, S. Sabbagh, H. Schneider, C.H. Skinner, V. Soukhanovskii, J. Timberlake, J. Wilgen, and L. Zakharov. Transition to elm-free improved h-mode by lithium deposition on nstx graphite divertor surfaces. *Journal of Nuclear Materials*, 390-391:764 – 767, 2009. Proceedings of the 18th International Conference on Plasma-Surface Interactions in Controlled Fusion Device, Proceedings of the 18th International Conference on Plasma-Surface Interactions in Controlled Fusion Device.

[36] B. P. LeBlanc, R. E. Bell, D. W. Johnson, D. E. Hoffman, D. C. Long, and R. W. Palladino. Operation of the nstx thomson scattering system. *Review of Scientific Instruments*, 74(3):1659–1662, 2003.

[37] R. Maingi, T. H. Osborne, B. P. LeBlanc, R. E. Bell, J. Manickam, P. B. Snyder, J. E. Menard, D. K. Mansfield, H. W. Kugel, R. Kaita, S. P. Gerhardt, S. A. Sabbagh, and F. A. Kelly. Edge-localized-mode suppression through density-profile modification with lithium-wall coatings in the national spherical torus experiment. *Phys. Rev. Lett.*, 103(7):075001, Aug 2009.

[38] T.K. Gray, R. Maingi, A. G. McLean, V. A. Soukhanovskii, and J-W. Ahn. Dependencies of the divertor and midplane heat flux widths in nstx. In *23rd IAEA Fusion Energy Conference*. IAEA, 2010.

[39] D.K. Mansfield, A.L. Roquemore, H. Schneider, J. Timberlake, H. Kugel, and M.G.

Bell. A simple apparatus for the injection of lithium aerosol into the scrape-off layer of fusion research devices. *Fusion Engineering and Design*, 85(6):890 – 895, 2010. Proceedings of the 1st International Workshop on Lithium Applications for the Boundary Control in Fusion Devices.

[40] K H Burrell, M E Austin, D P Brennan, J C DeBoo, E J Doyle, P Gohil, C M Greenfield, R J Groebner, L L Lao, T C Luce, M A Makowski, G R McKee, R A Moyer, T H Osborne, M Porkolab, T L Rhodes, J C Rost, M J Schaffer, B W Stallard, E J Strait, M R Wade, G Wang, J G Watkins, W P West, and L Zeng. Quiescent h-mode plasmas in the diii-d tokamak. *Plasma Physics and Controlled Fusion*, 44(5A):A253, 2002.

[41] R. Kaita, D. Johnson, H. Kugel, McCormack, A. L. Roquemore, and the NSTX team. Initial diagnostics for the national spherical torus experiment. In *26th EPS Conf. on Contr. Fusion and Plasma Physics*, 1999.

[42] D Johnson and NSTX Team. Diagnostic development for st plasmas on nstx. *Plasma Physics and Controlled Fusion*, 45(11):1975, 2003.

[43] B. C. Stratton, R. J. Fonck, K. Ida, K. P. Jaehnig, and A. T. Ramsey. Spred spectrograph upgrade: High-resolution grating and improved absolute calibrations. *Review of Scientific Instruments*, 57(8):2043–2045, 1986.

[44] P. Beiersdorfer, J. K. Lepson, M. Bitter, K. W. Hill, and L. Roquemore. Time-resolved x-ray and extreme ultraviolate spectrometer for use on the national spherical torus experiment. *Review of Scientific Instruments*, 79(10):10E318, 2008.

[45] J K Lepson, P Beiersdorfer, J Clementson, M F Gu, M Bitter, L Roquemore, R Kaita, P G Cox, and A S Safronova. Euv spectroscopy on nstx. *Journal of Physics B: Atomic, Molecular and Optical Physics*, 43(14):144018, 2010.

[46] S. F. Paul, R. J. Fonck, and A. K. MacAulay. Using a free-standing thermistor array to measure vuv emission from a tokamak plasma. *Review of Scientific Instruments*, 64(9):2423–2427, 1993.

[47] T.E. Evans, M.E. Fenstermacher, R.A. Moyer, T.H. Osborne, J.G. Watkins, P. Gohil, I. Joseph, M.J. Schaffer, L.R. Baylor, M. BÃ©coulet, J.A. Boedo, K.H. Burrell, J.S. deGrassie, K.H. Finken, T. Jernigan, M.W. Jakubowski, C.J. Lasnier, M. Lehnen, A.W. Leonard, J. Lonnroth, E. Nardon, V. Parail, O. Schmitz, B. Unterberg, and W.P. West. Rmp elm suppression in diii-d plasmas with iter similar shapes and collisionalities. *Nuclear Fusion*, 48(2):024002, 2008.

[48] S.A. Sabbagh, J.M. Bialek, R.E. Bell, A.H. Glasser, B.P. LeBlanc, J.E. Menard, F. Paoletti, M.G. Bell, R. Fitzpatrick, E.D. Fredrickson, A.M. Garofalo, D.A. Gates, S.M. Kaye, L.L. Lao, R. Maingi, D. Mueller, G.A. Navratil, D. Stutman, W. Zhu, and the NSTX Research Team. The resistive wall mode and feedback control physics design in nstx. *Nuclear Fusion*, 44(4):560, 2004.

[49] S. A. Sabbagh, R. E. Bell, J. E. Menard, D. A. Gates, A. C. Sontag, J. M. Bialek, B. P. LeBlanc, F. M. Levinton, K. Tritz, and H. Yuh. Active stabilization of the resistive-wall mode in high-beta, low-rotation plasmas. *Phys. Rev. Lett.*, 97(4):045004, Jul 2006.

[50] J.M. Canik, R. Maingi, T.E. Evans, R.E. Bell, S.P. Gerhardt, H.W. Kugel, B.P. LeBlanc, J. Manickam, J.E. Menard, T.H. Osborne, J.-K. Park, S. Paul, P.B. Snyder, S.A. Sabbagh, E.A. Unterberg, and the NSTX team. Elm destabilization by externally applied non-axisymmetric magnetic perturbations in nstx. *Nuclear Fusion*, 50(3):034012, 2010.

[51] S K Erents, G M McCracken, and P Goldsmith. Trapping of kev deuterons in lithium. *Journal of Physics D: Applied Physics*, 4(5):672, 1971.

[52] V. A. Evtikhin, I. E. Lyublinski, A. V. Vertkov, V. G. Belan, I. K. Konkashbaev, and L. B. Nikandrov. Calculation and experimental investigation of fusion reactor divertor plate and first wall protection by capillary-pore systems with lithium. *Journal of Nuclear Materials*, 271-272:396 – 400, 1999.

[53] V A Evtikhin, I E Lyublinski, A V Vertkov, S V Mirnov, V B Lazarev, N P Petrova, S M Sotnikov, A P Chernobai, B I Khripunov, V B Petrov, D Yu Prokhorov, and V M Korzhavin. Lithium divertor concept and results of supporting experiments. *Plasma Physics and Controlled Fusion*, 44(6):955, 2002.

[54] M.L. Apicella, G. Mazzitelli, V. Pericoli Ridolfini, V. Lazarev, A. Alekseyev, A. Vertkov, and R. Zagórski. First experiments with lithium limiter on ftu. *Journal of Nuclear Materials*, 363-365:1346 – 1351, 2007. Plasma-Surface Interactions-17.

[55] M.J. Baldwin, R.P. Doerner, S.C. Luckhardt, and R.W. Conn. Deuterium retention in liquid lithium. *Nuclear Fusion*, 42(11):1318, 2002.

[56] S. I. Krasheninnikov, L. E. Zakharov, and G. V. Pereverzev. On lithium walls and the performance of magnetic fusion devices. *Physics of Plasmas*, 10(5):1678–1682, 2003.

[57] R. Majeski, R. Doerner, T. Gray, R. Kaita, R. Maingi, D. Mansfield, J. Spaleta, V. Soukhanovskii, J. Timberlake, and L. Zakharov. Enhanced energy confinement and performance in a low-recycling tokamak. *Phys. Rev. Lett.*, 97(7):075002, Aug 2006.

[58] R. Maingi. Private communcation.

[59] V. A. Soukhanovskii, A. L. Roquemore, C. H. Skinner, J. Menard, H. W. Kugel, D. Johnson, R. Maingi, S. Sabbagh, and F. Paoletti. High-resolution spectroscopic diagnostic for divertor and scrape-off layer neutral and impurity emission measure-

ments in the national spherical torus experiment. *Review of Scientific Instruments*, 74(3):2094–2097, 2003.

[60] R. Majeski, S. Jardin, R. Kaita, T. Gray, P. Marfuta, J. Spaleta, J. Timberlake, L. Zakharov, G. Antar, R. Doerner, S. Luckhardt, R. Seraydarian, V. Soukhanovskii, R. Maingi, M. Finkenthal, D. Stutman, D. Rodgers, and S. Angelini. Recent liquid lithium limiter experiments in cdx-u. *Nuclear Fusion*, 45(6):519, 2005.

[61] C. Taylor S. Ortoleva M. Gonzalez J.P. Allain H. Kugel R. Kaita C. Skinner L. Roquemore B, Heim. The material analysis particle probe (mapp) as an in-situ plasma-material interaction diagnostic in nstx. In *52nd Annaual Meeting of the APS Division of Plasma Physics*, 2010.

[62] D.G. Whyte, T.E. Evans, C.P.C. Wong, W.P. West, R. Bastasz, J.P. Allain, and J.N. Brooks. Experimental observations of lithium as a plasma-facing surface in the diii-d tokamak divertor. *Fusion Engineering and Design*, 72(1-3):133 – 147, 2004. Special Issue on Innovative High-Power Density Concepts for Fusion Plasma Chambers.

[63] R. Ellis et al. In *23rd IEEE/NPSS Symposium on Fusion Engineering, 2009*, pages 1 –4, 2009.

[64] J.N. Brooks, T.D. Rognlien, D.N. Ruzic, and J.P. Allain. Erosion/redeposition analysis of lithium-based liquid surface divertors. *Journal of Nuclear Materials*, 290-293:185 – 190, 2001. 14th Int. Conf. on Plasma-Surface Interactions in Controlled Fusion D evices.

[65] R. Bell. Private communication.

[66] J. A. Boedo, N. Crocker, L. Chousal, R. Hernandez, J. Chalfant, H. Kugel, P. Roney, J. Wertenbaker, and NSTX Team. Fast scanning probe for the nstx spherical tokamak. *Review of Scientific Instruments*, 80(12):123506 –123506–10, December 2009.

[67] J. B. Wilgen, G. R. Hanson, T. S. Bigelow, D. W. Swain, P. M. Ryan, M. D. Carter, and J. R. Wilson. Reflectometer Measurements of Edge Density Profile for ICRF Coupling Studies on NSTX. *APS Meeting Abstracts*, pages 1012P–+, October 2001.

[68] R. Kaita, H. Kugel, J. Kallman, B. Leblanc, S. Paul, A. L. Roquemore, C. Skinner, V. Soukhanovskii, R. Maingi, J.-W. Ahn, J. Wilgen, J.-P. Allain, and C. Taylor. Diagnostics for Evaluating Performance of NSTX Liquid Lihium Divertor. pages 8046P–+, November 2009.

[69] D. Mastrovito, R. Maingi, H. W. Kugel, and A. L. Roquemore. Infrared camera diagnostic for heat flux measurements on the national spherical torus experiment. *Review of Scientific Instruments*, 74(12):5090–5092, 2003.

[70] S J Zweben, R J Maqueda, A L Roquemore, C E Bush, R Kaita, R J Marsala, Y Raitses, R H Cohen, and D D Ryutov. Local scrape-off layer control using biased electrodes in nstx. *Plasma Physics and Controlled Fusion*, 51(10):105012, 2009.

[71] H.W. Kugel, B. McCormack, R. Kaita, P. Goranson, L. Gutttadora, R. Hatcher, T. Holoman, D. Johnson, B. Nelson, C. Neumeyer, and A.L. Roquemore. Nstx high temperature sensor systems. pages 300 –305, 1999.

[72] J.P. Gunn, C. Boucher, B.L. Stansfield, and S. Savoie. *Review of Scientific Instruments*, 66(1):154–159, 1995.

[73] J. Kallman, M. A. Jaworski, R. Kaita, H. Kugel, and T. K. Gray. High density langmuir probe array for nstx scrape-off layer measurements under lithiated divertor conditions. *Review of Scientific Instruments*, 81(10):10E117, 2010.

[74] R. Maingi and the NSTX Research Team. *Nuclear Fusion*, 43(9):969, 2003.

[75] S.J. Zweben et al. *Plasma Physics and Controlled Fusion*, 49(7):S1, 2007.

[76] D.W. Jeppson, J.L Ballif, W.W. Yuan, and B.E. Chou. Lithium literature review: Lithium's properties and interactions. Technical report, Hanford Engineering Development Laboratory, 1978.

[77] Mdsplus home page. `http://www.mdsplus.org`.

[78] G F Matthews. Tokamak plasma diagnosis by electrical probes. *Plasma Physics and Controlled Fusion*, 36(10):1595, 1994.

[79] L.L. Lao, H. St. John, R.D. Stambaugh, A.G. Kellman, and W. Pfeiffer. Reconstruction of current profile parameters and plasma shapes in tokamaks. *Nuclear Fusion*, 25(11):1611, 1985.

[80] A. McLean, J.-W. Ahn, T.K. Gray, R. Maingi, M. Bell, R. Bell, M.A. Jaworski, H. Kugel, B.C. Lyons, R.E. Nygren, L. Roquemore, F. Scotti, and C.H. Skinner. Liquid lithium divertor surface temperature dynamics and edge plasma modification under plasma-induced heating and lithium pre-heating. In *2nd International Symposium on Lithium Applications in Fusion Devices*, 2011.

[81] Santa Barbara Focal Plane. `http://www.sbfp.com/imagir_camera.html`.

[82] J.C. Jaeger H.S. Carlsaw. *Conduction of Heat in Solids*. Oxford Science Publications, 1986.

[83] A Herrmann, W Junker, K Gunther, S Bosch, M Kaufmann, J Neuhauser, G Pautasso, Th Richter, and R Schneider. Energy flux to the asdex-upgrade diverter plates determined by thermography and calorimetry. *Plasma Physics and Controlled Fusion*, 37(1):17, 1995.

[84] A. McLean. Private communcation.

[85] Bear Kleiner John Chambers, William Cleveland and Paul Tukey. *Graphical Methods for Data Analysis*. Wadsworth, 1983.

[86] Hua-Tan Qiu and D.N. Ruzic. Molecular dynamics modeling of deuterium in liquid lithium surfaces. *Journal of Nuclear Materials*, 337-339:1029 – 1032, 2005. PSI-16.

[87] R. Chodura. Kinetic effects in the scrape off layer. *Contributions to Plasma Physics*, 32(3-4):219–230, 1992.

[88] M.A. Jaworski et al. ModiÞcation of the electron energy distribution function during lithium experiments on the national spherical torus experiment. *Fusion Engineering and Design*, In Press.